

AMANDEEP SINGH

Nanoparticle Synthesis by Pulsed Laser Ablation: From H₂O to pressurized CO₂

Possibilities for supercritical fluid
as reactive environment

AMANDEEP SINGH

Nanoparticle Synthesis by Pulsed Laser Ablation:
From H₂O to pressurized CO₂
Possibilities for supercritical fluid as reactive environment

ACADEMIC DISSERTATION

To be presented, with the permission of
the Faculty of Engineering and Natural Sciences
of Tampere University,
for public discussion in K1705 Auditorium
of the Konetalo Building, Kokeakoulunkatu 6, Tampere,
on the 11th of September 2020, at 1 pm.

ACADEMIC DISSERTATION

Tampere University, Faculty of Engineering and Natural Sciences
Finland

<i>Responsible supervisor and Custos</i>	Professor Erkki Levänen Tampere University Finland	
<i>Supervisor</i>	Dr. Erkki Frankberg Tampere University Finland	
<i>Pre-examiners</i>	Professor Simo-Pekka Hannula Aalto University Finland	Associate Professor David Amans Université Claude Bernard Lyon 1 France
<i>Opponents</i>	Associate Professor David Amans Université Claude Bernard Lyon 1 France	Professor Jouko Peltonen Åbo Akademi University Finland

The originality of this thesis has been checked using the Turnitin OriginalityCheck service.

Copyright ©2020 author

Cover design: Roihu Inc.

ISBN 978-952-03-1668-6 (print)

ISBN 978-952-03-1669-3 (pdf)

ISSN 2489-9860 (print)

ISSN 2490-0028 (pdf)

<http://urn.fi/URN:ISBN:978-952-03-1669-3>

PunaMusta Oy – Yliopistopaino
Vantaa 2020

Dedication

I would like to dedicate this book to all the kids in my homeland undivided-Panjab, especially from my ancestral village 'Bella'. I hope this book and my life encourages you to pursue an academic career and know that sky is not the limit. Be curious, be kind, help others, and be brave. Stay in Chardi kala - soaring spirits. Learn both 'Panjabi' and 'English'. The future is in your hands. Pick up the pen and start writing!

ACKNOWLEDGEMENTS

This doctoral dissertation was started in 2015 to effectively combine two different technologies involving pulsed lasers and supercritical CO₂ utilization, with reactive metal to produce different metal oxide nanomaterials and carbon nanostructures. The dissertation consists of the key studies I did between 2015 and 2019. Being a pioneer work meant lots of challenges and design improvements over the years, which at the same time was enthralling for me. For making this doctoral dissertation possible and a fruitful learning experience, I would like to thank the following:

Thanks to funding agencies for scholarships, grants, and research projects:

For research funding, I would like to acknowledge Tampere University Foundation (formerly TTY Säätiö) for granting me a four-year scholarship 2015-18 for doctoral studies. I would also like to acknowledge European Commission's Horizon 2020 project 'NanoStencil'—Proposal number 767285 for funding this research 2018-20. Special thanks to Tekniikan Edistämissäätiö (TES) for awarding me with the encouragement grant for the year 2018 based on my research achievements, to encourage me to do better.

Thanks to the Academic partners

I am thankful to Dr. Hua Jiang at the Nanomicroscopy Center (Aalto-NMC) at Aalto University, and Dr. Mari Honkanen at Tampere Microscopy Center in Tampere University for TEM, HR-TEM, and STEM imaging. I am grateful to Jere Manni at Top Analytica for XPS analysis, and to Tommi Vuorinen at VTT for bandgap measurement of nanoparticles.

Thanks to supervisor and co-authors

I would like to thank all my colleagues at the Materials Science laboratory. I would like to especially thank my supervisor Professor Erkki Levänen (Head of advanced ceramic materials group, former Head of Materials Science Department) for proposing and supervising this topic, for believing in me, and for giving me freedom

to plan and conduct research. I am thankful to Jorma Vihinen for being always ready to provide laser and its training for our exciting ablation experiments. I thank my former supervisor Dr. Matti Järveläinen for his help and supervision ever since I started working with the advanced ceramic materials group at Tampere University. I am thankful to Dr. Erkkä Frankberg, who shared the same enthusiasm about synthesizing nanomaterials with pulsed laser ablation as I have, and for the good supervision early on. I thank all my co-authors for their contributions to our manuscripts. I wish to specially thank Mari Honkanen, and Turkka Salminen, for their thorough and timely participation and collaboration for our manuscripts.

Thanks to colleagues, family and other near and dear ones

I am thankful to my colleagues who are also my friends and have always helped me over the years – Matti Järveläinen, Aaretti Kaleva, Saara Söyrinki, and Setareh Zakeri. I thank all colleagues at the faculty of engineering and natural sciences for their contribution in creating a good working environment. I thank my brother Gagandeep Singh for stimulating my passion for science and engineering at an early age. I am grateful to my parents – Sirdar Ranbir Singh and Sirdarni Narinder Kaur, for an amazing upbringing and providing me with the environment to study well, especially my mom for consistently motivating me to achieve higher academically, for her struggle in life to make ends meet to see her children progress in life, and for supporting me throughout the years with prayers and more. I understand the hardships and injustices they went through as a minority community in India, and their belief in good education to elevate us out of the predicament. Thanks to my beloved Eveliina for believing in me, supporting me through difficult times, and encouraging me to excel. I have no perfect words to express my gratitude to my family.

I wish to thank Tampere University's powerlifting-weightlifting club 'Herwannan Hauiskääntö', photography club 'TT-Kamerat', and their members for such an amazing time and unforgettable memories to cherish.

I am grateful to this beautiful country – Finland, for giving me the opportunity and infrastructure to carry out state-of-the-art research work and for bringing many friends in my life who are like family. Kiitos ystäville, jotka auttoivat minua oppimaan ja puhumaan suomea: kiitos Matti, Tytti, Aaretti, Natalia, Minna, ja Eve. I thank my friends for making me feel that I belong here. To be honest, I felt for the first time as an equal in the society after coming to Finland, where the nation state is not controlling me. There is a feeling of freedom here.

In the end, I thank the 1-force, 1-ness (or however you choose to call) for everything and pray for good health of all during the current corona virus Covid-19 pandemic.

Further, I add acknowledgments in my mother-language Punjabi:

ਸਬਦੁ ਗੁਰੂ ਸੁਰਤਿ ਧੁਨਿ ਚੇਲਾ ॥

ਗੁਰੂ ਦਾ ਕੇਟਾਂ ਕੇਟ ਸੁਕਰਾਨਾ ॥ੳੳ ਵਾਹਿਗੁਰੂ ਨਾਲ ਜੋੜਨ ਲਈ । ਅੱਗੋਂ ਵਾਸਤੇ ਵੀ ਹੁਕਮ ਵਿੱਚ ਰਹਿਣ ਦਾ ਬਲ ਬਖਸ਼ਣਾ । ਭੁੱਲਾਂ ਚੁੱਕਾਂ ਮੁਆਫ ਕਰਨੀਆਂ । ਸੁਮੱਤ ਦਾ ਦਾਨ ਬਖਸ਼ਣਾ ਜੀ । ਸਿੱਖ ਪੜ੍ਹਦੇ ਸੁਣਦੇ ਸਰਬੱਤ ਲਾਹੇਵੰਦ ਹੋਣ । ਨਾਨਕ ਨਾਮ ਚੜ੍ਹਦੀ ਕਲਾ ਤੇਰੇ ਭਾਣੇ ਸਰਬੱਤ ਦਾ ਭਲਾ ।

ਮੈਂ ਪੰਜਾਬੀ ਭਾਸ਼ਾ ਅਤੇ ਉਸ ਵਿੱਚ ਕਵਿਤਾ ਭਾਵੇਂ ਕਿ ਭਾਈ ਵੀਰ ਸਿੰਘ ਜੀ, ਪ੍ਰੋ ਪੂਰਨ ਸਿੰਘ ਜੀ, ਸਿਰਦਾਰ ਕਪੂਰ ਸਿੰਘ ਜੀ ਅਤੇ ਪ੍ਰੋ ਹਰਿੰਦਰ ਸਿੰਘ ਮਹਿਬੂਬ ਜੀ ਵਾਂਗ ਨਹੀਂ ਲਿਖ ਸਕਦਾ, ਪਰ ਇਹ ਰੇਠ ਲਿਖੀਆਂ ਸਤਰਾਂ ਮੇਰਾ ਇਸ ਦਿਸ਼ਾ ਵੱਲ ਇੱਕ ਨਿਮਾਣਾ ਜਿਹਾ ਉਪਰਾਲਾ ਹੈ।

“ਪੰਜਾਬੀ ਪੰਜਾਬੀ-ਬੋਲੀ ਬੋਲਣ ਤੋਂ ਅੱਜ ਸੰਗਦੇ,
ਰਹਿੰਦੀ ਨਾ ਇਹ ਬੋਲੀ ਨਾ ਪੰਜਾਬੀ ਸੂਬਾ ਜੇ ਖਾਲਸਾ ਜੀ ਸਰਕਾਰ ਮੂਹਰੇ ਨਾ ਖੜਦੇ ।
ਘਰੇ ਬੋਲਣੀ ਮਾਂ ਬੋਲੀ ਪੰਜਾਬੀ ਪਰ ਘਰੋਂ ਬਾਹਰ ਵਿਸਾਰਣੀ,
ਕਦੇ ਕਹਿਣਾ 'ਨਹੂੰ ਮਾਸ' ਦਾ ਰਿਸ਼ਤਾ ਤੇ ਕਦੇ ਮਾਂ ਹੀ ਬਦਲ ਕੇ ਹਿੰਦੀ ਬਣਾ ਲੈਣੀ ।
ਜਦੋਂ ਵੈਰੀ ਆਇਆ ਚੜ੍ਹ ਕੇ ਤੇ ਪੁਛਿਆ ਕੀ ਹੈ ਤੁਹਾਡੀ ਮਾਂ ਬੋਲੀ ?,
ਗੱਦਾਰੀ ਉਨ੍ਹਾਂ ਪੰਜਾਬੀਆਂ ਦੀ ਜਿਨ੍ਹਾਂ ਸਖੀ ਮਾਂ ਛਡ ਕੇ ਲਿਖਾਇਆ 'ਹਿੰਦੀ' ਹੈ ਹਮਾਰੀ ਮਾਂ ਬੋਲੀ ।
ਵੈਰੀ ਫਿਰ ਕੁਟਾਪਾ ਚਾੜ੍ਹਿਆ ਪੰਜਾਬ ਦਾ ਅਤੇ ਕੀਤੇ ਇਸਦੇ ਟੋਟੇ ਟੋਟੇ,
ਲੰਗੜੇ ਲੂਲੇ ਪੰਜਾਬ ਦਾ ਫਿਰ ਲੁਟਿਆ ਵੈਰੀ ਨੇ ਪਾਣੀ ਜੀਉ ।
ਗੁਰੂ ਸਾਹਿਬ ਆਖਿਆ 'ਪਾਣੀ ਪਿਤਾ ਮਾਤਾ ਧਰਤਿ',
ਮਾਂਪੇ ਲੁੱਟ ਲਏ ਪੰਜਾਬ ਦੇ, ਹੁਣ ਕਰੇ ਕੀ ਯਤੀਮ ਜੀਉ ।
ਸਿਰ ਸੁੱਟ ਕੇ ਮਨ ਹਾਰ ਕੇ ਨਾ ਬੈਠੇ ਮੇਰੇ ਮੀਤ ਜੀਉ,
ਸਿਰ ਜੋੜੋ ਅਤੇ ਕਰੋ ਯਾਦ ਕਿੱਦਾਂ ਦਿਸਦੀ ਸੀ ਸਰਾਭੇ ਨੂੰ ਚਮਕੇਰ ਅਤੇ ਸਰਹਿੰਦ ਚਮਕਦੀ ਮਿਸਾਲ ਜੀਉ ।
ਚੁਰਾਸੀ ਦੇ ਘੱਲੂਘਾਰੇ ਦਾ ਜਖਮ ਦਿਸਦਾ ਗੁਰਭਗਤ ਸਿੰਘ ਨੂੰ ਸੂਰਜ ਜੀਉ,
ਲਓ ਰੋਸ਼ਨੀ ਇਸ ਤੋਂ, ਵਿਚਾਰੋ ਬਾਣੀ ਅਤੇ ਕਰੋ ਤਿੱਖਾ ਬਿਬੇਕ ਜੀਉ ।”

It was an honour to start my D.Sc. studies in the same year to which the United Nations declared as “2015 – The Year of the Light”.

Tampere, August 2020

Amandeep Singh

ABSTRACT

The demand of nanoparticles has been increasing tremendously. However, the traditional methods of synthesis are mostly based on wet-chemical synthesis, that generally need chemical precursors that may not be environment friendly. Due to this, new greener techniques need to be designed and tested. PLAL technique has been demonstrated as a promising method that can be used to synthesize nanoparticles from almost the entire periodic table and requires much cheaper precursors than chemical synthesis techniques. The nanoparticles produced can have clean ligand-free surfaces, due to which they are ready for functionalization and act as better catalysts.

In this work, a single step method, PLA in H_2O and supercritical CO_2 , was used to produce TiO_2 nanoparticles and TiO_2 -carbon core-shell nanoparticles, by utilizing CO_2 in the process. Pressurized CO_2 , in the form of gaseous, liquid, and supercritical CO_2 was demonstrated as a promising solvent for producing well-dispersed agglomerate free nanoparticles and core-shell nanoparticles using PLA technique. With the proposed techniques, it is possible to produce stable rutile- TiO_2 as nanoparticle suspension by PLA in H_2O , while PLA in $scCO_2$ can be used to produce well dispersed non-agglomerate anatase- TiO_2 nanoparticles directly as a dry nanoparticle powder. Further, core-shell nanoparticles of anatase- TiO_2 as core and carbon as shell can be prepared by PLA in pressurized CO_2 and their size can be controlled by simply controlling the CO_2 pressure and temperature.

TABLE OF CONTENTS

Acknowledgements.....	v
Abstract.....	ix
Table of contents	xi
Abbreviations and symbols.....	xiii
List of original publications.....	xv
Author's contribution.....	xvi
1 Introduction.....	19
1.1 Aim of the work.....	20
1.2 Structure of the thesis	21
1.3 Scientific contribution of thesis	22
1.4 Research questions	23
2 Background of nanomaterials synthesis by pulsed laser ablation	24
2.1 TiO ₂ nanomaterials	24
2.2 Pulsed laser ablation (PLA)	27
2.3 PLA in liquids (PLAL).....	28
2.3.1 PLAL and nanoparticle formation.....	28
2.3.2 Types of nanoparticles by PLAL.....	30
2.4 Effects of PLAL process parameters	32
2.4.1 Effects of laser parameters	32
2.4.2 Material type.....	35
2.4.3 Effect of ablation medium on laser beam during PLAL	36
2.5 Shock wave emission and cavitation bubble phenomenon	37
2.6 Supercritical carbon dioxide (scCO ₂).....	38
2.6.1 Properties of CO ₂	38
2.6.2 Processing with scCO ₂	39
2.7 PLA in scCO ₂	39
2.7.1 Generality on bubble dynamics	39
2.7.2 PLA of low reactivity metals in pressurized CO ₂	44

3	Nanoparticle synthesis and characterization methods.....	46
3.1	Precursors	47
3.2	Preparing nanoparticles by PLA in H ₂ O and pressurized CO ₂	47
3.3	Analytical techniques	51
4	PLA in H ₂ O - (<i>Synthesis of stable phase rutile-TiO₂ nanoparticles and their size reduction and narrowing of size distribution measurement</i>).....	54
4.1	TEM analysis of nanoparticles	54
4.2	Phase analysis of nanoparticles by XRD, WAXS and Raman spectroscopy	56
4.3	Particle size and size distribution measurements (TEM and SAXS)	58
4.4	Comparison of nanoparticle morphology and phase synthesized with different laser parameters	61
5	PLA in pressurized CO ₂ - (<i>Synthesis of Stable, Meta-Stable Anatase-TiO₂, Ti_xO_y Nanoparticles With Or Without Carbon Shell/Layer</i>).....	65
5.1	Synthesis of nanoparticles by PLA in scCO ₂ vs H ₂ O – A Comparative analysis.....	65
5.1.1	TEM analysis of nanoparticles	66
5.1.2	Phase analysis – Raman and XRD.....	68
5.1.3	Source of oxidation	70
5.2	Synthesis of nanoparticles in gaseous, liquid and supercritical CO ₂	71
5.2.1	TEM analysis of nanoparticles synthesized at 10 MPa, 50 °C.....	71
5.2.2	Phase analysis and band gap of nanoparticles.....	73
5.2.3	Analysis of experimental parameters – Effect of CO ₂ pressure and temperature.....	76
5.3	Discussion on materials science of nanoparticle synthesis by PLA at high-pressure	81
5.3.1	Origin of difference in nanoparticle phase and effects of solvent pressure in PLA.....	81
5.3.2	Formation of TiO ₂ -carbon core-shell nanoparticles by PLA in pressurized CO ₂	83
6	Concluding remarks and suggestions for future work.....	86
	Bibliography	88
	Appendix	101
	Publications	107

ABBREVIATIONS AND SYMBOLS

ABPR	Automatic Back-Pressure Regulator
BSE	Back Scattered Electron
CNT	Carbon Nanotubes
DFT	Density Functional Theory
ED	Electron Diffraction
EDS	Energy Dispersive Spectroscopy
HR-TEM	High Resolution Transmission Electron Microscopy
LFL	Laser Fragmentation in Liquids
LIDAR	Light Detection And Ranging
LML	Laser Melting in Liquids
LP	Laser Power
MBE	Molecular Beam Epitaxy
NIR	Near Infrared
PLA	Pulsed Laser Ablation
PLAL	Pulsed Laser Ablation in Liquids
PLD	Pulsed Laser Deposition
SAXS	Small-Angle X-Ray Scattering
scCO ₂	Supercritical Carbon Dioxide
scH ₂ O	Supercritical Water
STEM	Scanning Transmission Electron Microscopy
TEM	Transmission Electron Microscopy
UV	Ultraviolet
UV-Vis	Ultraviolet-Visible
WAXS	Wide-Angle X-Ray Scattering
XPS	X-Ray Photoelectron Spectroscopy
XRD	X-Ray Diffraction
τ_{e-p}	time taken for energy transfer from photons to phonons
I	laser power density

$r_b(t)$	cavitation bubble radius at time t
$p_b(t)$	bubble pressure at time t
$\hat{p}(t)$	pressure at a distance far from the bubble
S	surface tension
ν	kinematic viscosity
ρ	density of the surrounding fluid
p_b	internal bubble pressure
$p_v(T_b)$	vapor pressure at T_b
T_o	temperature at a large distance from cavitation bubble
γ	isentropic expansion factor
p_{G0}	pressure of a bubble before laser irradiation
r_0	radius corresponding to p_{G0}
$T_b(R)$	bubble temperature at radius R
a	hard core radius of cavitation bubble
$D_v(R)$	volume-weighted particle size distribution
T_c	Critical temperature
P_c	Critical pressure
2θ	Diffraction angle
CHF_3	trifluoromethane

LIST OF ORIGINAL PUBLICATIONS

- Publication I A. Singh, J. Vihinen, E. Frankberg, L. Hyvärinen, M. Honkanen, and E. Levänen, “Pulsed Laser Ablation-Induced Green Synthesis of TiO₂ Nanoparticles and Application of Novel Small Angle X-Ray Scattering Technique for Nanoparticle Size and Size Distribution Analysis,” *Nanoscale Res. Lett.*, vol. 11, no. 1, p. 447, 2016.
- Publication II A. Singh, J. Vihinen, E. Frankberg, L. Hyvärinen, M. Honkanen, and E. Levänen, “Effect of laser power on yield of TiO₂ nanoparticles synthesized by pulsed laser ablation in water,” *J. Ceram. Sci. Technol.*, vol. 8, no. 1, pp 39-44, 2017.
- Publication III A. Singh, T. Salminen, M. Honkanen, J. Vihinen, L. Hyvärinen, and E. Levänen, “Multiphase Ti_xO_y nanoparticles by pulsed laser ablation of titanium in supercritical CO₂,” *Appl. Surf. Sci.*, vol. 476, pp. 822–827, 2019.
- Publication IV A. Singh, T. Salminen, M. Honkanen, J.-P. Nikkanen, T. Vuorinen, R. Kari, J. Vihinen, E. Levänen, “Carbon coated TiO₂ nanoparticles prepared by pulsed laser ablation in liquid, gaseous and supercritical CO₂,” *Nanotechnology*, vol. 31, no. 8, p. 085602, 2020.

AUTHOR'S CONTRIBUTION

Amandeep Singh, the author of this thesis, was the main author and researcher for all four publications, and responsible for designing and performing majority of the experimental work. The following is description of author contributions in the four publications included in this thesis.

Publication I

The author of this thesis was the main author and researcher of this manuscript. He planned, designed and conducted all laser experiments. He interpreted the TEM, XRD, SAXS results and prepared TEM-based particle size distributions for comparison with SAXS-based particle size distribution. He wrote the manuscript and received expert inputs on TEM and PLAL from co-authors. Jorma Vihinen gave training for laser and scanner use and helped to plan experiments. Erkka Frankberg supervised the study and gave expert inputs on the manuscript draft. Leo Hyvärinen conducted the XRD and SAXS studies. Mari Honkanen did the TEM imaging and analyzed TEM results. Erkki Levänen was the main supervisor for this publication and helped in formulating research questions and planning the experiments.

Publication II

The author contributions for publication II were the same as for publication I except that instead of SAXS, WAXS studies were conducted by Leo Hyvärinen. In addition, Jorma Vihinen and Amandeep Singh, conducted and interpreted laser power measurements, respectively.

Publication III

The author designed the set-up for combination of PLA and CO₂ autoclave, and operated all components of this set-up, with the help of Jorma Vihinen. The author planned and conducted all laser experiments. He made the laser scanner stand with micrometer adjustment for precision in laser focusing, and target stand for correct target height inside the autoclave in front of the sapphire viewport. He also

connected an automatic back pressure regulator to control the depressurization of CO₂ inside the autoclave. The author prepared the nanoparticle samples for HR-TEM, Raman, and XRD. He analyzed the XRD raw data. He interpreted the TEM, Raman, and XRD results and wrote the manuscript with insightful inputs from co-authors on PLAL, Raman, and TEM results. Turkka Salminen conducted Raman spectroscopy of nanoparticle samples and analyzed the Raman results. He also thoroughly commented on PLA, Raman and XRD related parts of the manuscript. Mari Honkanen conducted TEM studies of the samples, analyzed TEM (from Tampere University) and HR-TEM images (from Aalto University), and commented on the manuscript draft. Leo Hyvärinen performed the XRD measurements. Erkki Levänen supervised the study, helped to formulate the structure of manuscript, and commented on the manuscript draft.

Publication IV

The author planned and conducted all laser experiments. The author designed the combination of PLA and CO₂ autoclave, and operated all components of this set-up. He prepared the nanoparticle samples for (S)TEM, Raman, and XRD analysis. He conducted the tests numerous times to produce sufficient nanoparticle quantity for bandgap studies. He characterized the samples with XRD and analyzed the raw data. He interpreted the STEM, XPS Raman, XRD and bandgap results. He wrote the manuscript with insightful inputs from co-authors on discussion of Raman and STEM results. Turkka Salminen did the Raman spectroscopy measurements, analyzed the Raman results, helped with interpretation of XPS results, and gave insightful comments on the prepared manuscript draft. Mari Honkanen did (S)TEM imaging for nanoparticle samples, analyzed STEM, BSE topography images, conducted line and spot line elemental analysis of nanoparticles. Mari Honkanen commented on the prepared manuscript and gave expert comments for the TEM part. Juha-Pekka Nikkanen and Tommi Vuorinen did the band-gap measurements. Risto Kari helped with the ablation in CO₂ experiments. Jorma Vihinen helped with the laser set-up and its training. Erkki Levänen supervised the study, helped to formulate the structure of manuscript, and commented on the manuscript draft.

1 INTRODUCTION

Laser is arguably one of the most commonly used acronyms. Laser is short for light amplification by stimulated emission of radiation. The story of laser started when Albert Einstein in his 1917 work ‘Quantum theory of radiation’ laid the theoretical foundation of modern laser [1]. After Theodore Maiman in 1960 demonstrated the first operatable laser, which was a pulsed laser, his peers disparaged his invention saying, “A laser is a solution seeking for a problem” [2]. Today, the applications of pulsed lasers transcend almost all fields involving science and engineering. In the transportation section, Light Detection and Ranging (LIDAR) technology has made possible the concept of self-driving cars. The technology developed by NASA to meticulously adjust rockets in their final position for launch was applied for eye surgery several decades later. An early experiment in 1998 demonstrated the generation of fusion reaction using femtosecond laser at 10^{18} Wcm⁻² [3]. 20 years later in 2018, ultrafast pulsed lasers made possible the demonstration of micro-scale nuclear fusion with record neutron generation efficiency by heating ordered nanowires to produce plasma [4]. Nobel prizes in Physics 2018 was awarded to three scientists involved with pulsed lasers research, Donna Theo Strickland, Gérard Mourou and Arthur Ashkin. The impact and supremacy of pulsed lasers took these scientists to the pinnacle of recognition in sciences. In astrophysics, without pulsed lasers as guide stars in the state-of-the-art telescopes, the imaging of super massive black holes would still be a dream. Pulsed lasers have transformed the technology sector especially. To illustrate the point from a very pragmatic example, the Apple iPhone would not be possible without pulsed lasers.

70 years after Einstein’s ‘Quantum theory of radiation’, in 1987, Ogale et al. discovered ‘pulsed-laser-induced reactive quenching’, now commonly known as ‘pulsed laser ablation’ (PLA) when they shot laser pulses onto a solid target dipped in liquid [5,6]. Currently, PLA in liquids (PLAL) has been established as a well-known and promising technique for nanoparticle synthesis [7]. With lasers, we can achieve high energy density, which leads to extremely high local temperatures ($\sim 10^4$ K) on a solid target upon irradiation. The intensity of sunlight that we receive on earth is about 0.1 W/cm². Pulsed laser beams are one of the most intense forms of light.

With nanosecond lasers, the intensity of light is usually around 10^8 W/cm², which is a billion times (10^9) more compared to what we perceive from sunlight. The intensity of light represents the number of photons in the laser beam. The wavelength (λ) of photons, same as the wavelength of laser used, defines the energy of each photon by the well-known relation $E=hc/\lambda$. The nanosecond lasers at about 10^8 W/cm² might have high intensities but they seem to fade when compared to the recently developed state-of-the-art lasers with upwards of 10^{21} W/cm² intensity. One of the highest intensity focused laser in the world '**Hercules Petawatt laser**' at University of Michigan in USA can generate a laser beam of 2×10^{22} W/cm² intensity.

In this study, nanosecond pulsed lasers were used in PLAL in H₂O as well as in PLA in supercritical CO₂ (scCO₂) for synthesis of titanium oxide nanoparticles under varying process conditions, in order to understand the effect of process parameters. Initial studies were done with PLAL technique in its traditional and simplest form i.e. using deionized water as the solvent, to get the know-how of the technique. Later, we explored possibilities for using scCO₂ as a potential promising solvent for controlling nanoparticle phase and morphology of Ti_xO_y nanoparticles while utilizing CO₂ in the PLA process. For this, we built our own 'PLA in scCO₂ high-pressure system' at Tampere University, Finland.

In this chapter, the aim of the study is highlighted. Further, the structure of the thesis is explained, and the main research questions of this thesis are underlined.

1.1 Aim of the work

This thesis was started to test the abilities of PLA in producing nanoparticles and based on hypothesis that we can decompose CO₂ into carbon nanostructures with pulsed laser. CO₂ is a well-known global warming gas. If it were possible to utilize CO₂ and convert it into carbon nanostructures such as graphene, carbon nanotubes (CNT), C-60 or particles with carbon coating, it could help establish a nanomaterial synthesizing method with carbon negative footprint. Since no molecular precursors are needed in PLA based synthesis, this may lead to lower reagent costs and energy requirement [7,8]. A reader interested in detailed economic comparison between wet chemical synthesis and PLA based synthesis is recommended to read the study by Zhang et al. [7].

The aim of this work was to synthesize TiO₂ nanoparticles by PLA starting from using H₂O as the medium and studying the process parameters. As the solvent plays an important role for the synthesis process in PLAL, there was interest to see the

effect of supercritical state of CO₂ on ablation of titanium and on the produced nanoparticles while keeping the laser parameters and ablation material same as in PLAL in H₂O. Further, there was the big question whether it is possible to decompose CO₂ to oxidize the titanium target to titanium oxides nanomaterial or further add carbon to the nanostructures. For this, we varied two main solvent parameters, the pressure and the temperature of CO₂, to observe if this affects the nanoparticle phase, size, and size distribution. It was scientifically very captivating to explore whether we can introduce carbon in/on/at the nanoparticles of titanium oxides by PLA in pressurized CO₂. Such studies are not previously reported in literature to the best of our knowledge. The main themes of this study are shown in figure 1.

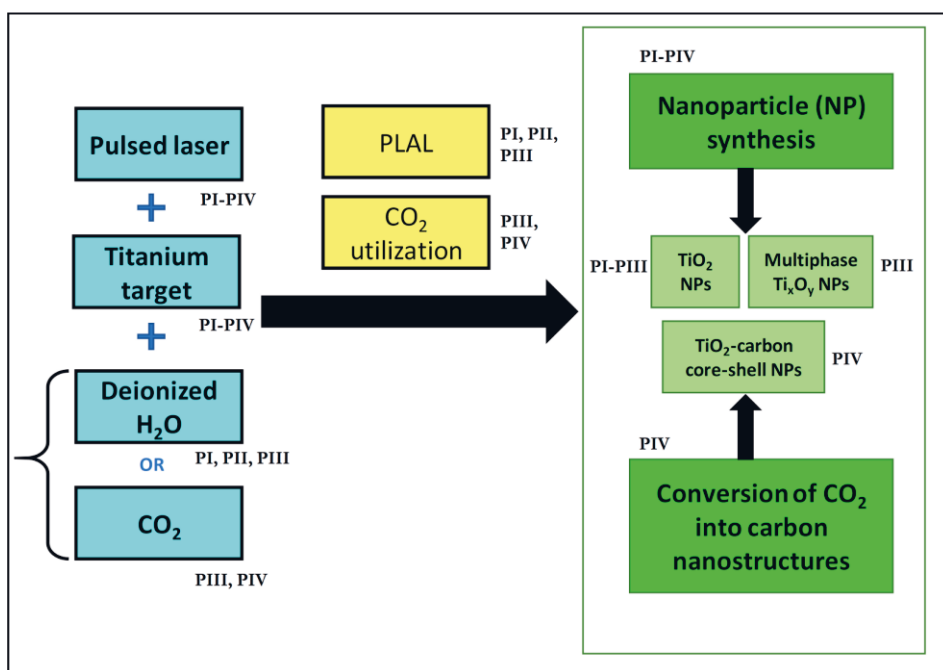


Figure 1. The main themes of this thesis and their order are illustrated. Here Px refers to article numbered x, where x is I–IV.

1.2 Structure of the thesis

This thesis is divided into chapters and the beginning of each chapter consists of a brief summary of the topics discussed in the chapter. A reader, who is curious to

have a quick overview of the chapters, is recommended to read the introduction to the respective chapters.

The thesis starts with an introduction to the thesis in chapter 1. The chapter 2 focuses on the motivation of thesis and state-of-the-art, why PLA in liquids and supercritical fluids is so interesting for nanoparticle synthesis. The analytical techniques and processing methods used in this study are listed in chapter 3. The results and discussion section is spread over chapters 4 and 5. Chapter 4 consists of results from PLA in H₂O and is closely related to publications I and II mostly, and somewhat publication III. Chapter 5 consists of results from PLA in liquid, gaseous and supercritical CO₂ and is closely associated to publications III and IV. The conclusions are presented in chapter 6 along with some suggestions for future work to advance this field.

1.3 Scientific contribution of thesis

This thesis, firstly, contributes to a comparative analysis of TEM and SAXS measurement techniques for determining the size and size distribution of PLAL (in H₂O) produced TiO₂ nanoparticles. We demonstrated SAXS as a quick, promising method for nanoparticle size and size distribution measurement. Further, this thesis contributes to synthesis of multiphase titanium oxide nanoparticles directly as well-dispersed non-agglomerated dry nanoparticle powder by PLA scCO₂. Another important scientific contribution of this thesis is the comparative analysis of PLA in H₂O and PLA in scCO₂ which suggests that while major phase in water studies was agglomerated, stable phase rutile-TiO₂, on the other hand well-dispersed non agglomerated nanoparticles consisting of meta-stable phase (mostly anatase-TiO₂) are favored by PLA in scCO₂, under the same laser parameters. Further, an important contribution of this study is the demonstration of possibilities of solvent control (by changing pressure and temperature of CO₂) of PLA process on the size and phase of synthesized nanoparticles, and possibility to make core-shell nanoparticles by single step dry process. We first reported PLA of a reactive metal in scCO₂ for synthesis of TiO₂-carbon core-shell nanoparticles by PLA in gaseous, liquid and supercritical CO₂. These novel contributions of this thesis are evident from the results and discussion in chapters 4 and 5.

2 BACKGROUND OF NANOMATERIALS SYNTHESIS BY PULSED LASER ABLATION

This chapter reviews the background of TiO_2 nanoparticles, synthesis methods of nanoparticles and PLAL technique for nanoparticle synthesis. Further, the effects of PLAL process parameters are discussed based on literature. This is followed by discussion on concept of supercritical fluids and the latest research when PLAL is combined with scCO_2 . In the end, the research gaps are highlighted that form the basis of the research questions of this study.

2.1 TiO_2 nanomaterials

TiO_2 has been widely studied in the past few decades, ever since the demonstration of its photocatalytic activity by Fujishima and Honda in 1972 [9]. The applications include water purification [10], air purification [11,12], solar cells [13], batteries [14], TiO_2 has been used as a functional material for self-cleaning and anti-fogging surfaces owing to its photo-induced superhydrophilic properties, and in anti-bacterial applications [11,15]. Other applications of TiO_2 include their use in sunscreens [16], teeth whitening solutions [17,18], and as pigments [19]. A classification of some common applications of TiO_2 nanomaterials is shown in **figure 3**. For TiO_2 , the important factor in influencing the photocatalytic activity is the ratio of the surface charge carrier transfer rate to electron-hole recombination rate [20]. Another factor is the particle size. Typically, smaller size leads to larger specific surface area, leading to higher surface-active sites. The lower size limit to his rule is about 10 nm. For particle size smaller than 10 nm, according to Zhang et al, the catalytic activity decreases due to higher recombination rate [21].

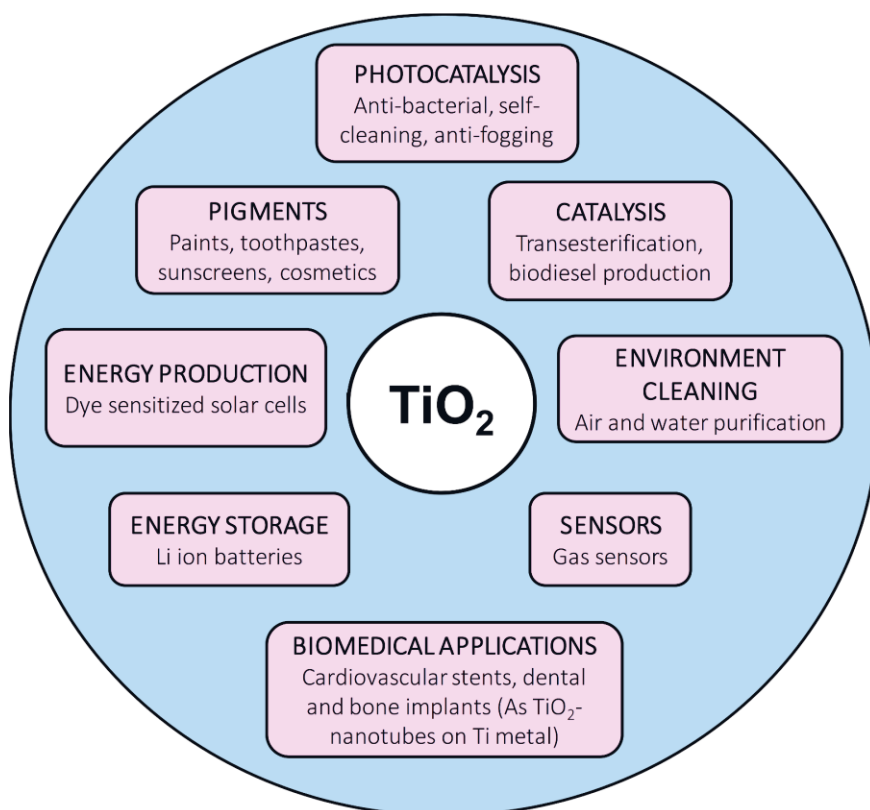


Figure 3. Classification of some common applications of TiO_2 nanomaterials.

TiO_2 occurs as three main allotropes; rutile, anatase, and brookite. It is well known that rutile is the most stable and common, naturally occurring form of TiO_2 . It is the most widely used titanium oxide with its use as a pigment. The band gap energy of rutile is about 3.0 eV. Anatase has a band-gap energy of 3.2 eV. While rutile is more stable than anatase on macroscopic level, nanosized anatase has a higher stability. The third allotrope, brookite, is difficult to produce in pure form, and is the rarest naturally existing form of titania. Like other allotropes, brookite is photocatalytically active. However, the problem with TiO_2 as a photocatalyst is its high bandgap energy of around 3 eV between its conduction and valence band. Several attempts have been made to decrease the bandgap energy by doping TiO_2 . Briefly overviewing, the absorption of TiO_2 in the visible range has been improved by doping with transition elements (V, Co, Cr, Mn, Fe, and Rh) [22], and non-metals (such as C, N) [23,24]. In another study, production of dopant free multiphase titanium oxide nanomaterials by femtosecond laser ablation was reported to cause narrowing of the band gap to 2.39 eV [25,26]. Zuñiga-Ibarra et al. reported synthesis of black- TiO_2 nanoparticles

with a bandgap of 1.84 eV by irradiating white-TiO₂ nanoparticles using PLAL technique [27]. Lowering the bandgap energy of TiO₂, however, is not the aim of this study.

Currently, the demand of nanomaterials is soaring, however, the methods used for their production are not sustainable. Even the chemical industry is underlining the innovation of more sustainable methods of nanoparticle production [28]. The traditional chemical synthesis techniques involve a “precursor reaction or ligand exchange”[29], which usually renders the nanoparticles contaminated and introduces several problems such as catalytic deactivation [30], toxicity [31], and aggregation [32,33]. In this context, PLAL has been reported as a clean, sustainable and promising method for producing nanoparticles [29]. This technique complies with the twelve principles of green chemistry [29,34,35]. The nanoparticles produced by PLAL are high purity, ligand-free and ready for functionalization [35–37]. Further details to this technique are mentioned later in section 2.3.

This thesis study also involves synthesis of core-shell nanoparticles, which are sometimes also called nanoshell particles or core@shell particles. Core-shell nanoparticles have gained significant interest recently due to their unique, novel properties that are different than their single-counterpart. With small changes in the size, morphology or ratio of core to shell, the properties can be customized according to the desired application [38]. Traditionally, the techniques used for their synthesis mostly include polymerization [39], and sol-gel [40] (Chemical techniques), or plasma-based synthesis [41,42], flame synthesis [43], or spray pyrolysis [44] (physical methods), or then chemical vapour deposition techniques [45]. PLAL technique is another physical method for production of core-shell nanoparticles [46], that is single step, involves little sample preparation and is an in-situ synthesis technique. Additionally, unlike some chemical techniques, it does not utilize environmentally hazardous solvents. This may mean further cost saving when compared to the chemical methods, since there is no need of any chemical waste management.

The extensive applications of core-shell particles have been summarized in several review articles, such as by Kalele et al. 2009, where the use of core-shell nanoparticles for colorimetry and biosensing, colloidal stability, catalysis, and for photonic band gap materials has been described in detail [38]. Core-shell nanoparticles are used in the energy sector (for batteries, solar cells, and supercapacitors), medical biotechnology (such as for cancer treatment, and molecular bioimaging), and in electrocatalysis [47–49]. Since this thesis deals with synthesizing TiO₂ nanoparticles both normal (particles made of only one material)

and core-shell (TiO_2 core with carbon shell), it is pertinent to mention some excellent properties exhibited when TiO_2 is combined with carbon nanostructures. Combination of TiO_2 with graphene has been reported to form a new electronic platform capable of double functionality of photosensitivity and field effect in FETs (such as bottom gated field effect transistors) [50]. Lee et al. reported the use of TiO_2 -carbon core-shell structures as a support material increased the catalytic activity and stability of Pt catalyst, used in a fuel cell [51].

In the next section, PLA and PLAL technique will be discussed in detail and mechanisms of nanoparticle synthesis will be explained.

2.2 Pulsed laser ablation (PLA)

The ejection of material from a target upon irradiation by an intense ultrashort-pulsed laser beam is termed as pulsed laser ablation or simply PLA [52]. The removed material is in the form of high-temperature high-pressure plasma. The temperature and pressure in this plasma plume is around 10^4 K and ~ 1 GPa, respectively. Ablation happens because the energy of the laser beam is higher than the binding energy between the atoms of the target material. The electrons in the target material, upon absorbing energy from the oncoming photons, transfer the energy to phonons that are lattice vibrations and cause heating of the material. This sudden intense heating of the target leads to expulsion of target species to form plasma containing ablated ionized species. This phenomenon is known as vaporization and explosive-boiling and will be discussed later. When the surrounding medium is vacuum or a gas, pulsed laser ablation is a well reported method to synthesize thin coatings, and the process is called pulsed laser deposition (PLD). Depending on the ambient gases, it is possible to form both stoichiometric as well as non-stoichiometric coatings by PLD. When the surrounding medium is a liquid, the technique is called pulsed laser ablation in liquids or simply PLAL, as mentioned before. There are other plasma based processes for nanoparticle synthesis such as high temperature plasma processes like AC and DC systems, and pulsed RF systems, while low temperature plasma processes include microwave systems (GHz) and RF systems (MHz) [53]. However, in this study, we will focus on PLAL.

Laser ablation is a simple and quick process that can effortlessly be employed to produce nanoparticles without any fundamental understanding of the underlying principles governing it. Due to this, the technique had been widely accepted in the industry before any breakthrough studies were made on the interaction between light

and matter, especially at extremely high intensities of light. In photonics, it is commonly known that the energy profile of the laser beam has a significant effect on the synthesis of quantum dots by laser interference patterning followed by molecular beam epitaxy (MBE) growth [54]. However, when the aim is to synthesize nanoparticles, the process is less sensitive to the energy profile of the beam.

2.3 PLA in liquids (PLAL)

2.3.1 PLAL and nanoparticle formation

Ogale et al. discovered PLAL in 1987, when they irradiated a metallic target using a ruby laser (30 ns, 694 nm) to form metastable phases, for which they used the term ‘pulsed-laser-induced reactive quenching’ [5,6]. However, it was not until 1993 when Nedderson et al. used the term nanoparticle for the first time for the particles formed by irradiating with a 1064 nm Nd:YAG laser [55]. To date, similar experimental set-up is used to form nanoparticles by PLAL as was described in this pioneering study.

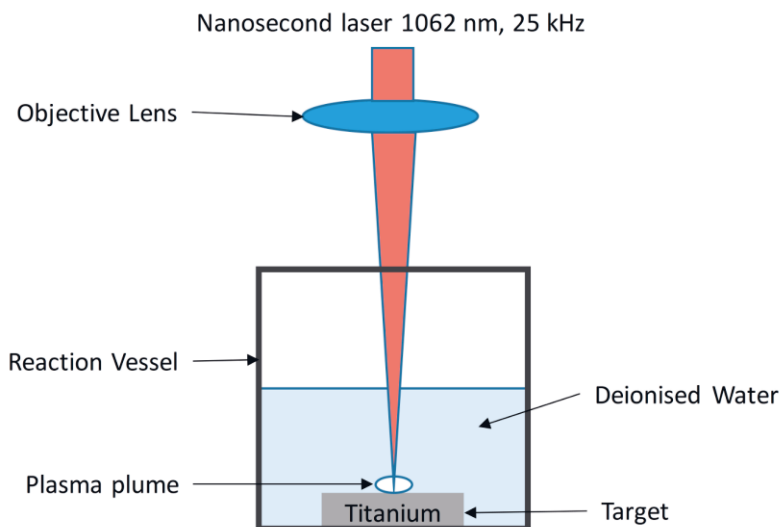


Figure 4. Basic set-up for PLAL of Titanium in deionized water. Figure from Publication I.

For PLAL, the basic set-up, as shown in **figure 4**, consists of a target dipped in liquid, a pulsed laser, an objective lens to focus the laser and an XY scanner to scan the laser beam. PLAL enables synthesis of metal, metal oxide, carbon nanoparticles with no by-products [52,56,57]. PLAL typically does not involve any chemicals, due

to which it is an environment friendly process. Nanoparticle formation in PLAL (**figure 5**) can be understood in following steps:

1. Laser pulse penetrates the liquid above the target.
2. Laser pulse gets absorbed by the target.
3. The ablated target material ionizes and gets detached from the target surface to form plasma.
4. The laser induced plasma plume expands and quenches, giving rise to cavitation bubble.
5. Cavitation bubble expands wherein the nanomaterials may nucleate and grow. This is followed by bubble collapse to release nanoparticles in surrounding liquid.
6. Nanoparticles grow and agglomerate in the ambient liquid. [58]
7. The nanoparticles undergo further laser processing in case of batch type process. [59].

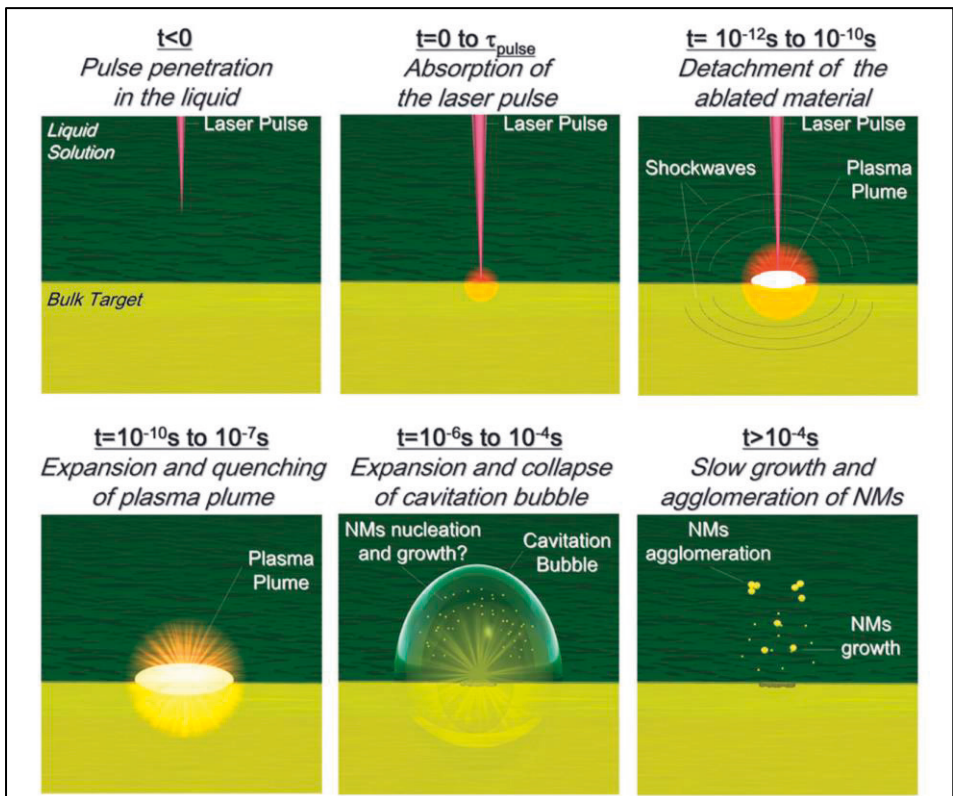


Figure 5. Schematic showing timeline for nanoparticle formation during PLAL. Figure adapted from reference [58].

2.3.2 Types of nanoparticles by PLAL

Nanoparticles of ‘library of materials’ comprising almost the whole periodic table can be synthesized by PLAL [58]. The elements highlighted in yellow colour in **figure 6** indicate the elements of the compounds in the nanoparticles that have been demonstrated so far by PLAL [58]. In the past, there have been reports of formation of nanoparticles from gold [60–62], silver [55,63,64], platinum [65,66], copper [67–71], titanium [68,72], zinc [70,73–75], aluminium [76], magnesium [70], lead [70], iron [6,66,70], nickel [70,77,78], palladium [79], manganese [80], tungsten [64,81,82], tin [83], silicon [82,84], germanium [82], and carbon [85]. With the choice of these targets, and different solvents such as water, ethanol, toluene, cyclohexane, cyclopentane, chloroform, acetone, n-hexane, or methanol, it is possible to engineer different compositions of nanoparticles [52].

H																	He	
Li	Be											B	C	N	O	F	Ne	
Na	Mg											Al	Si	P	S	Cl	Ar	
K	Ca	Sc	Ti	V	Cr	Mn	Fe	Co	Ni	Cu	Zn	Ga	Ge	As	Se	Br	Kr	
Rb	Sr	Y	Zr	Nb	Mo	Tc	Ru	Rh	Pd	Ag	Cd	In	Sn	Sb	Te	I	Xe	
Cs	Ba	*	Lu	Hf	Ta	W	Re	Os	Ir	Pt	Au	Hg	Tl	Pb	Bi	Po	At	Rn
Fr	Ra	**																
		*	La	Ce	Pr	Nd	Pm	Sm	Eu	Gd	Tb	Dy	Ho	Er	Tm	Tb		
		**	Ac	Th	Pa	U	Np	Pu	Am	Cm	Bk	Cf	Es	Fm	Md	No		

Figure 6. The elements highlighted in yellow colour in the Periodic table specify the key elements of the compounds synthesized by pulsed laser ablation in liquids Adapted from reference [58].

Further, there are several morphologies of nanoparticles reported using PLAL technique. The simplest morphology formed is the crystalline sphere. During laser processing, reactive, soluble or supersaturated seed concentrations may produce non-spherical nanomaterials by undergoing ripening [29]. This then leads to morphologies such as flower-like [86,87], fractal [88], fullerene-like [89], leaf-like [81], hexagonal [90], tubular [91], hollow [72,74,76,92,93], core-shell [77,94–97],

nanonecklaces [62], nanoribbon [98], nanospindle [73,99], nanosheet [100–102], nanowire [103–105], nanodisk [106], and nanocube [70,107–109].

Efforts to understand nanoparticle formation

Significant efforts in terms of collaborative research have been ongoing to understand the nanoparticle formation mechanism in PLAL, such as the collaborative research from University of Virginia, USA and University of Duisburg-Essen, Germany. Using atomistic modelling of PLAL for Ag in H₂O and cavitation bubble imaging experiments for Au in H₂O, Shih et al reported new insights into the picosecond laser ablation and explained the origin of bimodality of nanoparticle size distribution in PLAL. [110,111]. Shih et al developed atomistic simulations for laser ablation of thin silver films in water medium at two laser fluences (400 and 700 J/m²) in phase explosion regime to provide microscopic insight to nanoparticle formation in PLAL. The molecular dynamics simulations indicated that in both nanoparticle formation mechanisms, dense superheated liquid metal layer forms at water-plume surface that transforms an interfacial region of water into supercritical water. This subsequently forms a low-density metal-water mixing region which then quickly expands and acts as precursor for cavitation bubble formation later. This is followed by rapid nucleation and growth of nanoparticle in the mixing region on a timescale of a few nanoseconds. The breakdown of the superheated layer then constitutes to the second nanoparticle formation mechanism leading to formation of nanoparticles that are several tens of nanometers in diameter. This occurs on a much longer timescale than the first nanoparticle formation mechanism. [110] These are the two main nanoparticle formation mechanisms in PLAL that cause bimodality of nanoparticle size in PLAL.

Unique applications for PLAL synthesized nanoparticles

Highly pure, clean, and ligand free nanoparticles formed by PLAL can especially be good for biomedical and optoelectronic applications. Recently, the use of PLAL produced nanoparticles to produce “nanoparticle-metal composite powders for laser additive manufacturing of oxide-dispersion strengthened alloys” was demonstrated [112]. PLAL synthesized nanoparticles can have several advantages over chemically synthesized nanoparticles, such as augmented conjugation efficiency, higher grafting density, catalyst functionalization, and increased electro affinity for charged biomolecules [29].

2.4 Effects of PLAL process parameters

2.4.1 Effects of laser parameters

Effect of pulse wavelength

Different target materials have different absorption for different wavelengths of light. The skin depth, also known as the absorption coefficient, of target material depends on the wavelength of the laser pulse [58]. In this study, the inherent beam was 1064 nm and turning it to second harmonic would reduce the beam energy and the laser fluence may also decrease depending on the optics.

If the already synthesized nanoparticles absorb laser pulses, they can go through additional modifications [35]. Depending on the phase composition, the wavelength absorbed by nanoparticles may vary. While ultraviolet (UV) irradiation is uniformly and efficiently “absorbed by interband transitions in metal targets” resulting in uniform erosion of spot area irradiated, many studies reported near infrared (NIR) radiation is absorbed by impurities and defects in target preferentially, leading to a non-uniform erosion on spot area irradiated [58,113,114]. However, study by Leyder et al. demonstrated that the laser energy deposition does not depend on the doping concentration of the target. In their study, a 130 fs laser at 1.3 μm was used while the doping concentrations in the target were varied from 10^{13} cm^{-3} to 10^{18} cm^{-3} [115].

Effect of number of overlapping pulses

Depending on the pulse duration, repetition rate and the scanning speed of the laser used, the most studied number of overlapping pulses vary from 1 – 100,000. For repetition rates higher than 100 kHz, when the pulses are overlapping, the laser pulse hits the plasma plume and cavitation bubbles formed by the previous pulse. This further complicates the understanding of the nanoparticle synthesis phenomenon. The overlap of laser beam and plasma plume further increases the temperature of the plasma species due to absorption of laser energy by plasma plume. However, the disadvantage is that plasma plume also optically shields the target surface from the incident laser beam [35]. The overlap of laser beam with the plasma may occur only when the repetition rate is over 100 kHz since the plasma duration does not exceed 10 μs [116] even though the bubble duration can reach 100-300 μs .

Effect of repetition rate

The time delay between two laser pulses is defined by the repetition rate of the laser. The higher the repetition rate, the smaller the time lag between two pulses. Generally, an increase in the repetition rate causes an almost linear increase in the nanoparticle yield, if the time delay is longer than the cavitation bubble lifetime [58]. This could inversely mean that in case of PLA in pressurized fluids, due to much shorter bubble lifetime compared to PLA in normal pressure fluids, a higher repetition rate could be used. This could lead to higher nanoparticle yield for PLA in pressurized fluids than in atmospheric pressure fluids. However, after the aforementioned linear increase in nanoparticle yield, the non-linearity of yield when the time delay is shorter than bubble lifetime does not account for decreased pulse energy at higher repetition rates. Only at a fixed pulse energy, the influence of the repetition rate can be meticulously understood [7]. Zamiri et al. studied PLAL of Ag in water at a fixed pulse energy of 60 mJ and varying repetition rates of 10–40 Hz and reported a linear increase in the nanoparticle yield with increasing repetition rate [117]. The time delay for the repetition rates from 10 to 40 Hz (corresponding to 25–100 ms) was much longer than the bubble lifetime, which were <1 ms.

Effect of pulse duration and pulse energy

The pulse duration (same as pulse length) strongly influences the nanoparticle size, size distribution and nanoparticle formation mechanism. Depending on the pulse duration of the laser, the nanoparticles can form either by **photothermal** or by **Coulomb explosion mechanism**. In *photothermal mechanism*, the particle is heated to temperatures above its boiling temperature and surface atoms start to vaporize. This phenomenon in PLAL experiments for batch cell processes falls in the domain of laser melting in liquids (LML). In *Coulomb explosion* mechanism, the pulse length is smaller than the coupling time of electron-phonon (of nanoparticle material). Due to this, the electron temperature¹ significantly increases without any change in lattice temperature due to which electrons are ejected out from the solid target or particle under consideration. The sudden change of charge causes immediate fragmentation/explosion due to internal charge repulsion. So, when the disruptive Coulomb force surpasses the cohesive force, the particle becomes unstable and fragments [7]. This phenomenon falls in the domain of laser fragmentation in liquids

¹ Electron temperature is the temperature of the energy distribution function (Fermi-Dirac statistics) of the velocity of the electrons.

(LFL), in PLAL for a batch cell process. The effect can be discerned from figure 7 (a). Further, when a colloidal solution of nanoparticles is subjected to PLA, the size reduction mechanisms depends on laser parameters such as pulse energy and pulse width and particle parameters such as initial particle cohesion (such as binding energy, heat capacity, volume) [7]. In general, increase in laser fluence and irradiation time leads to decrease in particle size when nanoparticle suspensions are ablated with pulsed laser.

The threshold laser fluence of a material is a function of the pulse width of the laser. For the same nanoparticle material in case of plasmonic particles, the threshold laser fluence is exceptionally lower when ablated with a femtosecond laser compared to a nanosecond laser for particle sizes less than 50 nm [29,118]. This is evident from figure 7 (b). Also, observable is that the size of particle under the laser beam affects the threshold laser fluence. Same-size particles behave differently under femtosecond and nanosecond laser. As particles size decreases, the threshold laser fluence decreases with an exception in case of nanosecond laser. According to figure 7 (b), for nanosecond PLA, when the nanoparticle size is less than a threshold size, the threshold laser fluence increases significantly with the decrease in nanoparticle size.

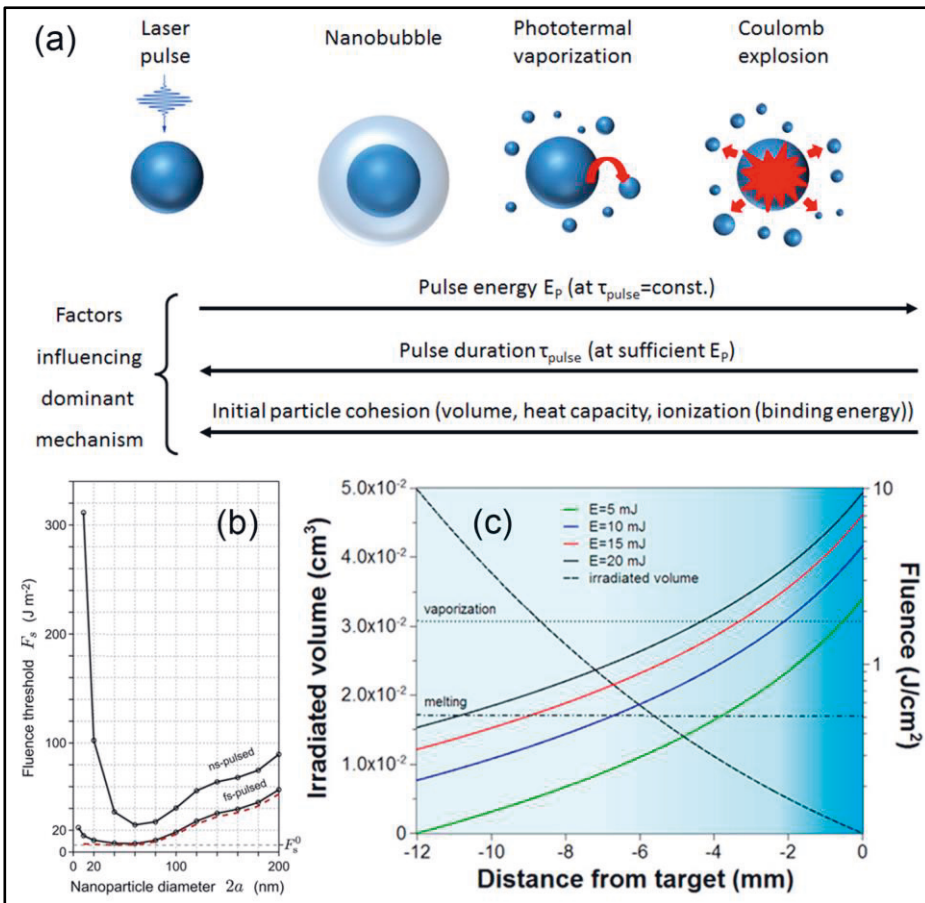


Figure 7. (a) Schematic for size-reduction/fragmentation mechanisms of nanoparticles with PLA, (b) Threshold laser fluence as a function of nanoparticle size and pulse width, (c) Attenuation of laser beam (for several fluences) along the optical path in liquid with the distance from the target Adapted with permission from reference [7,118,119]. The data in the above figure is based on results for plasmonic particles.

2.4.2 Material type

The library of materials that can be used in PLAL extends across almost the whole periodic table. Based on that and solvent selection, we can make either that element's native form nanoparticles or its oxide or carbide depending on the medium used. The list of nanoparticles that can be made by PLAL are highlighted in section 2.3.2.

2.4.3 Effect of ablation medium on laser beam during PLAL

The solvent has a strong influence on the composition of the nanoparticles. When the plasma implodes and cavitation bubble is formed, the ionized target species react with the ionized species of solvent. The final composition of the nanoparticles depends on whether the solute species and solvent species are reactive with each other or not. Further, since the solvents usually contain some amount of atmospheric gases such as O₂, N₂, H₂O and CO₂, the ablated species can and will react with these gases also [58]. The solvent may determine in many cases the nanoparticle composition depending on the target material type, whether it is a low reactivity material such as Au, and Ag, or if it more reactive such as Ti, Al, and Fe.

The solvent may strongly influence the beam attenuation in PLAL, depending on the pulse energy, when the beam penetrates through the liquid and travels the length equivalent to thickness of liquid film above the target. Figure 7(c) vividly shows the increase in the attenuation of laser beams of different pulse energies upon passing through the liquid with increasing thickness of liquid film on top of target. Also evident from figure is that vaporization (of particles under beam) is more prevalent at higher laser fluences especially for higher pulse energies while melting or partial-melting is more prevalent for lower laser fluences [119]. In addition, due to laser penetration of liquid, the focal length also varies which may defocus the beam on target. This is rather complex since for picosecond and femtosecond lasers, self-focusing is also possible.

Further, the solvent acts as a medium for shockwave propagation. The nanoparticles can undergo fragmentation due to laser-induced shockwaves. The laser-induced shockwave generates high pressures in water. The maximum pressure of laser-induced shockwave (P), is related to the laser power density according to the following equation:

$$P \text{ [GPa]} \approx 2.5 \times \sqrt{I \text{ [GWcm}^{-2}\text{]}}$$

where I is the laser power density. It was further reported that with the increase in length of pulse duration in the range 0.6-30 ns, higher peak pressures are obtained for a given laser intensity. [120,121] The oscillating cavitation bubbles as a result of these shockwaves further generate high pressures. These shockwaves can be accompanied by ejection of material in the form of “jets” [122,123].

2.5 Shock wave emission and cavitation bubble phenomenon

Shock wave emission

After absorption of laser energy, target species are emitted to form a plasma plume that expands and pushes the surrounding liquid to form a shock wave that propagates into the target and another shock wave that counter-propagates into the liquid at supersonic speeds ($>10^3$ m/s) [58]. So, the excess energy is released by emission of shock wave. A shock wave is creation of a discontinuity in the fluid variables, such as density of liquid. Shock wave front and propagation of shock wave front can be observed by shadowgraph imaging since it creates a change in the refractive index of fluid at the periphery of wave front. Imploding laser-induced bubbles also emit shock waves that are typically visible in the shadowgraph images, however not as distinctly as the shock waves released upon irradiation with laser [52]. The formation and propagation of these shock waves causes significant dissipation of the laser energy [52]. This means that only a fraction of the energy from the incident laser is absorbed to form plasma plume.

Laser ablation-induced cavitation bubbles

There are two ways by which laser ablation-induced bubbles are formed: (i) one is by cavitation when the pressure of liquid at constant temperature goes under the tension strength of the liquid, (ii) second is when liquid temperature rises to the kinetic limit of superheat (often seen as explosive boiling) [52]. At the solid-liquid interface, PLAL leads to formation of cavitation bubbles that expands at supersonic speed, then implodes and releases shock waves in the system. The nanoparticles are synthesized upon nucleation and growth of atoms and cluster of atoms that collide and aggregate inside the cavitation bubbles [63,124]. This signifies the importance of cavitation bubbles for understanding the phenomenon of formation of nanoparticles. The lifetime of the cavitation bubbles is around multiple hundreds of microseconds after which it collapses and releases the nanoparticles in the surrounding media [125,126]. The collapsing cavitation bubble can further create more cavitation bubble and so on. The energy of each collapsing bubble is sufficient to remove material from the target.

2.6 Supercritical carbon dioxide (scCO₂)

2.6.1 Properties of CO₂

CO₂ is a non-flammable, non-toxic gas that exhibits relatively low reactivity. Due to these ‘green’ properties, CO₂ is highly advantageous environmentally in industrial use to substitute chemicals in processes, especially as supercritical CO₂ (scCO₂). A fluid is in its supercritical state when its pressure and temperature are above its critical point. For CO₂, this critical point (shown in **figure 8**) is at a temperature of 31.1 °C and a pressure of 73.8 bar (7.38 MPa). This is much less than the critical point of H₂O, which is 374 °C and 220.8 bar (22.08 MPa). Beyond this critical point, CO₂ becomes a supercritical fluid, where it is neither gas nor liquid but exhibits properties of both states [127]. Due to its low critical point, it takes less energy to reach its critical point and it can easily be handled safely using a standard high-pressure vessel.

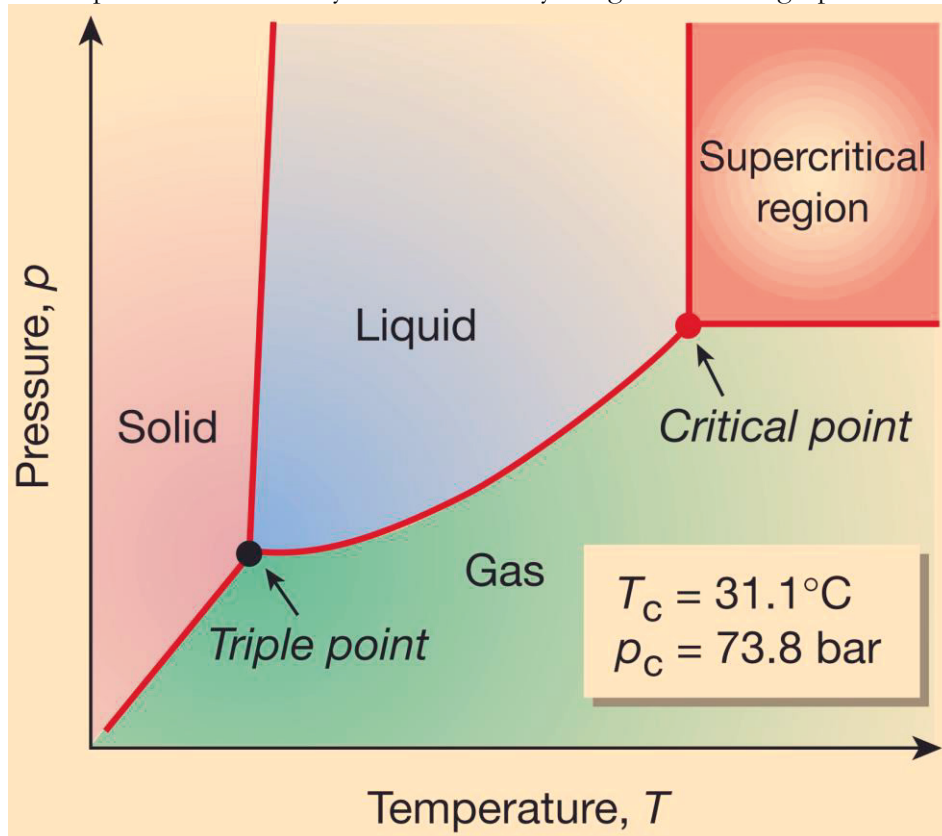


Figure 8. Phase diagram of CO₂ showing the critical point. Adapted from reference [127].

2.6.2 Processing with scCO₂

In the supercritical state, CO₂ has liquid-like density, gas-like diffusivity and zero surface tension. Because of liquid-like density, scCO₂ has a high dissolution power so it can easily dissolve co-solvents. Further, due to its gas-like diffusivity and zero surface tension, CO₂ can penetrate nanostructures, cause the reactions and leave the system without leaving any residue and without affecting the nanostructures. This leads to **application** of scCO₂ processing to synthesize aerogels. scCO₂ processing is one of the most common ways to produce decaffeinated coffee. This technique is widely used for dry cleaning of textiles. scCO₂ is a safe cleaning, degreasing and particle-removing agent and acts as a brilliant alternative for organic solvents, especially for sterilizing applications. By simple manipulations in temperature and pressure, the physical and thermal properties of scCO₂ such as diffusivity, viscosity, and conductivity can be changed from being gas-like to liquid-like or vice-versa [128].

For PLA in scCO₂, CO₂ is recyclable in this process since scCO₂ can be released from the high-pressure chamber as gaseous CO₂ and pumped back into it for further processing. In chapter 5, we will discuss the decomposition of scCO₂ to carbon and oxygen, leading to oxidation of titanium to titanium oxide and presence of carbon layer on nanoparticles. This suggests PLA in scCO₂ as a CO₂ utilization technique for nanoparticle synthesis and may also functionalize the target surface.

2.7 PLA in scCO₂

2.7.1 Generality on bubble dynamics

The next step in the solvent-induced control of PLAL synthesis could be PLA in pressurized fluids. Higher CO₂ pressures have been reported to enhance ablation efficiency. In the field of pressurized fluids, as mentioned earlier, a fluid is in its supercritical state when its pressure and temperature surpass its respective critical point. When combined with PLAL, supercritical fluids, such as scCO₂, have been reported to assist creation of reaction fields which may lead to the formation of exotic, meta-stable phases [129]. **Figure 9** shows a schematic for PLA in high-density CO₂, which is attached to a pulsed laser and automatic back pressure regulator from publication IV.

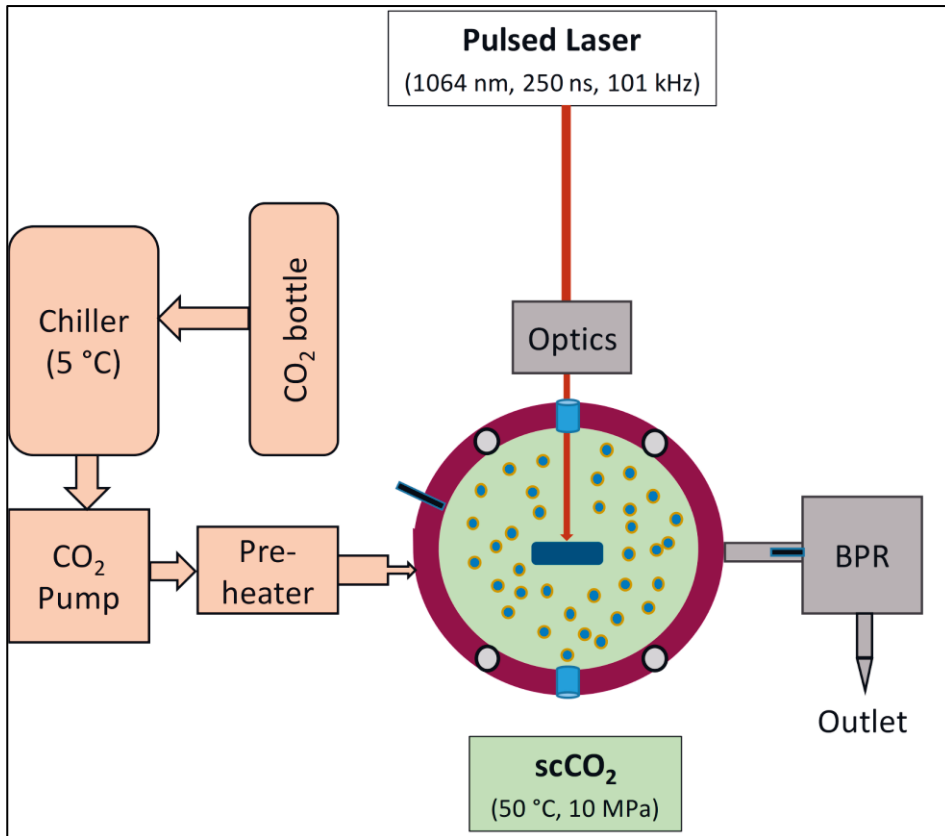


Figure 9. Schematic for PLA in high-density CO₂. Figure Adapted from Publication IV.

Ablation-induced bubble-like optical phenomenon in supercritical fluids has not been studied as much compared to PLAL. While a 2012 study showed shrinking and collapse of cavitation bubbles, a 2014 study reported that the bubble-like hollow inside cavitation bubbles neither shrinks nor collapses [128,130]. Shadowgraph images obtained during PLA in scCO₂ are shown in **figure 10** at delay times of 5 μ s, 100 μ s, and 500 μ s and at CO₂ pressures 5 MPa and 8 MPa at 40 °C [128]. Due to this disagreement, newer experimental studies are indispensable to elucidate the actual phenomenon. It is interesting to know how the difference in the bubble dynamics will affect nanoparticle size, morphology and composition in PLA in scCO₂ compared to H₂O.

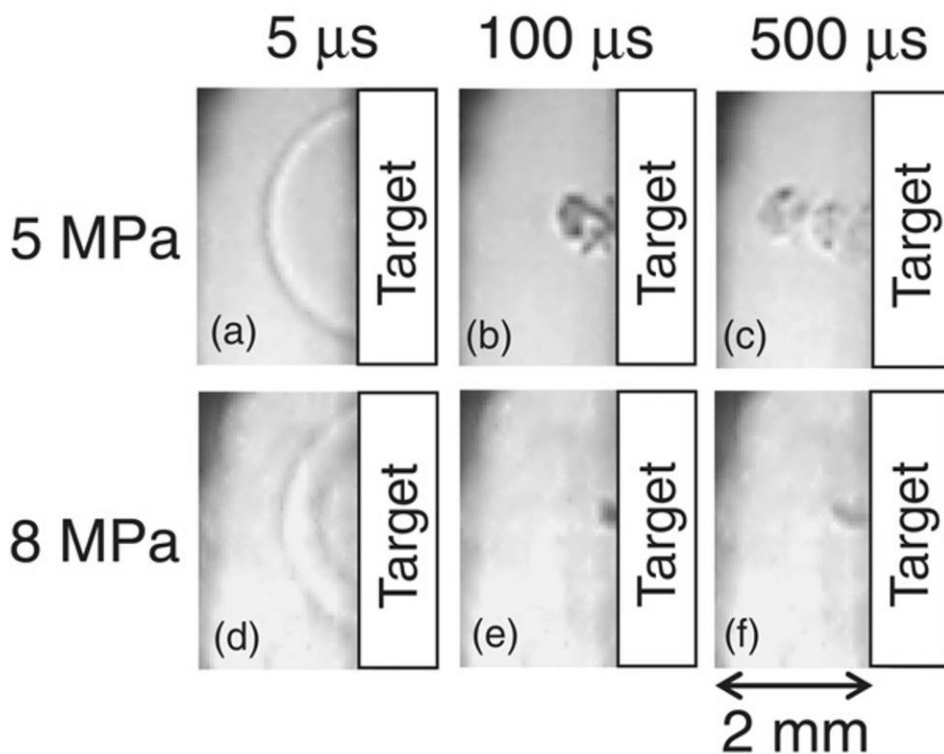


Figure 10. Shadowgraph images from pulsed laser ablation in supercritical CO_2 at delay times of 5 μs , 100 μs , and 500 μs . Figure adapted from reference [128].

Effect of solvent pressure on laser-induced plasma and cavitation bubble

The size of plasma plume decreases as the ambient pressure of the solvent is increased significantly. Sasaki et al. reported 25% decrease in plasma volume when the ambient pressure of solvent was increased from 0.1 MPa to 30 MPa during PLAL of titanium in water [131]. Under the same conditions, Takada et al. observed from the optical emission images the flattening of the plasma plume at increased pressure (30 MPa versus 0.1 MPa) [132]. This effect of pressurization on the plasma plume is illustrated in **figure 11**.

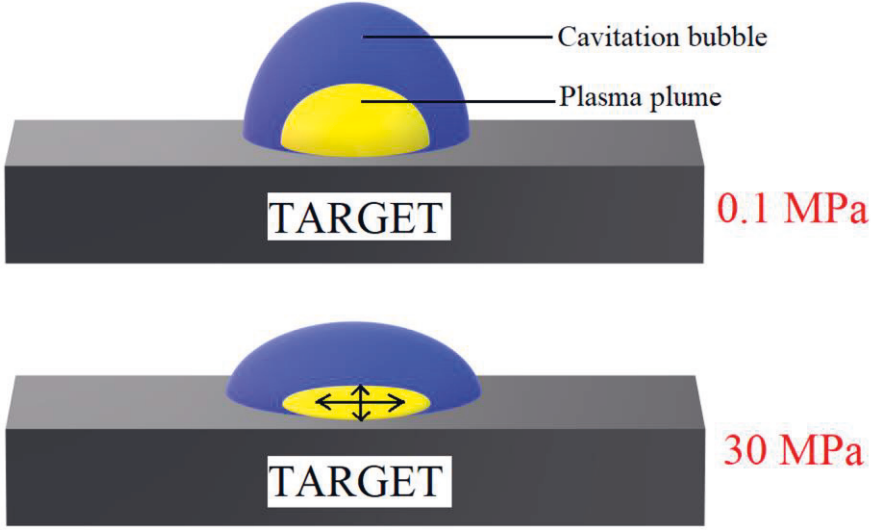


Figure 11. Increased ambient pressure causes plasma plume to become squeezed laterally and it expands parallel to the target surface. In figure, the upper schematic is for 0.1 MPa ambient pressure while the bottom schematic is for 30 MPa. Figure is based on discussion on optical intensity images in reference [132].

The size of the cavitation bubble after expansion can be estimated from the Rayleigh-Plesset equation [133]. Rayleigh-Plesset model can be solved according to following equation to estimate the pressure and temperature inside the cavitation bubble [134]:

$$\frac{p_b(t) - p(t)}{\rho_L} = r_b(t) \frac{d^2 r_b(t)}{dt^2} + \frac{3}{2} \left(\frac{dr_b(t)}{dt} \right)^2 + \frac{4\nu}{r_b(t)} \frac{dr_b(t)}{dt} + \frac{2S}{\rho_L r_b(t)}$$

where, $p_b(t)$ is the bubble pressure at delay time t , and $p(t)$ is the pressure at a distance far from the bubble, $r_b(t)$ represents the cavitation bubble radius at time t , and ρ_L , ν , and S are the density, the kinematic viscosity coefficient, and the surface tension, of fluid, respectively [134,135]. The internal bubble pressure p_b at any time t is given by following equation:

$$p_b(t) = p_v(T_b) + p_{G_0} \left(\frac{T_b}{T_0} \right) \left(\frac{r_0}{r_b(t)} \right)^{3\gamma}$$

where the vapor pressure at temperature T_b is $p_v(T_b)$, T_0 is the temperature at a large distance from cavitation bubble, p_{G_0} and r_0 are the pressure and radius of a

bubble existing in liquid before laser irradiation connected $p_{G_0} = p_o - p_v(T_o) + 2S/r_o$, and γ is the isentropic expansion factor, and calculated as the ratio of the specific heats given as $\gamma = C_p / C_v$ [134,135]. The bubble temperature T_b is given by

$$T_b(r) = \frac{T_0 r_0^{3(\gamma-1)}}{(r^3 - a^3)^{\gamma-1}}$$

where a is the hard core radius of cavitation bubble given by, $a = r_o/8.86$ [134,135]. The assumptions in the above Rayleigh Plesset model are not valid during PLA since the cavitation bubble is neither empty nor spherical in shape. The Rayleigh Plesset model in its simplest form is only acceptable for modelling the first bubble oscillation. Soliman et al. presented a modified Rayleigh-Plesset model that accounted for the “hemispherical nature of the cavitation bubble” and the influence of contact angle between the target, the bubble and the solvent [134]. **Figure 12 (a)** shows decent agreement between the experimentally observed and modified Rayleigh-Plesset model calculated cavitation bubble radius and delay times reported by Soliman et al. [134]. However, the assumptions of varying surface tension and viscosity in the modified Rayleigh-Plesset model could be poorly reliable. The Gilmore model, which accounts for liquid compressibility and acoustic energy dissipation, efficiently explains the bubble rebounds without any dangerous or potentially unreliable assumptions. Barcikowski et al. used the Gilmore model to accurately model the cavitation bubble rebounds and compared it with the Rayleigh Plesset model, which only explained the first bubble collapse accurately [136].

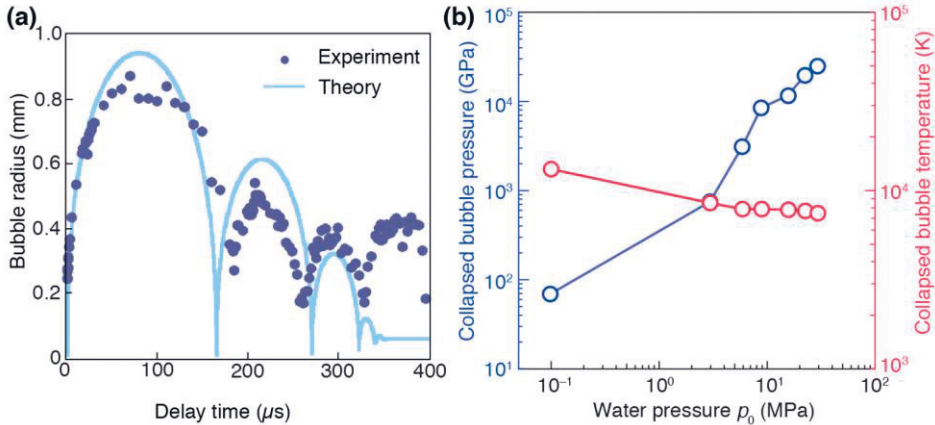


Figure 12. (a) The theoretical estimation from the modified Rayleigh-Plesset model were in agreement with the experimental observations and (b) The effect of water pressure on the cavitation bubble pressure and temperature. Adapted from references [134,135].

The bubble pressure at the time of collapse of the first cavitation bubble is significantly higher when the ambient pressure is higher (**figure 12 (b)**), however, the bubble temperature decreases only slightly [134,135]. In a new 2020 study on bubble dynamics in PLA using shadowgraph imaging, Hupfeld et al. reported variation in the size, temporal shape, and lifetime of laser induced cavitation bubbles, also damping of oscillations when the kinematic viscosity was changed several orders of magnitude. They reported several competing forces that determine the variations in bubble dynamics such as “competition between the viscous forces and surface tension (capillary number)” and “competition between viscous forces and inertia (Reynolds number)”. They summarized that the viscosity of the surrounding liquid in PLA determines the dynamics of the cavitation bubble. [137]

2.7.2 PLA of low reactivity metals in pressurized CO₂

Saitow et al. in 2005 [84] first reported production of nanoparticles by pulsed laser ablation in supercritical CO₂. They reported synthesis of silicon nanoclusters in 2005 [84] and gold nanospheres and nanonecklaces in 2008 [62]. Later in 2009, research led by Motonobu Goto reported on increased ablation efficiency for PLA of copper in supercritical CO₂ [69]. Next in 2011, synthesis of higher diamondoids by Nakahara et al. [138] and synthesis of gold nanoparticles in 2011 by Goto and co-workers [129] was reported. Later, Motonobu Goto’s group reported synthesis of silver and nickel nanoparticles in 2013 [139] and 2016 [78], respectively. There are three main queries or research gaps with these topics.

The **first query** is that, so far, the focus of PLA in pressurized or supercritical CO₂ has been to synthesize nanoparticles of low reactivity metals resulting in no or very limited interaction with the surrounding fluid. The use of low reactivity metal for PLA could be one reason why the interaction of CO₂ with laser induced plasma and hot metal nanoparticles has not been reported much in literature. Although, Mardis et al. observed presence of carbon on nanoparticles [140], it was not further explored in terms of effect of laser induced decomposition of CO₂ or hot nanoparticles causing CO₂ decomposition to adsorb a carbon layer and simultaneously oxidizing the core of particles. The possible mechanisms for CO₂ decomposition and carbon layer formation on nanoparticles remain undiscovered!

The **second query** is the nanoparticle size. For gold nanoparticles synthesized by PLA in pressurized CO₂, both Saitow et al. [62] and Machmudah et al. [129] reported two nanoparticle populations: (a) particles few tens of nanometers in

diameter, (b) particles 300-600 nm in diameter. It has been reported by Saitow et al. in 2012 that the fluid density is one factor that determines whether we obtain nanonetwork like structures or nanonecklaces. Further, they concluded that the morphology and the amount of particles depends on the “dielectricity and polarization energy of the fluid”. [141] However, in our 2018 study (Publication III), TiO₂ nanoparticles synthesized by PLA in scCO₂ did not consist of any particles of size few hundreds of nm. Our 2019 study (Publication IV) on synthesis on TiO₂ nanoparticles in gas, liquid, and supercritical CO₂ with variable fluid densities indicated absence of any significant effect of the fluid density on the morphology or size of nanoparticles. In addition, at all CO₂ densities studies in our study, only nanoparticles few tens of nm in diameter were observed. Furthermore, the earlier mentioned observation by Saitow et al. [62] and Machmudah et al. [129], of only two such discreet population sizes of nanoparticles varying by an order of magnitude, have not been reported for PLA in H₂O to the best of our knowledge. This raises questions whether the effect of fluid density is observable only for low reactivity metals. Do the laser and scanning parameters affect the PLA process such that they negate the effect of change in fluid density? Saitow et al. [141] performed PLA for 10 minutes with 20 Hz laser while Mardis et al. [78] performed PLA for 15 minutes with 10 Hz laser. There was no mention of a scanner with the laser in their studies. In our study, we irradiated the titanium target for 30 minutes with a 101 kHz laser and scanned it over an area of 7 × 7 mm at the speed of 2 m/s.

The ***third query*** is the presence of carbon nanoparticles or carbon layers independent from the carbon on the nanoparticles. This could mean presence of several mechanisms of carbon formation from CO₂ decomposition. Such observation has not been previously reported in PLA in pressurized CO₂.

3 NANOPARTICLE SYNTHESIS AND CHARACTERIZATION METHODS

In this chapter, we discuss about the materials used in this study and briefly explain how the nanoparticle samples were produced in each publication. Further, the characterization techniques used to analyze the samples are explained. Briefly summarizing this chapter, the material precursors needed were only titanium target, deionized water, and CO₂ gas. PLA was performed in deionized water and pressurized CO₂ including scCO₂ using two different setups to produce nanoparticles from titanium target in a single step process. In case of PLA in H₂O, nanoparticle suspensions were obtained upon ablation which were characterized as suspensions or as nanoparticle powder after drying. In case of PLA in pressurized CO₂, dry powder of nanoparticles was obtained upon ablation, which were characterized in the dry form. The analytical techniques used for characterizing the nanoparticle samples consisted of TEM (including HR-TEM and STEM, EDS), Raman spectroscopy, XPS, UV-Vis spectroscopy, XRD, SAXS and WAXS. In addition, particle size measurement was done manually from TEM images.

3.1 Precursors

Titanium (from Goodfellow Ltd), 99.99%, pure was used as the ablation target material and CO₂ (from Oy AGA Ab) >99.8% pure (with O₂ ≤ 20 ppm, H₂O ≤ 100 ppm) was used as the solvent for PLA in pressurized CO₂. For the nanoparticle synthesis experiments, the solvents used were only deionized water and CO₂.

3.2 Preparing nanoparticles by PLA in H₂O and pressurized CO₂

PLA in H₂O

For PLA in H₂O in **publications I and II**, the experimental setup included an 85W, 500 ns SPI pulsed laser with a wavelength 1062 nm and repetition rate 25 kHz, a PC-controlled GSI HB-X10 XY scanner connected with the laser, a titanium target (submerged in deionized H₂O) and a test vessel (as shown in schematic in **figure 4** and actual experiment picture in **figure 13**). The maximum energy of the laser beam was 3.4 mJ per pulse. The laser beam was focused on the target with an f-theta Ronar lens of focal length 160 mm. The set up was arranged so that the laser beam was scanned on the target from the top, perpendicular to the target surface at a speed of 2 m/s and over an area of 8 × 8 mm. The thickness of the water film above the target was 5 mm and the ablation time was 30 minutes for each experiment. In the publication I, three types of ablation experiments were performed with laser powers; (1) 20%, (2) 40%, and (3) 50% of the maximum laser power while in the publication II, seven types of experiments were performed at laser powers; (1) 12%, (2) 15%, (3) 18%, (4) 20%, (5) 30%, (6) 40%, and (7) 50% of the maximum laser power. After the ablation experiment finished, the nanoparticle suspensions were collected for their characterization.

For **publication III (PLA in H₂O part)**, the experimental setup was the same as explained above. However, the laser and its parameters used were different. A 70 W, 250 ns pulse fiber laser with wavelength of 1062 nm, and repetition rate of 101 kHz was used with a f-theta lens of focal length 80 mm. The scanned area was 6 × 6 mm and the ablation time was 30 minutes. The water film thickness above the target was 4 mm. The loss in laser transmission was measured to be same for 13 mm thick

sapphire window (PLA in scCO₂) and 4 mm thick water film above target (PLA in H₂O). After the experiment, the nanoparticles were collected in the form of nanoparticle suspension. This test was conducted to compare directly the effect of solvent (H₂O vs. CO₂) on the nanoparticle phase, dispersibility, size and morphology.

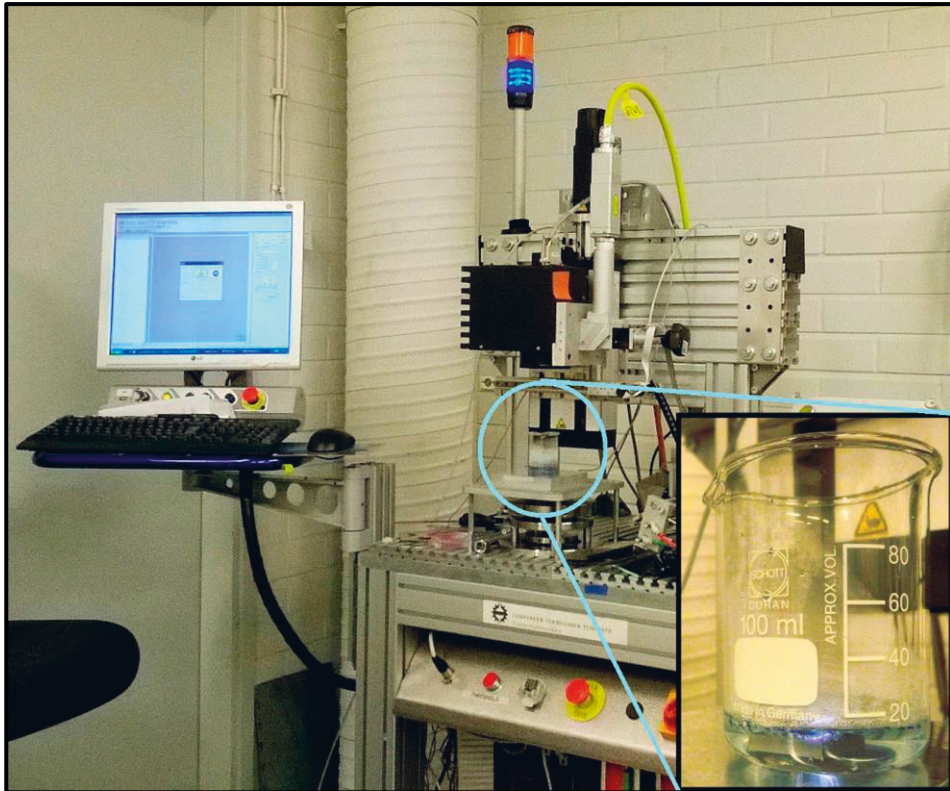


Figure 13. Picture of the experimental set-up with PLA in deionized H₂O in process with the visible plasma in inset in bottom right corner.

PLA in liquid, gaseous and supercritical CO₂

For **publication III (PLA in scCO₂ part)** and **IV**, the experiment consisted of a 70 W, 250 ns pulse fiber laser with wavelength of 1062 nm, and repetition rate of 101 kHz (schematic in **figure 14**). A telecentric f-Theta lens with focal length 80 mm and spot diameter of 35 μm, was used to focus laser on the titanium target. The laser beam energy was 690 μJ per pulse for 101 kHz repetition rate.

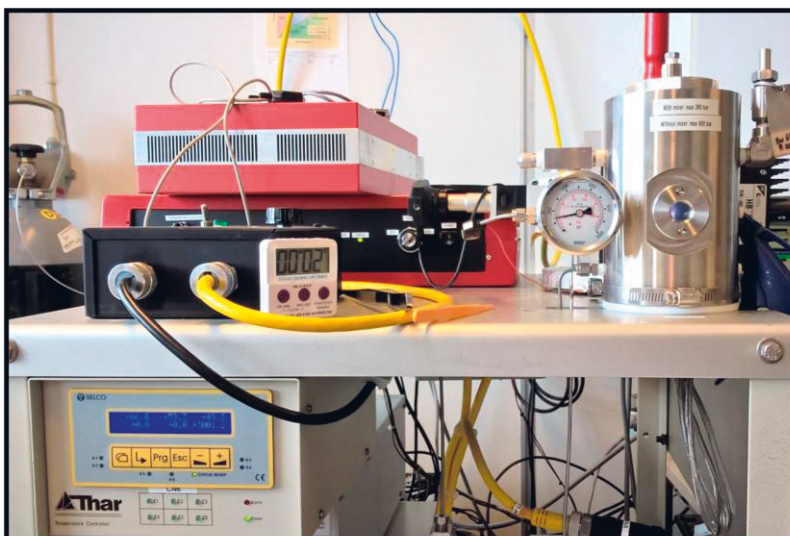


Figure 14. Picture of experimental set-up in PLA in scCO₂ during an ongoing high-pressure nanoparticle synthesis experiment.

In publication III, the laser scanner was fixed on a stand attached with micrometer for better accuracy during focusing of laser. The ablation target was placed on the target stand which was then inserted inside the chamber. The stand also ensured correct height of the target inside the chamber, in front of the sapphire view ports. The target was placed inside the chamber for a 30-minute ablation period where the laser irradiated the target surface perpendicularly. The equipment for this experiment was a Thar Technologies Inc. RESS 250 system (Pittsburg, USA) with laser and scanner attached to it. The CO₂ system consisted of a 316SS steel reaction chamber, built for pressures up to 62 MPa and temperatures up to 150 °C. For heating the chamber, there were heating rods built into the walls. The chamber consisted of two viewports made of sapphire windows, which was used to introduce the laser for causing ablation on the target fixed inside the chamber. The set up did not have a cooling system for the chamber. Before beginning the laser irradiation for ablation, the reaction chamber was flushed with CO₂ (gas) several times to alleviate the effects of atmospheric O₂ and N₂. CO₂ was pumped into the chamber at 20 grams/minute using a high-pressure piston-pump until the pressure stabilized at 10 MPa and temperature stabilized at 50 °C. This was followed by 30 minutes of laser ablation on an area of 6 × 6 mm and at a scanning rate of 2 m/s. The depressurization of the chamber was done meticulously by an automatic back-pressure regulator (ABPR)

after ablation finished at a rate of 5 s/MPa. The samples were collected in the form of dry nanoparticle powder from the chamber.

In publication IV, the experimental set-up was the same as in publication III. In this case, the ablation experiments were performed at five different CO₂ pressures - 5, 10, 15, 20 and 40 MPa while the CO₂ temperatures was fixed at 50 °C and at three different CO₂ temperatures namely 30 °C, 40 °C and 50 °C while the CO₂ pressure was fixed at 10 MPa. So, there were seven tests out of which five were in supercritical CO₂, one in liquid CO₂ and one in gaseous CO₂. In these tests, CO₂ was heated through the heating rods in the chamber wall. The ablation duration was 30 minutes and the scanned area was 7 × 7 mm at 2 m/s.

The main process parameters of the study from PLA in H₂O and pressurized CO₂ are mentioned in **Table 1 and 2**, respectively.

Table 1. Process parameters for PLA in H₂O

Parameters for PLA in H ₂ O (Publications P1, P2 and P3)	Range
Pulse length	500 ns (P1, P2), 250 ns (P3)
Repetition rate	25 kHz (P1, P2), 101 kHz (P3)
Focusing lens	160 mm (P1, P2), 80 mm (P3)
Lasers	SPI 85W (P1, P2), 70W (P3)
Beam energy	3.4 mJ (P1, P2), 690 μJ (P3)
Wavelength of Laser	1062±2 nm
Solvent	Deionized H ₂ O
State of solvent	Liquid
Solvent temperature	20 °C (NTP)
Solvent pressure	0.101 MPa (NTP)
Total laser irradiation time	30 minutes

Table 2. Process parameters for PLA in gaseous, liquid and supercritical CO₂.

Parameters for PLA in liquid, gaseous and scCO ₂ (Publications P3 and P4)	Range
Pulse length	250 ns
Repetition rate	101 kHz
Focusing lens	80 mm
Laser	70W

Beam energy	690 μ J
Wavelength of Laser	1062 \pm 2 nm
Solvent	CO ₂
State of solvent	Supercritical, liquid, and gaseous
Solvent temperature	30–50 °C
Solvent pressure	5–40 MPa
Total laser irradiation time	30 minutes

3.3 Analytical techniques

Transmission electron microscopy

Transmission electron microscopy (TEM) in scanning mode and high-resolution mode was performed to study the size, morphology, and crystallinity of the nanoparticles. Electron diffraction (ED) pattern was taken from samples to observe the crystallinity of the nanoparticles while EDS was employed for their elemental analysis. The publications I and II include the use of TEM at Tampere University Hervanta campus (formerly Tampere University of Technology). A Jeol JEM-2010 microscope at 200 kV acceleration voltage was used for imaging the nanoparticles. For this, the TEM samples were prepared by dropping nanoparticle suspensions on TEM copper grids with a holey carbon film. To ensure as less agglomeration of nanoparticles as possible, freshly ablated suspensions were used to make TEM samples. Electron diffraction patterns were also obtained from the same samples. For publication III, imaging was done using a TEM (Jeol, JEM-2200FS HRTEM) for high resolution imaging of nanoparticles at Aalto University, while a Jeol JEM-2010 microscope at Tampere University was used to characterize the shape and size of nanoparticles. For publication IV, Tampere Microscopy Center's Jeol JEM F200 (S)TEM with a Jeol Dual electron energy dispersive spectrometer (EDS) was used for imaging the nanoparticle powders. For analyzing the variation in the elemental composition of the nanoparticles, STEM-EDS was used in line analysis and spot analysis mode. For (S)TEM, the samples were prepared by touching the TEM copper grid containing holey carbon film with the nanoparticle powder.

X-ray diffraction, small-angle and wide-angle X-ray scattering

For determining the phases present in the nanoparticle powders and suspensions, X-ray diffraction (XRD) and wide-angle X-ray scattering (WAXS) measurements respectively, were done while small-angle X-ray scattering (SAXS) was employed to measure particle size and size distribution. X-ray measurements were done using a Panalytical Empyrean Multipurpose Diffractometer with a CuK α X-ray source at wavelength of 0.1541 nm. were obtained. A solid-state pixel detector, PIXcel3D, connected with the diffuser measured the scattered intensities. The phase identification of the XRD peaks was performed with Panalytical HighScore Plus software (version 3.0.5) from the database PDF-4+ of the International Centre for Diffraction data (Database version 4.1065).

For (XRD) measurements, the scan range was 20.00°–80.95° with 0.05° step size. For SAXS measurements, the scan range was from –0.12° to 5.01° with 0.01° step size. For this, measurement setup utilized a parallel beam X-ray mirror for Cu radiation. The X-ray generator was powered at 40 mA and 45 kV. The nanoparticle suspensions were directly used as liquid for SAXS measurement while for XRD measurements, the nanoparticle suspensions were dried (drying temperature was 40 °C) to obtain nanoparticle powder in case of PLA in H₂O. For preparing SAXS samples, identical volume of each suspension was enclosed between two (X-ray transparent) Mylar foils which was then put in the respective circular transmission holders. The background sample was prepared by enclosing deionized water between two Mylar foils. WAXS measurement was done with the SAXS samples, however the scan range was from 5.0° to 54.9° with a 0.026° step size.

Raman spectroscopy:

Raman spectroscopy is a useful tool for to get detailed information on the nanoparticles phase, chemical structure, crystallinity and polymorphy. For publication III and IV, Raman spectroscopy was done to get additional information about the phases present in the nanoparticle powders, in addition to XRD. The nanoparticle samples were analyzed with the Renishaw InVia Qontor Raman microscope using a 532 nm laser. The laser power was 0.175 μ W.

X-ray photoelectron spectroscopy

X-ray photoelectron spectroscopy (XPS), is a brilliant technique for analyzing chemistry of nanomaterials, since the depth of measurement is quite shallow, less than about 5 nm. This is helpful for analyzing thin layers on nanoparticles. For publication IV, the XPS analysis was performed at Top Analytics, Turku, with a PHI

Quantum 2000 spectrometer with an Al 1486.6 eV mono x-ray source at 24.3 W. The nanoparticle powder was carefully spread on top of a double-sided tape that was attached to a metal plate to prepare the XPS sample. A stationary beam with a beam diameter of 100 μm measured the nanoparticle samples.

Ultraviolet–Visible Spectroscopy

For publication IV, a spectrophotometer (Shimadzu UV 3600) in reflectance mode at VTT, Tampere, was used to study the optical properties of the synthesized nanoparticles at 10 MPa scCO_2 pressure and 50 $^\circ\text{C}$ scCO_2 temperature. In the wavelength range 300–900 nm, the absorbance spectra were measured. The band-gap energy of the nanomaterial sample was estimated from the Tauc-plots.

Particle size measurement

For publication I, the nanoparticle sizes were measured by SAXS and compared with the nanoparticle size measurements from TEM image analysis done manually. With SAXS measurement, we obtained the particle size and the size distribution of particles by volume. Panalytical's EasySAXS software (version 2.0a) was used to analyze SAXS data and obtain the volume-weighted particle size distribution, $D_v(R)$, by indirect Fourier transform method. The second method for determining the nanoparticle size and size distribution was based on manually calculating the diameters of 100 nanoparticles from the TEM images. The data was then presented in the form of a histogram to analyze the size distribution (by number). The size distribution curve obtained from SAXS measurement was plotted with the histogram from TEM image analysis to compare the results from these two measuring techniques. It is worth noting that while the TEM samples were prepared from freshly ablated suspensions, the SAXS samples were prepared and measured several hours after ablation. Additionally, peak analysis was performed on the XRD pattern by using Panalytical HighScore Plus software (version 3.0.5) to determine the crystallite size. The Panalytical software, based on the Scherrer equation, used line profile analysis algorithm for determining the crystallite size. For publication IV, the average nanoparticle sizes for each sample were obtained by measuring diameters of 400 nanoparticles from the TEM images using Image J software (Version 1.50i).

4 PLA IN H₂O - (*Synthesis of stable phase rutile-TiO₂ nanoparticles and their size reduction and narrowing of size distribution measurement*)

In this chapter, size reduction and narrowing of size distribution of TiO₂ nanoparticles with laser power is demonstrated by synthesizing TiO₂ nanoparticles using PLA of titanium in deionized H₂O at different laser powers. XRD, WAXS, and Raman spectra all indicated presence of mostly stable phase rutile-TiO₂ as well as small amounts of anatase-TiO₂ and brookite-TiO₂ in the nanoparticles. In addition, SAXS is proposed as a promising method for determination of particle size and size distribution from nanoparticle suspensions by comparing it against more commonly used TEM image analysis. Finally, we compared the TEM, Raman and XRD analysis results from TiO₂ nanoparticle suspensions made by two different lasers - 250 ns at 101 kHz and 500 ns at 25 kHz. TEM samples from the nanoparticle suspensions prepared at different laser powers showed very similar networks of round nanoparticles connected with randomly shaped nanomaterials. Irrespective of laser power used, Raman and XRD data suggested presence of mostly rutile in nanoparticles along with small amounts of anatase or brookite or a combination of both. The results in this chapter are based on publications PI, PII, and PIII.

4.1 TEM analysis of nanoparticles

Section 4.1 contains results from publication PI.

The nanoparticles were almost all round based on TEM images of nanoparticle samples synthesized at 20 % laser power (LP), 40 % LP, and 50 % LP, **figures 15 (a), (b), and (c)** respectively. To decrease the interfacial energy, the nanoparticles assume a spherical shape. Hot clusters of atoms coalesce with other hot clusters consisting of high mobility surface atoms and form polycrystalline nanoparticles [35,58]. Based on TEM micrographs, the suspensions synthesized at 20%, 40%, and 50% LP, all consisted of nanoparticles that were smaller than 10 nm, however there were also some large nanoparticles, over 50 nm. The already synthesized

nanoparticles can absorb the subsequent laser pulses and undergo modifications that reduce the particle size and narrow the size distribution [113,142–144] or undergo melting and fusion like process to grow into large nanoparticles [145].

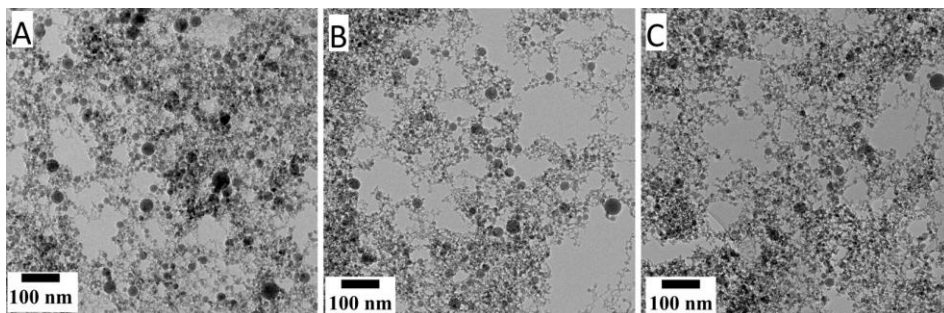


Figure 15. TEM micrographs of nanoparticles from suspensions synthesized by PLAL of Ti in H₂O at laser powers (a) 20%, (b) 40%, and (c) 50%, of the maximum laser power. The scale in the micrographs is 100 nm. [Publication PI].

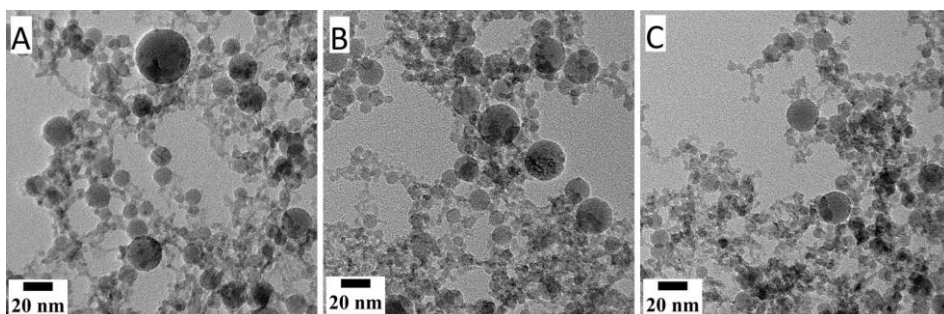


Figure 16. TEM micrographs showing nanoparticles forming web-like networks for suspensions synthesized by PLAL of Ti in H₂O at laser powers (a) 20%, (b) 40%, and (c) 50%, of the maximum laser power. The scale in the micrographs is 20 nm. [Publication PI].

In **figures 16 (a), (b), and (c)**, spherical shaped nanoparticles were observed to connect to each other in the form of web-like networks. The presence of web-like networks in PLAL produced nanoparticles has previously been reported by Ledoux et al. [146]. The nanoparticles were crystalline based on the presence of bright spots in their electron diffraction (ED) pattern (**figure 21 (a)**). However, the presence of diffused rings indicated some amorphous nanomaterial also. The nanostructures connecting round nanoparticles were randomly shaped and likely amorphous. The decrease in nanoparticle size was slightly observable from **figures 16 (a) to (c)**, which is later clear in **figure 19 (d)**. Moreover, there were reduced number of larger

nanoparticles at higher laser powers. Although, this might not be representative of the whole sample, since it is one image from TEM grid, however, such observations were confirmed from the SAXS measured particle size distributions, which typically measures millions of particles.

4.2 Phase analysis of nanoparticles by XRD, WAXS and Raman spectroscopy

Section 4.2 contains results from publications PI, PII, and PIII.

Titanium is chemically active and readily reacts with the available oxygen to form its oxides during PLAL in deionized water. Oxygen is available both as dissolved in deionized water [71] and ionized oxygen produced as a result of plasma induced breakdown of water [147]. The nanoparticles dried from suspensions or directly as suspension were analyzed for their phase composition by XRD, WAXS and Raman spectroscopy.

Based on the XRD spectra of dried nanoparticles from suspension (**figure 17**), the nanoparticles were crystalline, and their small size caused peak broadening. The high peaks in the XRD spectra corresponded to mostly rutile-TiO₂. Rutile peaks at 27.4, 36.1, 41.2, 54.3, 64.0, and 69.7° (2θ degrees) were observed. The peak at 56.6° was observed as a shoulder to the more intense rutile peak at 54.3°. The peaks observed at 25.3, and 48.0° corresponded to anatase-TiO₂. Further, the double peak between 68 and 70, corresponds to anatase at 68.8 and rutile at 69.7°. The highest intensity peaks of brookite-TiO₂ at 25.3 and 25.7° were not visible distinctly due to strong anatase signal at 25.3. Besides, the anatase peak is broadened due to small size of nanoparticles, making it more challenging to observe brookite peaks in the same region. However, one of the high intensity peaks of brookite at 30.8° was observed, indicating presence of small amounts of brookite in the nanoparticles.

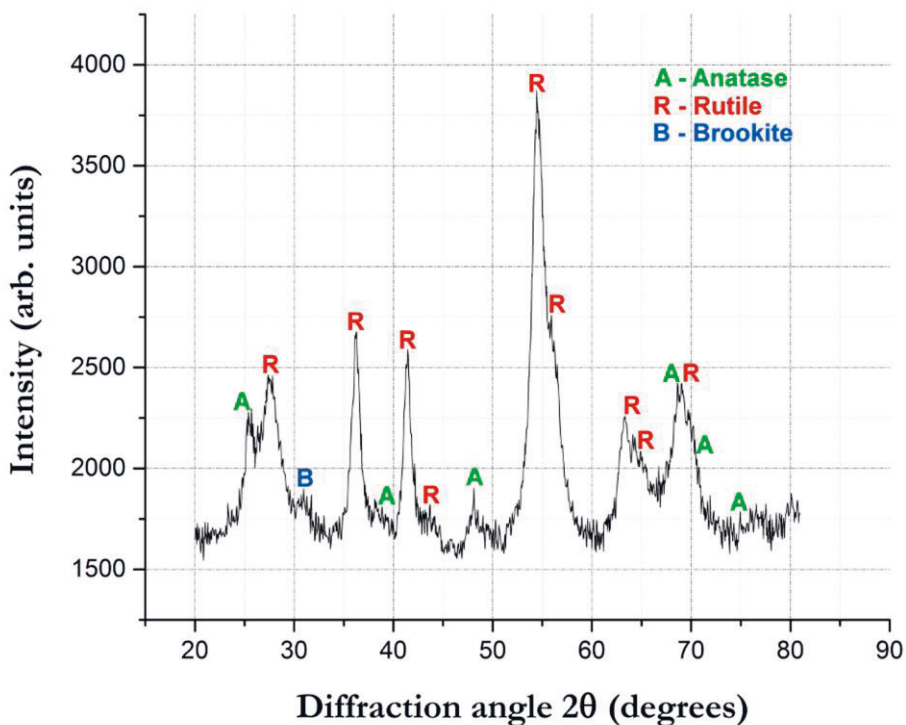


Figure 17. XRD spectra of nanoparticles synthesized by PLAL of titanium in H₂O indicating mostly rutile and some anatase and brookite phases of TiO₂. [Publication PI].

The WAXS measurement can be done directly from nanoparticle suspension in the same measurement as SAXS, so it is advantageous as a quick phase analysis technique. The WAXS measurements from the nanoparticle suspensions (**figure 18**) corroborated XRD results to indicate mostly rutile-TiO₂, based on the peaks at 27.4 and 36.1 (2θ) degrees. The minor phase was anatase-TiO₂. Additionally, the small size of the nanoparticles caused broadening of the peaks, similar to the observation in the XRD spectra. From all suspensions synthesized at different laser powers, the XRD and WAXS spectra were almost alike with same ratio of TiO₂ phases. This suggested that the laser power did not affect the phase composition of nanoparticles.

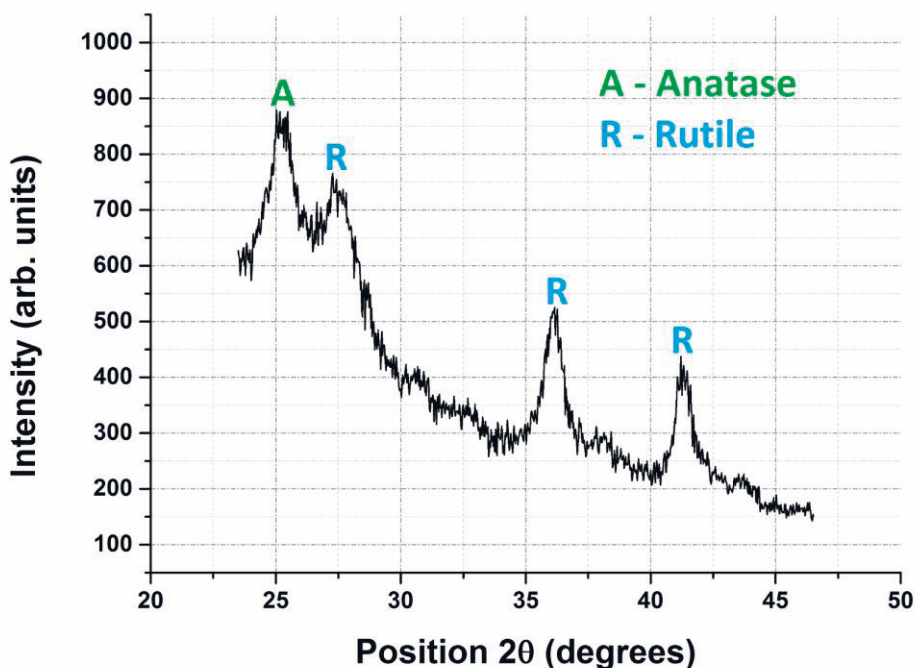


Figure 18. WAXS spectra of nanoparticles synthesized by PLAL of titanium in H₂O indicating mostly rutile and some anatase, both allotropes of TiO₂. [Publication PII].

The Raman spectra (**figure 22 (b)**) indicated mostly rutile-TiO₂ with possibility of presence of some anatase and brookite as minor phase, in agreement with the results from WAXS and XRD data. The strong peaks at 440 cm⁻¹ and 610 cm⁻¹ corresponded to rutile. The high broad peak at around 150 cm⁻¹ indicated presence of anatase or brookite or both in nanoparticles. Additionally, there were small peaks of anatase and brookite marked in **figure 22 (b)**, suggesting again that both phases were likely present as a minor phase.

4.3 Particle size and size distribution measurements (TEM and SAXS)

In this section, the size distribution measurement results by TEM and SAXS are compared (**figures 19 (a)–(c)**) from publication PI. For this, the histogram from TEM image analysis was plotted with y-axis corresponding to the number of nanoparticles and x-axis corresponding to nanoparticle diameter. This plot also included $D_v(R)$ from SAXS on the right y-axis, which was plotted against the same

x-axis. Both the TEM determined histogram and SAXS determined size distribution curve for nanoparticles synthesized at 20% laser power (**figure 19 (a)**) showed a maximum between 8–10 nm. Further, in the plot corresponding to suspension synthesized at 40% laser power (**figure 19 (b)**), both techniques suggested minima at around 19 nm followed by a small increment around 22–24 nm. Both the histogram and distribution curve indicated the bimodality of the nanoparticle size distribution. This was indicated also for suspensions synthesized at 50% laser power (**figure 19 (c)**). In this case, both measurements suggested a maximum at around 6 nm.

Two particle size populations give rise to a bimodal size distribution. Based on atomistic modelling and stroboscopic videography experiments by the research groups of Zhigilei and Barcikowski, respectively, they proposed two main mechanisms in the PLAL process that leads to bimodal size distribution of nanoparticles: the first mechanism is the “Rayleigh-Taylor instability” at the plume-supercritical water² interface giving rise to large nanoparticles, while the second mechanism is the “nucleation and growth of small nanoparticles in the metal-water mixing region” [110,111]. Meunier and Meneghetti have previously reported bimodal size distribution for PLAL produced nanoparticles [35,60].

From these particle size distribution plots in **figures 19 (a)–(c)**, size reduction and narrowing of size distributions was also observed with increasing laser power. The absolute values of average nanoparticle sizes for all laser powers were slightly higher for SAXS measurement than TEM measurement. This is due to two main reasons: (i) SAXS gives a volume size distribution while TEM measurement was number size distribution, and (ii) SAXS measurement is not sensitive to agglomerates resulting in measurement of ‘agglomerate size’ as ‘particle size’ while in TEM, due to good resolution and contrast, it is easy to distinguish between individual particles and agglomerates. The size reduction and narrowing of size distribution occurs due to photothermal melting-evaporation and explosive disintegration of bigger nanoparticles to form smaller nanoparticles [145,148]. The size reduction mechanism may change if the laser pulse duration is changed to picoseconds or femtoseconds. A thermodynamic model was proposed by Werner et al. to interpret the change in nanoparticle size reduction mechanisms with the change in laser parameters [148].

² Supercritical water – Thin layer of water close to plasma plume and cavitation bubble turns to supercritical state due to high local temperature and high local pressure conditions. For water, $T_c = 374$ °C, and $P_c = 22.1$ MPa.

The average nanoparticle size at each laser power by TEM and SAXS was plotted against the laser power to observe this pattern. **Figure 19 (d)** indicated a decreasing trend of nanoparticle size with increasing laser power, and a good agreement between the size reduction trends by both measurement techniques. Good agreement between both measurement technique was observed based on the bimodality indicated by both, and the similarity of size reduction trend. This demonstrates SAXS as a fast, promising method for particle size distribution analysis. Revisiting the research questions from section 1.4, this answers the first research question for measuring size and size distribution of PLAL produced nanoparticles.

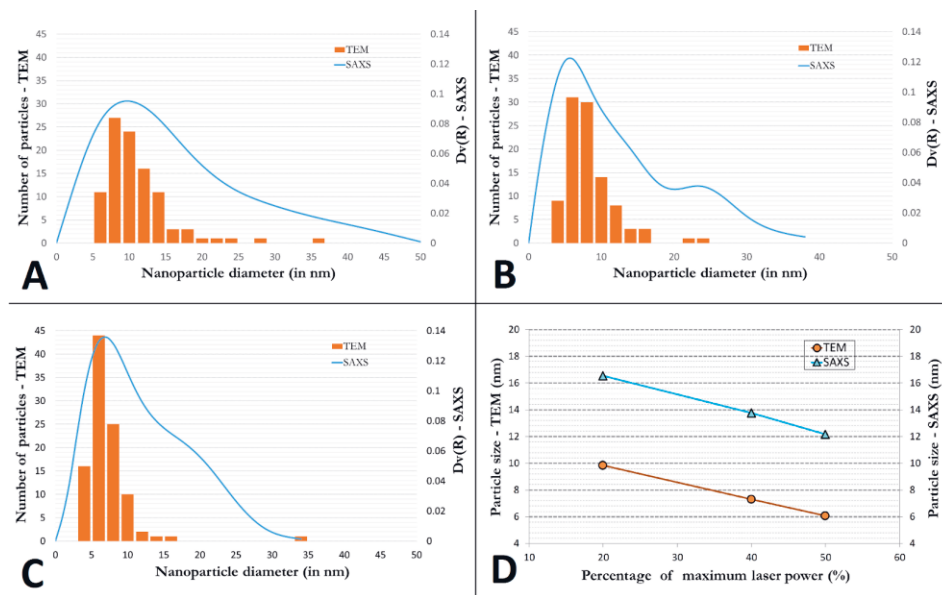


Figure 19. Particle size distributions of nanoparticle suspensions synthesized at laser powers (a) 20%, (b) 40%, and (c) 50% of the maximum laser power, with the blue line representing SAXS measured size distribution curve superimposed on the orange size distribution histogram obtained from TEM-image analysis, (d) The decreasing average nanoparticle size with increasing laser power measured by TEM and SAXS showed same trend, indicating good agreement between both measurement techniques. [Publication P1].

SAXS measurement technique is based on a parametric distribution model, in which the assumed particle shape stays same (such as spherical in this case) while the particle size varies [149]. The measurement in SAXS technique can quickly be done from freshly ablated nanoparticle suspensions while TEM measurement is tedious and involves several steps such as TEM sample preparation, drying of TEM grid,

TEM imaging, manual TEM image analysis, and finally plotting of data. The number of nanoparticles analyzed by SAXS is several tens of magnitudes higher than in TEM. However, SAXS technique is sensitive to the particle concentration in the nanoparticle suspension. According to the guidelines of EasySAXS software from Panalytical, for the results to be reliable, the absorption factor of the sample should be between 1.5 and 5. This is because a value lower than 1.5 indicates no conclusive difference between particles and the background. Finally, for the determination of particle size and size distribution directly from suspensions in a quick and easy way, we propose SAXS as a promising method. However, TEM is still proposed as a necessary method for determining nanoparticle shape and appearance.

4.4 Comparison of nanoparticle morphology and phase synthesized with different laser parameters

The aim of this section is to compare the results from PLA of titanium in deionized water with two different lasers and show the similarity of phase analysis results. This is important because we observe multiphase non-stoichiometric oxides by PLA of titanium in scCO₂ (discussed in Chapter-5), and the idea here is to assert that the formation of such mixed phase oxides is not due to a different laser. It is in fact due to a different solvent, which is, supercritical CO₂. The results presented in section 4.4 correspond to publications PI, PII, and PIII.

Synthesis of nanoparticles by PLA of titanium in deionized H₂O using – 250 ns laser at 101 kHz, 690 μJ/pulse (PIII) VS. 500 ns laser at 25 kHz, 3.4 mJ/pulse (PI, and PII)

The repetition rates of 25 kHz and 101 kHz mean that the delay between the two laser pulses was 40 μs and 9.9 μs, respectively. Such time delay is much shorter than the cavitation bubble lifetime which is usually few hundreds of microseconds in normal atmosphere water. This would result in strong screening of the laser pulses with the cavitation bubble, which acts like a lens and may defocus the beam to cause irregular ablation [124]. Similar optical shielding can be expected from the plasma plume [35]. Due to a high repetition rate and comparatively slow scanning rate, re-ablation of the same spot may happen also. The pulse durations of 250 ns and 500 ns are rather close, so that the particle formation mechanisms stay the same. The pulse energies are, however, a bit different; 690 μJ for 250 ns laser while 3.4 mJ for 500 ns laser. With the 250 ns laser, an 80 mm focusing lens ensured a spot diameter

of around 35 μm at all laser powers whereas in 500 ns laser, a 160 mm focusing lens focused the laser to spot diameters 55–155 μm depending on the laser power used.

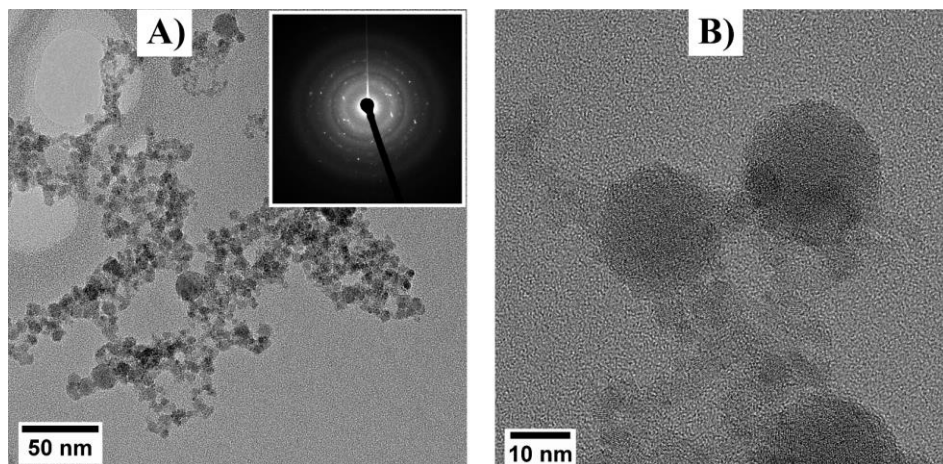


Figure 20. TEM micrographs for suspensions synthesized by 250 ns, 101 kHz laser showing (a) nanoparticles forming network like structure and ED pattern (inset) indicated crystallinity of nanoparticles and presence of some amorphous nanomaterials, and (b) at higher magnification, round nanoparticles seem joined to random shaped nanostructures. [Publication PIII].

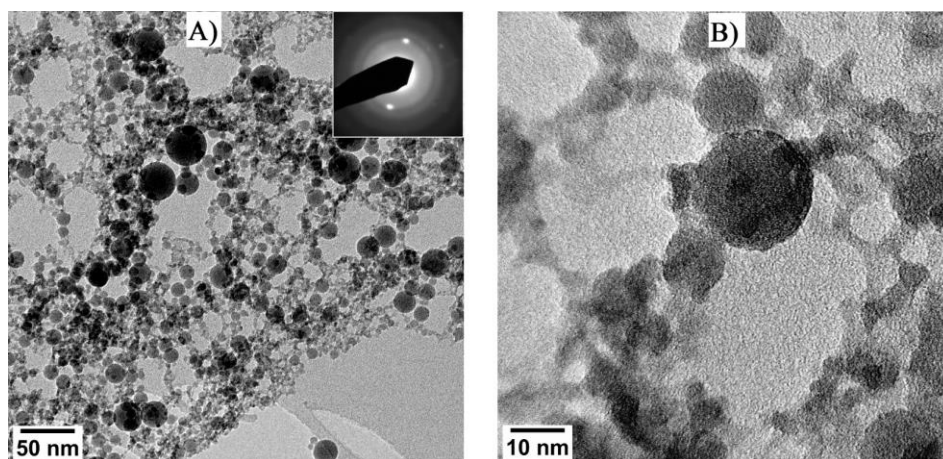


Figure 21. TEM micrographs for suspensions synthesized by 500 ns laser at 25 kHz showing, (a) round nanoparticles agglomerated and connected to each other with smaller nanoparticles, and were mostly crystalline with some amorphous phase, as indicated by ED pattern in inset, or (b) random shaped nanomaterials connect the round nanoparticles. These micrographs showed similarities to nanoparticles synthesized by 250 ns laser at 101 kHz depicted in figure 20. [Publication PI].

For nanoparticle synthesis by PLAL, the laser fluence is of great importance. For 250 ns laser, the maximum laser fluence was 71.75 J/cm² while for the 500 ns laser, it was 57.63 J/cm². So, no dramatic difference between the laser fluence of the two lasers.

From the comparison of laser parameters, similar phenomenon could be expected in PLA with both lasers: re-ablation of nanoparticles and same spot on target surface, laser defocusing by the cavitation bubbles, and mostly thermal mechanisms (for nanosecond lasers) for nanoparticle formation and their size reduction. Further, the results from both lasers are compared based on TEM, Raman, and XRD data.

The TEM micrographs from suspensions made by 250 ns laser at 101 kHz (**figures 20 (a) and (b)**), and 500 ns laser at 25 kHz (**figures 21 (a) and (b)**) showed very similar results and indicated presence of nanoparticles that connected with each other to form networks.. In each case, and ED pattern (**inset figures 20 (a) and 21 (a)**) crystalline nanoparticles along with some randomly shaped nanostructures that were amorphous. A detailed discussion on this topic has already been presented in section 4.1 TEM micrographs in **figures 20 and 21** suggested no difference in synthesized nanoparticles with the change in the laser parameters.

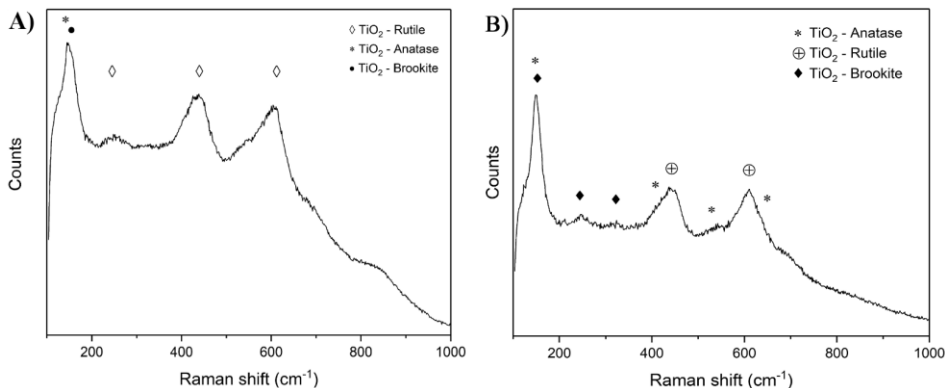


Figure 22. Raman spectra of nanoparticles synthesized by PLAL of titanium in H₂O using a (a) 250 ns laser at 101 kHz and (b) 500 ns laser at 25 kHz. [Publication PIII and PI, respectively].

Raman spectra in **figures 22 (a) and (b)** indicated similarity in phase composition of nanoparticles synthesized by different laser parameters. to each other in terms of the observed major peaks to indicate mostly rutile-TiO₂ as the main phase based on

the strong peaks at 440 cm^{-1} and 610 cm^{-1} . The high peak at 150 cm^{-1} could be from anatase or brookite or a combination of the two in both figures. The other smaller peaks of rutile, anatase and brookite have been marked in the figures.

XRD spectra (figures 23 (a) and (b)), in accordance with the Raman spectra indicated that nanoparticles composition was almost the same despite change in laser and its parameters. The main peaks in the XRD spectra corresponded to rutile peaks at 27.4 , 36.1 , 41.2 , 54.3 , 64.0 , and 69.7° , and brookite peak at 25.3° which also corresponded to anatase. Anatase peak at 25.305° and brookite peak at 25.340° were hard to distinguish due to peak broadening and overlap. The overlap might have made the intensity stronger for this peak, since the other high intensity peaks were too small to analyze with high certainty.

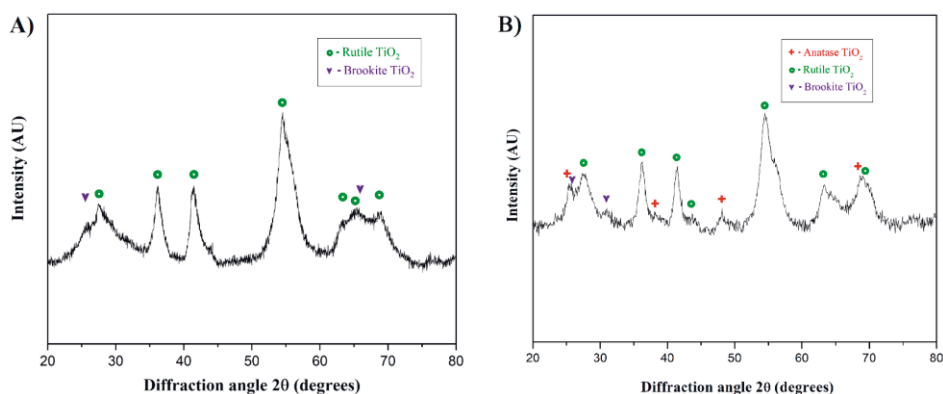


Figure 23. XRD spectra of nanoparticles synthesized by PLAL of titanium in H_2O by (a) 250 ns laser at 101 kHz and (b) by 500 ns laser at 25 kHz. [Publication PIII and PI, respectively].

In the next chapter, the results from PLA of titanium in sCO_2 as well as liquid and gaseous CO_2 using 250 ns laser at 101 kHz, $690\text{ }\mu\text{J/pulse}$ are reported and discussed.

5 PLA IN PRESSURIZED CO₂ - (*Synthesis of Stable, Meta-Stable Anatase-TiO₂, Ti_xO_y Nanoparticles With Or Without Carbon Shell/Layer*)

In this chapter, we report the results from the first tests for synthesis of nanoparticles in scCO₂. This is then compared with PLA in H₂O results using the same laser parameters. Initial results indicate formation of well-dispersed, non-agglomerated nanoparticles by PLA in scCO₂. The nanoparticles were composed of mostly meta-stable phases anatase-TiO₂ and Ti₂O₃, while non-stoichiometric phases, such as TiO_{0.89} was also present. This is discussed in juxtaposition with the results from PLA in H₂O where we observed mostly rutile-TiO₂ nanoparticles that were partially agglomerated or connected to each other with randomly shaped nanomaterials to form web-like networks.

After this, the results from a series of seven different tests are reported with varying CO₂ pressures 5–40 MPa and CO₂ temperatures 30–50 °C. We report on formation of mostly anatase-TiO₂ nanoparticles with core-shell structures and nanoparticles with either thick carbon layer or without carbon layer on them. This is followed by characterization with Raman, XRD and XPS. Further, the effects of CO₂ temperature and pressure on the nanoparticle size, and phase composition are analyzed. This is followed by a thorough discussion for the formation of core-shell nanoparticles and on the possible mechanisms of formation of different nanoparticle phase compositions, including the effect of pressurized CO₂ on them. The results presented and discussed in this chapter correspond to publications PIII and PIV.

5.1 Synthesis of nanoparticles by PLA in scCO₂ vs H₂O – A Comparative analysis

Section 5.1 contains results from publication PIII. The plasma dynamics and cavitation bubble phenomenon are influenced by the solvent pressure during PLA in pressurized media [131,132,135]. PLA in supercritical fluids has advantages over PLA in liquids due to higher reaction rates in supercritical fluids owing to their higher

diffusivity and further having zero surface tension. Supercritical fluids penetrate the nanostructures easily and escape from it unharmed. [129] Achieving supercritical condition is relatively easier and takes less energy for CO₂ ($T_c = 31.1\text{ }^\circ\text{C}$ and $P_c = 7.4\text{ MPa}$) compared to H₂O ($T_c = 374\text{ }^\circ\text{C}$ and $P_c = 22.1\text{ MPa}$) while there is advantage of almost negligible distortion of beam shape, which is observed in scH₂O [128]. In our study, the nanoparticles were synthesized by PLA of titanium in scCO₂ and H₂O with a 250 ns 1064 nm laser at 101 kHz. The synthesized nanoparticles were studied with TEM, Raman and XRD to compare their size, morphology, dispersibility and phase composition.

5.1.1 TEM analysis of nanoparticles

From the TEM micrographs (**figures 24 (a) and (b)**), we observed uniformly dispersed round nanoparticles from the sample synthesized by PLA in scCO₂ at 10 MPa, 50 °C. The roundness of the nanoparticles is due to the diffusion of hot surface atoms as well as to reduce the interfacial energy upon melting caused by laser processing of already produced nanoparticles [26]. The crystalline rings in the ED pattern (**figure 24a inset**) indicated presence of mostly crystalline nanoparticles. Saitow et al reported formation of gold nanospheres by PLA in scCO₂ with particle diameters around 400 nm, however, we did not observe any such large nanospheres in this study [62]. This could either be due to a much smaller CO₂ density around 0.34–0.38 g/cm³ in comparison to 1.7 g/cm³ used by Saitow et al. A direct comparison with the study of Saitow et al. would be unfair due to very different laser parameters used. This study used a high repetition rate of 101 kHz and a longer pulse duration 250 ns compared to 20 Hz and 9 ns in the study of Saitow et al. [62]. Additionally, in this study the laser beam was scanned on the target surface at 2 m/s for 30 minutes while in the study of Saitow et al., there was no mention of scanning parameters. It has been reported that for PLA in supercritical fluids such as CO₂ and CHF₃ (trifluoromethane), that lower densities of supercritical fluids result in smaller nanoparticles (few nm to few tens of nm) while higher densities result in formation of bigger nanospheres (few hundreds of nm) and nanonecklaces [62,141].

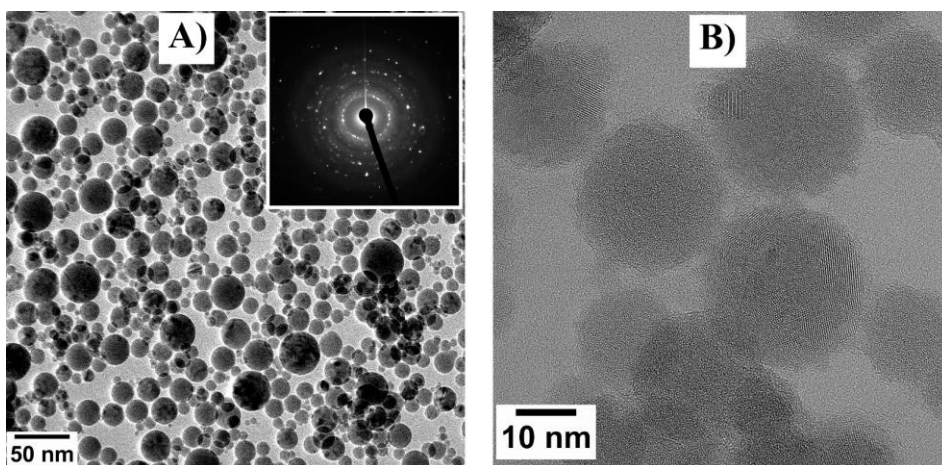


Figure 24. TEM images of nanoparticles synthesized by PLA in $scCO_2$ showing (a) well dispersed round nanoparticles that were crystalline based on ED pattern (inset), and (b) lattice fringes observable in high resolution TEM image of nanoparticles. [Publication PIII].

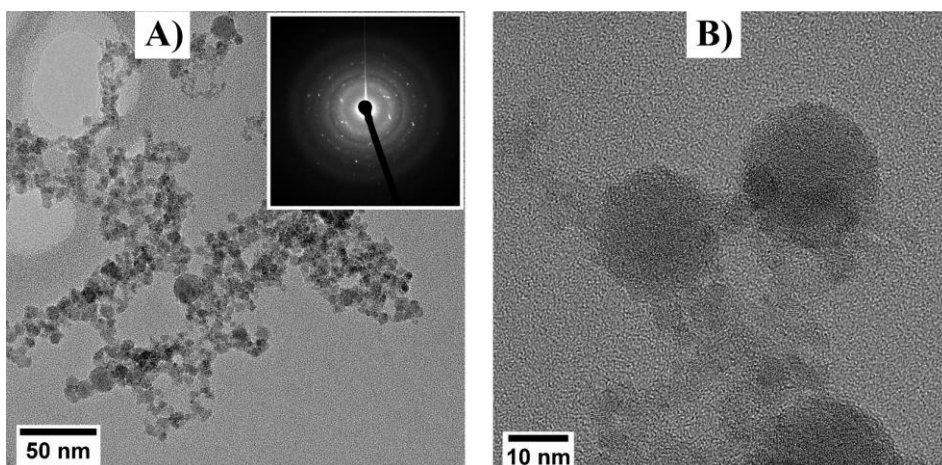


Figure 25. TEM images of nanoparticles synthesized by PLA in H_2O showing (a) nanoparticles joined to each other forming networks consisting of both crystalline and amorphous nanomaterials based on ED pattern in inset, and (b) round nanoparticles joined to smaller nanoparticles and connected by random shaped nanomaterials. [Publication PIII].

In comparison, the TEM micrographs of nanoparticles synthesized by PLA in H_2O (**figures 25(a) and 25(b)**) showed web-like networks of round nanoparticles. Such web-like networks have been previously reported [146]. At higher magnifications (figure 25(b)), it was possible to observe that these web-like networks consisted of randomly shaped nanoparticles connected to each other as well as other

nanoparticles to cause some degree of agglomeration. The crystalline rings and spots and maybe also diffuse rings in the ED pattern from this region (**inset figure 25(a)**) indicated presence of crystalline as well as some possibly amorphous phases in the nanomaterials.

A comparative analysis of PLA in scCO_2 and H_2O based on TEM analysis showed that the nanoparticles formed in scCO_2 were uniformly dispersed and non-agglomerated. This could be because scCO_2 is non-polar and has zero surface tension while the synthesized nanoparticles were polar. The electrical double layer that usually surrounds the nanoparticle surface in aqueous medium should be absent for scCO_2 , in theory. Further, due to no evolution of hydrogen during PLA in scCO_2 , hydrogen bonding of the particles can be eliminated as well as the presence of aqueous ions such as OH^- , H_3O^+ , and H^+ ions is unlikely. These factors combined would ensure no agglomeration. Although, after the PLA in scCO_2 process is finished, it may be expected that some H_2O in the form of moisture gets adsorbed on the particle surface when the high-pressure chamber is opened, and the nanoparticles are exposed to the ambient environment. Another noticeable difference was that the randomly shaped nanoparticles observed for PLA in H_2O (**Fig. 25(a) and 25(b)**), were absent in PLA in scCO_2 . The above comparison suggests PLA in scCO_2 as a promising process for single step synthesis of dry, spherical-shaped nanoparticles that are well-dispersed and non-agglomerated.

5.1.2 Phase analysis – Raman and XRD

The nanoparticles synthesized by PLA in scCO_2 and H_2O were analyzed with Raman and XRD. Raman spectra of the nanoparticles synthesized by PLA in scCO_2 (**figure 26(a)**) indicated the nanoparticle powder consisted of mostly anatase- TiO_2 with small amount of titanium (III) oxide (Ti_2O_3). This was evident from the sharp distinct peaks of anatase while the broader features could be from the smaller peaks of anatase, titanium (III) oxide or some other titanium oxides. The presence of titanium carbide could be ruled out due to absence of any peaks at 222, 420 or 605 cm^{-1} . In contrast, the Raman spectra of nanoparticle synthesized in H_2O (**figure 26(b)**) showed two big peaks of rutile- TiO_2 at 440 and 610 cm^{-1} . Other identified phases were anatase- TiO_2 , brookite- TiO_2 , or combination of both based on the peak at 150 cm^{-1} . Further, the broad features up to 900 cm^{-1} could indicate presence of amorphous material or disordered phase.

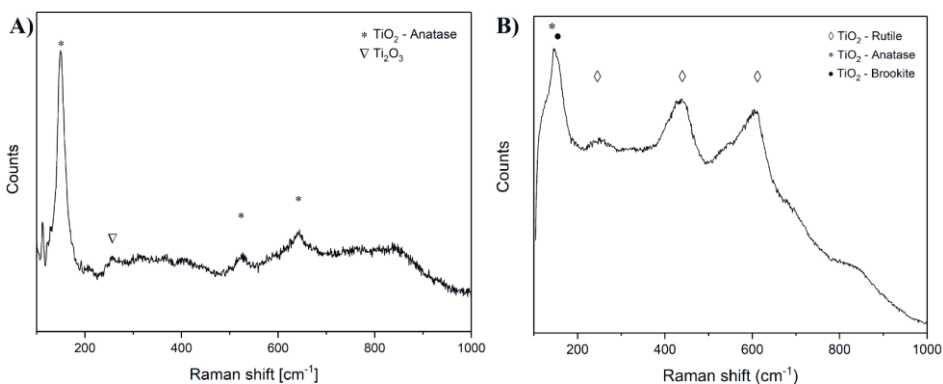


Figure 26. Raman spectra of nanoparticles synthesized by (a) PLA in $scCO_2$, and (b) PLA in H_2O . [Publication PIII].

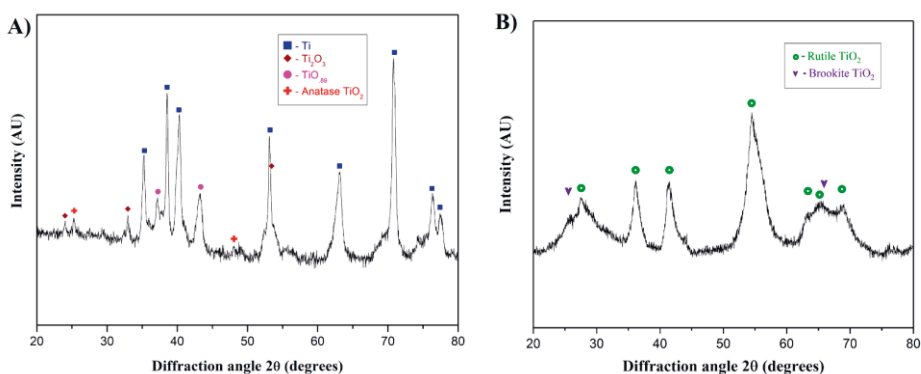


Figure 27. XRD spectra of nanoparticles synthesized by (a) PLA in $scCO_2$, and (b) PLA in H_2O . [Publication PIII].

The XRD results corroborated the observations from Raman analysis. Peak broadening was observed in the XRD spectra and is commonly known to be caused by the small size of nanoparticles. XRD spectra of nanoparticles produced in $scCO_2$ (**figure 27(a)**) indicated presence of anatase- TiO_2 and titanium (III) oxide Ti_2O_3 . Further, the presence of $TiO_{0.89}$, a non-stoichiometric high-temperature phase, was also indicated. Additional information on this phase is presented in appendix 1. In the XRD pattern of the nanoparticles produced in H_2O (**figure 27(b)**), the sharp peaks at 27.4 , 36.0 , 41.2 , and 54.3° strongly indicated presence of rutile- TiO_2 . Other rutile peaks have been marked in **figure 27(b)**. Additionally, the small peaks at 25.3 , 62.0 and 70.0° may correspond to brookite, rutile or a combination of both. The sharp and large peaks of titanium in **figure 27 (a)** were observed because the

nanoparticles sample was on top of the titanium substrate. The same sample was used for Raman analysis in **figure 26 (a)**, but no titanium peaks were observed since metals are transparent in the Raman spectra.

From the Raman and XRD analysis of nanoparticles, the formation of meta-stable (anatase-TiO₂ and Ti₂O₃) and non-stoichiometric (TiO_{0.89}) phases was observed, in contrast to PLA in H₂O, where stable phase rutile-TiO₂ was observed to be the main phase of the nanoparticles.

5.1.3 Source of oxidation

Supercritical CO₂ is a non-toxic fluid with low reactivity; however, during the PLA process, it can decompose to produce O⁻¹/O₂. The ionized target species from the high-temperature high-pressure plasma plume will then interact with the solvent ions after the plasma plume implodes and ionized species are introduced to the cavitation bubble, containing solvent ions to produce nanoparticles [7,58,150]. The dissociation of CO₂ can either follow the minimum path energy to form CO and O⁻¹ which would then again form CO₂ and O₂ or in extreme conditions of temperature, dissociation of CO₂ can form molecular carbon and oxygen, which is possible via dissociative electron attachment [151] or vacuum-ultraviolet³ photodissociation [152]. These solvent species can then oxidize the solute ions such as the titanium ions in this study. In PLA in H₂O, the ionized target species react with oxygen [150] that is either made available by the plasma-induced water splitting of oxygen bound to water molecule [147] or readily available oxygen dissolved in water [71]. H₂O is less oxidizing than CO₂ under 1000 K according to Ellingham diagram [153]. However, fully oxidized stable phase rutile-TiO₂ was identified as the main phase of nanoparticles synthesized by PLA in H₂O. This is likely if the oxygen dissolved in water is responsible for oxidation. An exhaustive thermodynamic analysis would be out of scope of this study.

In summary, section 5.1 answers the second research question from section 1.4. This is further answered and discussed in section 5.3 to explore formation of multiphase titanium oxides and the possible pathways for reduction and oxidation reactions between titanium and CO₂.

³ vacuum ultraviolet – The part of the electromagnetic spectrum in which the photons are energetic enough to excite atom from its ground state to ionization, can be referred to as vacuum ultraviolet. Its wavelength is around 200 nm.

After the comparative analysis in this section, the TEM analysis of nanoparticles synthesized in scCO₂ was continued and particles with some layer or shells corresponding to carbon were observed. Could this mean decomposition of CO₂ to form carbon and oxygen? Such decomposition is possible under extreme conditions as discussed earlier in this section. This led to a new series of experiments where the CO₂ pressure and temperature were varied and the effect of this variation was measured against the particle size, morphology, shell thickness, and phase composition. The results from these measurements are reported and discussed in section 5.2.

5.2 Synthesis of nanoparticles in gaseous, liquid and supercritical CO₂

The results presented and discussed in section 5.2 correspond to publication PIV.

5.2.1 TEM analysis of nanoparticles synthesized at 10 MPa, 50 °C

Based on investigation with transmission electron microscopy, the nanoparticles were classified into three categories, (i) nanoparticles with core-shell structure (**figure 28 (a)–(c)**), (ii) nanoparticles with thick carbon layer (**figure 28 (d) and (e)**), and (iii) nanoparticles with no carbon layer (**figures 24 (a) and (b)**). The particles with no carbon layer have already been discussed earlier in section 5.1.1 for nanoparticles synthesized by PLA in scCO₂.

STEM images (**figures 28 (a) – (c)**) show round nanoparticles that formed core-shell structures with a smooth shell of varying thickness. This type of core-shell structures and varying shell thickness have been previously reported in literature, where they found the shell thickness to increase with the increase in the particle diameter [154]. Individual particles were covered with carbon layer. This was further elucidated from the backscattered electron (BSE) image in topographical mode **figure 28 (c)**. Such core-shell nanoparticles were the dominant type of nanoparticles synthesized. This is consistent with earlier studies of PLA of iron-gold in which the core-shell morphology corresponded to over 90% of the nanoparticles [155].

STEM image (**figure 28 (d)**) showed the other type of nanoparticles that consisted of a thicker carbon layer which surrounded many nanoparticles. This observation was further evident in the STEM-BSE image (topographical mode) in

figure 28 (e) in which the clusters of nanoparticles appeared to be under thick carbon layer. These particles were not the characteristic core-shell structures and were fewer than the core-shell morphology particles. While the nanoparticles from other test conditions also consisted of nanoparticles with thin and thick carbon layer, no prominent trend in the variation of the shell thickness was observed.

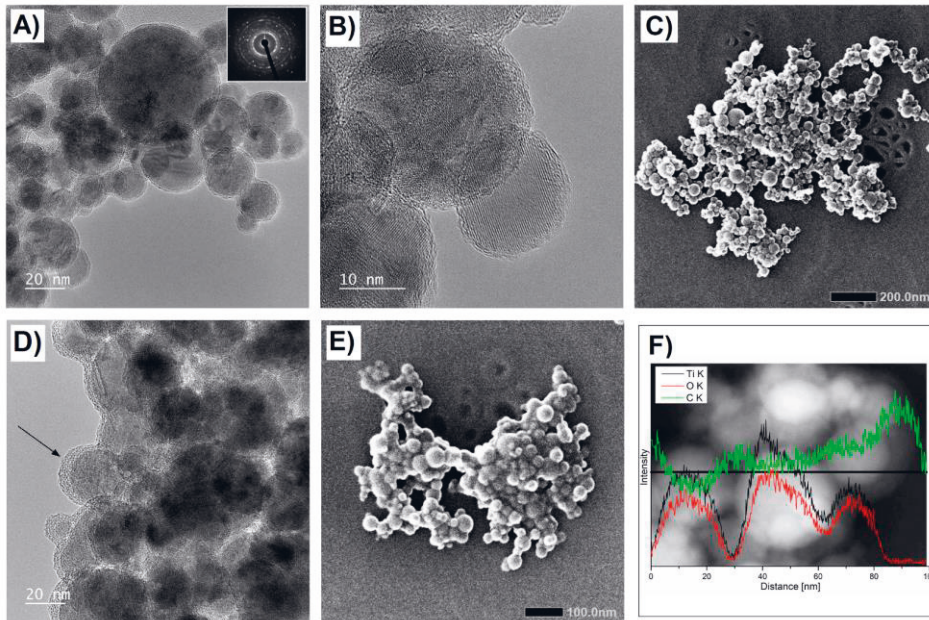


Figure 28. Particles with thin carbon layer: (a) TEM image of core–shell type nanoparticles and its electron diffraction pattern (inset), (b) high-resolution TEM image of particle with its core showing lattice fringes conforming to anatase (101) single crystal, (c) STEM BSE image of core–shell particles. Particles with thick carbon layer: (d) TEM image of thick carbon layer on particles, marked by an arrow, (e) Thick carbon layer on nanoparticles observable in STEM BSE image (topographical mode), and (f) STEM-EDS line analysis showing intensity variation of Ti, O and C in the particles. [Publication PIV].

Based on STEM-EDS line and spot analysis (**figure 28 (f)**), the core region of the nanoparticles was rich in titanium and oxygen while the shell or layer region was carbon rich. A dramatic change in peak intensities, visible for titanium and oxygen 80–100 nm, was not observable for carbon intensity since carbon covers the nanoparticle from all sides. This means that there will always be some carbon detected even when analyzing the composition at the center of the core of the nanoparticle.

The STEM images from samples synthesized at other CO₂ pressures and temperatures showed very similar results as in figure 28. The nanoparticle population types and ratios were the same and no trend in carbon layer thickness with change in CO₂ pressure and temperature was observed.

5.2.2 Phase analysis and band gap of nanoparticles

Raman and XRD analysis

The most prominent peaks in the Raman spectra of the nanoparticles (**figure 29 (a)**) at 144, 400, 520, and 636 cm⁻¹ corresponded to anatase-TiO₂. The peaks for rutile-TiO₂ at 447 cm⁻¹ and 610 cm⁻¹ were observed as shoulders or small features to the anatase peaks. In the wide spectrum measurement (**inset figure 29 (a)**), two broad features centered around 1100 cm⁻¹ and 1450 cm⁻¹ were observed. Since D and G bands were absent, the carbon on nanoparticle surface could be in the form of hydrocarbon rather than pure carbon. C–C bond stretch and CH₂ twists and bends explain the peaks at 1000 cm⁻¹ and 1450 cm⁻¹, respectively. Thus, Raman measurements indicated anatase-TiO₂ to be the main phase of the nanoparticles with rutile-TiO₂ as a minor phase. Additionally, the wide spectrum Raman measurement indicated presence of carbon on particle surface which could be in the form of hydrocarbon.

XRD spectra of the nanoparticles **figure 29 (b)** strongly indicated presence of anatase-TiO₂, in agreement with the Raman results. The most prominent peaks of anatase-TiO₂ were observed at 25.3°, 48.1°, and 55.2°, while other peaks are marked in figure 29 (b). Other smaller peaks corresponded to rutile-TiO₂ at 27.4°, brookite-TiO₂ at 30.8°, and carbon containing phase – titanium oxycarbide Ti₍₁₎O_(0.5)C_(0.5) at 36.2° and 42.1°. Additional information on titanium oxycarbide is presented in appendix 2. Although carbon peaks were not observed at 26.1 and 42.3 since carbon may not be present in crystalline form, the broad feature 25–31° may possibly indicate presence of amorphous carbon. Marzun et al. reported the difficulty of observation of carbon peaks in XRD of core-shell particles with carbon layer synthesized by PLAL, since XRD is more applicable for crystalline materials [71].

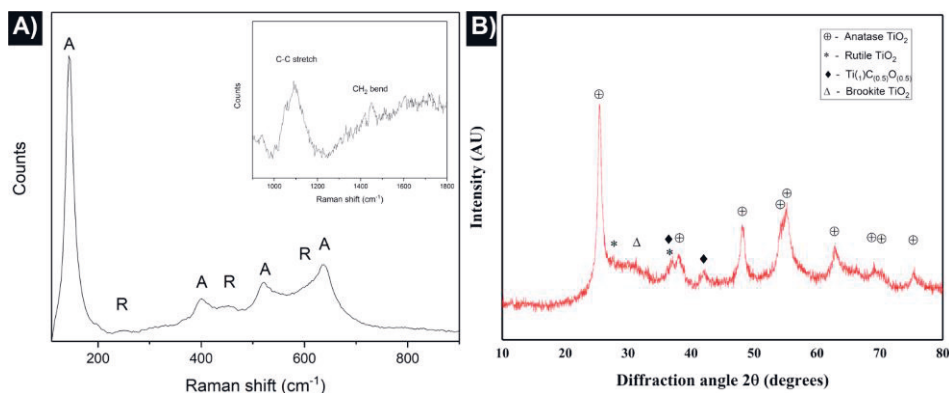


Figure 29. (a) Raman spectra, and (b) XRD spectra, of the nanoparticles synthesized by PLA in scCO₂. [Publication PIV].

Raman and XRD results indicated nanoparticles consisted of mostly anatase-TiO₂. While rutile-TiO₂ was present as a minor phase, XRD results suggested possibility of also brookite-TiO₂. Further, both Raman and XRD indicated presence of carbon in some form such as hydrocarbon in Raman and titanium oxycarbide in XRD. For a conclusive measurement on presence of carbon on nanoparticles and the phases present, XPS measurements were done.

XPS analysis

The XPS spectra (**figure 30 (a)**) confirmed the presence of titanium, oxygen, and carbon in the nanoparticles with the observation of peaks corresponding to Ti2p, O1s and C1s. The presence of carbon in sp² hybridization C=C was indicated from the 284–286 eV C1s peak (**figure 30 (b)**). Additionally, carbon in sp³ hybridization is likely present based on the broadening of C1s peak. The small broad feature 288–290 eV may indicate presence of O–C=O bonds. The absence of peaks at 281.5, 454.7, and 460.9 eV eliminates possibility of titanium carbide. In **figure 30 (c)**, the peak at 530 eV corresponded to O1s peak while the shoulder to this peak around 531.5–532 eV may signify presence of oxygen bonded to carbon C=O. This may indicate presence of organic carbonyl, or ketones or then presence of H–O–C bond. It is also possible that metal carbonate (TiCO₃ 531.5–532 eV) in nanoparticles adds to this feature. The peaks in XPS spectra in **figure 30 (d)** at 464.3 and 458.5 eV corresponded to Ti2p₁ and Ti2p₃ respectively. This strongly indicates presence of Ti+4 in the form of rutile-TiO₂ and anatase-TiO₂ based on their bond energies. In summary, XPS results indicated nanoparticles consisted of mostly anatase and rutile

in agreement with the results from Raman and XRD and further suggested presence of carbon on the nanoparticles. Additionally, a minor amount carbon could be bonded to oxygen but not to titanium.

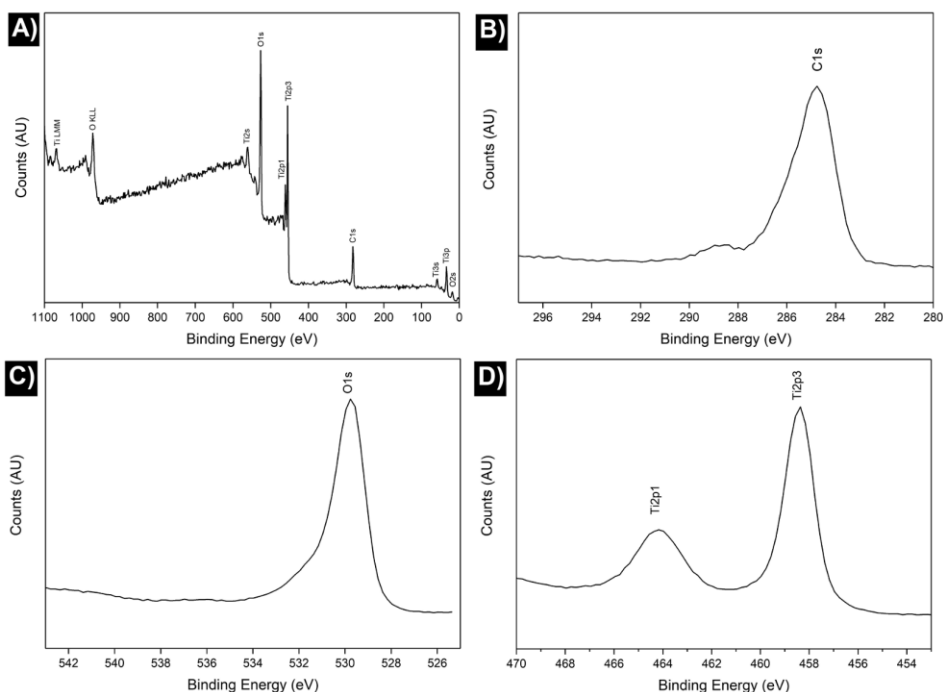


Figure 30. XPS spectra of nanoparticles synthesized by PLA in $scCO_2$, corresponding to the (a) Survey spectra, (b) C1s peak, (c) O1s peak, and (d) Ti2p1 and Ti2p3 peaks. [Publication PIV].

Based on the Tauc-plot in **figure 31**, the band gap of the nanoparticles was calculated to be 3.32 eV. This is slightly higher than the more commonly known bulk value of 3.20 eV for anatase- TiO_2 [156]. The slightly higher band gap is reportedly due to quantum size effect and surface states in case of nanoparticles and thin films [157,158]. This suggests that the nanoparticles were mostly anatase- TiO_2 , corroborating the Raman and XRD results.

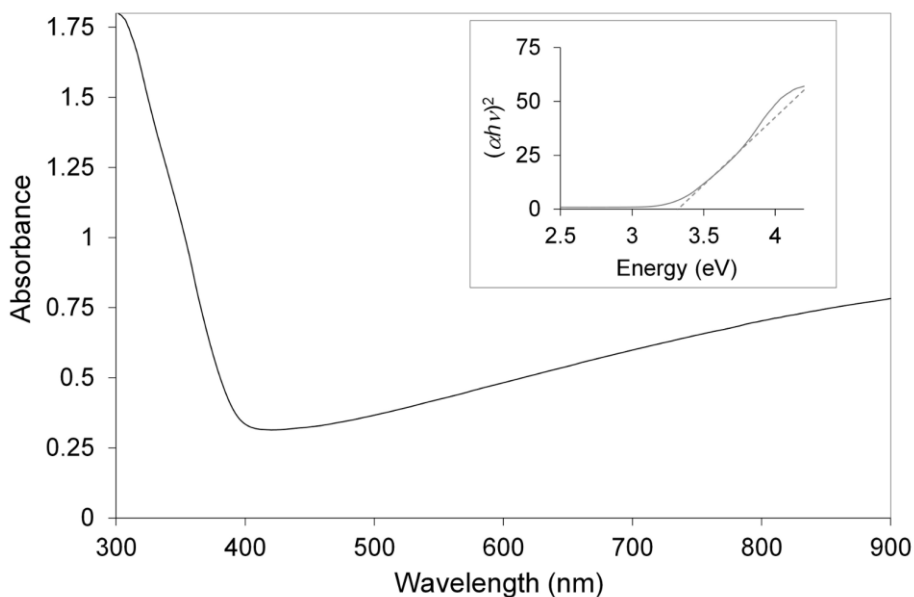


Figure 31. Absorption spectra 300–900 nm and band gap (inset) of nanoparticles synthesized by PLA in scCO₂ at 10 MPa, 50 °C. [Publication PIV].

5.2.3 Analysis of experimental parameters – Effect of CO₂ pressure and temperature

In this section, the effects of CO₂ temperature and pressure on the nanoparticle size, and phase composition are presented and discussed. To observe temperature effect, the CO₂ temperature was varied from 30 to 50 °C while pressure was fixed at 10 MPa. Similarly, to observe pressure effect, the CO₂ pressure was varied from 5 MPa to 40 MPa while the temperature was kept constant at 50 °C.

Effect of CO₂ temperature

Temperature effect on nanoparticle size

Conclusive results on the effect of CO₂ pressure on the cavitation bubble dynamics are well reported [128,131], however, the impact of CO₂ temperature is not studied as much. The nanoparticle size plot against the CO₂ temperature (**figures 32**) indicated size refinement. The size refinement with increasing temperature is rather startling since higher temperatures cause decrease in CO₂ density under isobaric

conditions, while increasing CO₂ pressure under isothermal condition causes increase in CO₂ density as well as particle size refinement. For PLA in liquids, in situ SAXS technique has been used to thoroughly study the effects of cavitation bubble dynamics to nanoparticle formation [159,160]. Similar comprehensive studies for PLA in supercritical fluids would be interesting to understand the underlying phenomenon.

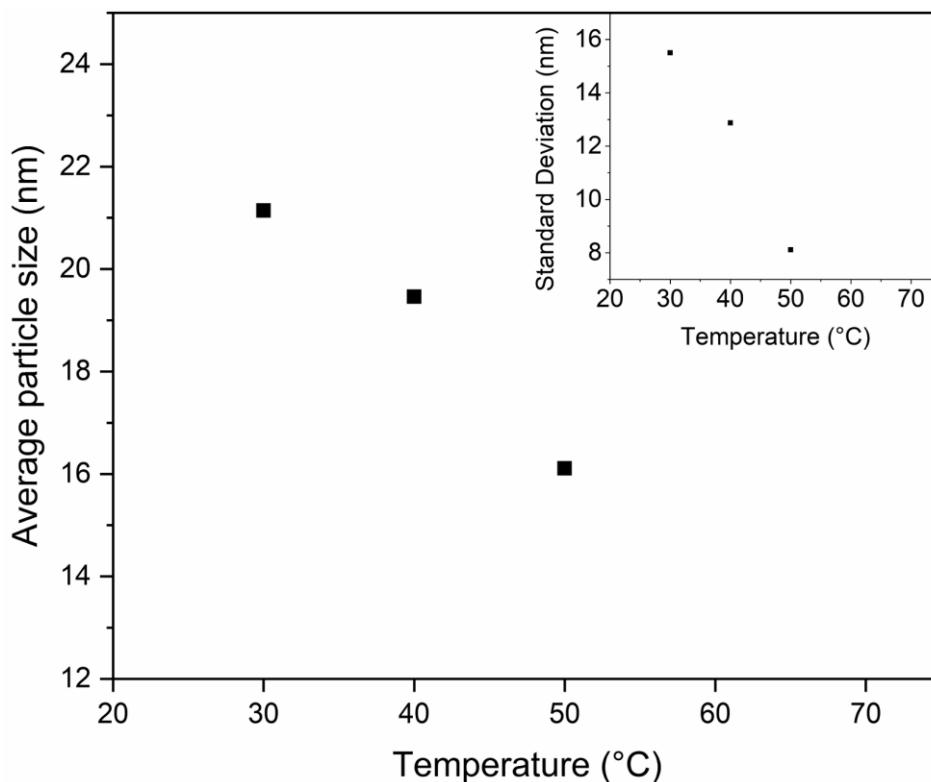


Figure 32. Variation in nanoparticle size with CO₂ temperature 30-50 °C, obtained from TEM. [Publication PIV].

Temperature effect on nanoparticle phase

The Raman spectra (**figure 33 (a)**) indicated anatase-TiO₂ to be the main phase and rutile-TiO₂ as the minor phase of nanoparticles despite the change in CO₂ temperature. The same trend was observed in the XRD spectra (**figure 33 (b)**) of nanoparticles, in agreement with the Raman results. In contrast to the CO₂ pressure

studies, discussed in the next sub-section, a definite trend in rutile amount with CO₂ temperature variation was not observed.

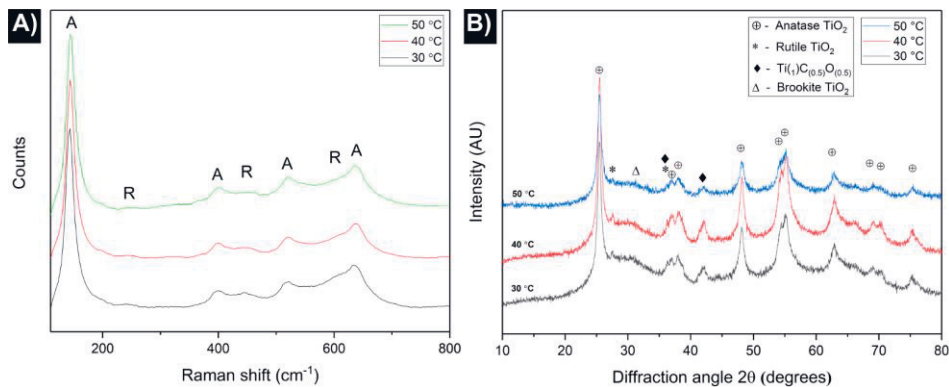


Figure 33. (a) Raman spectra, and (b) XRD spectra for nanoparticles synthesized by PLA in CO₂ at temperatures 30, 40, and 50 °C at 10 MPa. [Publication PIV].

Effect of CO₂ Pressure

Pressure effect on nanoparticle size

The plot of average particle size against CO₂ pressure in **figure 34** indicated particle size refinement with the increase in pressure. Such size refinement is in accordance with the particle size refinement reported by PLA in pressurized fluids (CO₂, and H₂O) for Au [140], Sn [161], and ZnO [162]. Higher solvent pressure decreases the cavitation bubble volume and lifetime which in turn leads to size refinement [131,162].

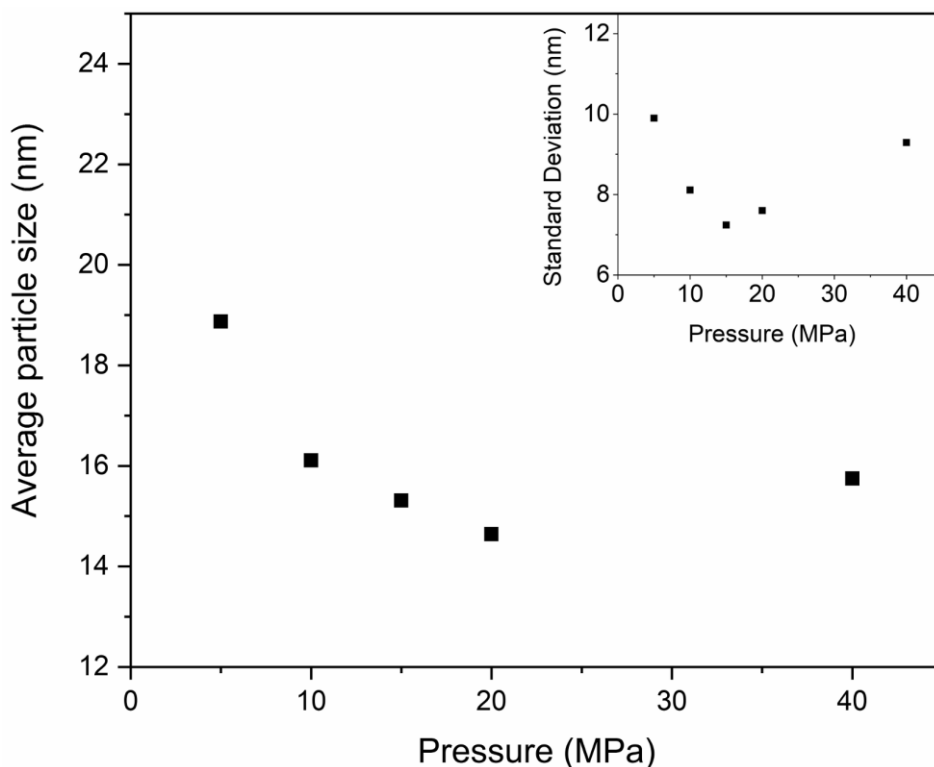


Figure 34. Variation in nanoparticle size with CO₂ pressure 5-40 MPa, obtained from TEM. [Publication PIV].

Raman and XRD spectra (**figures 35 (a) and (b)**) indicated anatase-TiO₂ to be the main phase of nanoparticles despite the change in pressure. However, there were some differences in the peaks corresponding to rutile-TiO₂ with the change in pressure for both Raman and XRD spectra. The plot for area of rutile to anatase fitted peaks with CO₂ pressure (**figures 36 (a) and (b)**) based on Raman and XRD spectra indicated increase in rutile amount with increased CO₂ pressure. The trend in the plot for area of the fitted peaks from XRD spectra verified the observation from Raman spectra. In addition, other noticeable difference in phase composition was the observation of Ti₃O₅, a high-temperature meta-stable phase, at 21.2° in the XRD spectra of nanoparticles synthesized at 15 MPa. Additional information for Ti₃O₅ is presented in appendix 3.

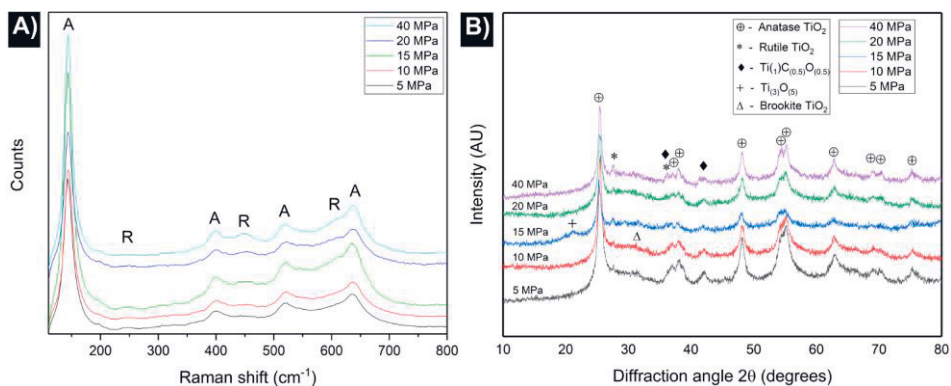


Figure 35. (a) Raman spectra, and (b) XRD spectra, for nanoparticles synthesized by PLA in CO₂ at pressures 5, 10, 15, 20, and 40 MPa at 50 °C. [Publication PIV].

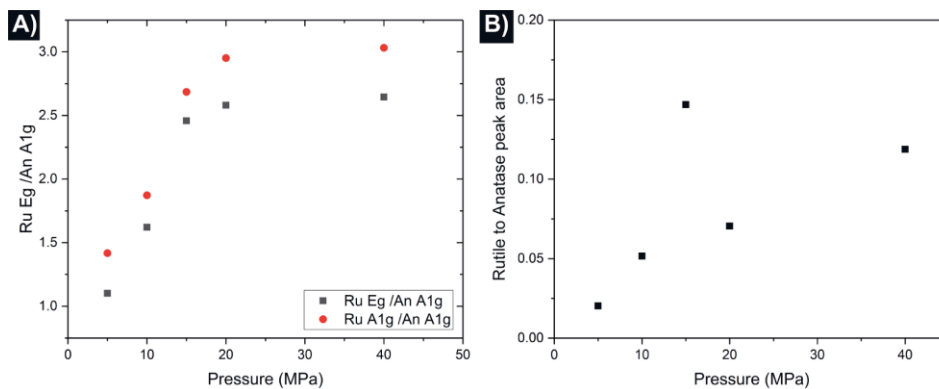


Figure 36. Rutile to anatase peak area ratios from (a) Raman spectra, and (b) XRD spectra, The blue squares in figure 36 (a) correspond to the area ratio of rutile Eg peak (440 cm⁻¹) to the anatase A1g peak (520 cm⁻¹). Similarly, the red circles correspond to the area ratio of rutile A1g peak (610 cm⁻¹) to the Anatase A1g peak. [Publication PIV].

As summary of section 5.2.3, size refinement was observed when CO₂ temperature was increased from 30 °C to 50 °C. Raman and XRD spectra indicated anatase-TiO₂ as main phase and rutile-TiO₂ as minor phase despite the temperature variation. Using CO₂ pressure from 5 to 40 MPa at 50 °C as a tool to control nanoparticle size and phase composition was more suitable in PLA process than CO₂ temperature. Increasing the CO₂ pressure from 5 to 40 MPa caused the size refinement of nanoparticles from 19 nm average particle diameter to about 14.5 nm. The reason was that higher CO₂ pressure caused a decrease in cavitation bubble volume and shortened its lifetime. Further, Raman and XRD suggested anatase-TiO₂ as main phase and rutile-TiO₂ as minor phase despite variation in CO₂ pressure. However,

the rutile amount seemed to increase with the increase in CO₂ pressure based on area of fitted peaks from Raman and XRD spectra.

In addition, section 5.2 answers the third research question (from section 1.4) to imply indirectly from Raman, XPS, and HR-TEM data that carbon was indeed found on nanoparticles and it is most likely produced by decomposition of CO₂ by laser, or hot nanoparticles, or catalysis by oxygen vacancies in anatase-TiO₂. However, whether this carbon is fully amorphous or consists of also multi-layer graphene or some other carbon nanostructure, is not fully established yet due to limitations of characterization techniques. In section 5.3.2, the possibilities of formation of carbon are discussed, in addition to multiphase oxides of titanium.

5.3 Discussion on materials science of nanoparticle synthesis by PLA at high-pressure

5.3.1 Origin of difference in nanoparticle phase and effects of solvent pressure in PLA

The phase and structure of the nanoparticles depend on mainly four factors: pressure, temperature, concentration of ablated material and concentration of solvent species. However, owing to “hemispherical symmetry of laser ablation”, these four parameters are neither constant in time or nor uniform in space. [58] High ambient solvent pressure affects the plasma dynamics and cavitation bubble phenomenon, both of which play an extremely important role in PLA process for nanoparticle synthesis. Regarding the pressure effect on the plasma plume, Takada et al. reported that the plasma geometry becomes squeezed laterally and plasma expands parallel to the target surface plane at 30 MPa ambient pressure compared to 0.1 MPa. They also reported lesser plasma volume and higher plasma pressure for plasma formed at 30 MPa compared to 0.1 MPa. [132] Ambient pressure significantly affects the cavitation bubble dynamics also. According to Stauss et al., while the cavitation bubble lifetime for PLA of titanium in H₂O at 0.1 MPa (normal atmosphere) was few hundreds of microseconds, at 3 MPa, the lifetime reduced to around 10 μs. In addition, they reported a significant reduction in the size of the cavitation bubble at higher pressure. [135] Takada et al. reported smaller size of cavitation bubbles in 8 MPa scCO₂ compared to 5 MPa gaseous CO₂ based on shadowgraph images during PLA in pressurized CO₂ [128]. While the cavitation

bubble phenomenon in PLA in liquids is well studied, it is not well understood in case of PLA in supercritical fluids. However, a recent study by Muneoka et al. provided new insight about cavitation bubble phenomenon and nanoparticle synthesis based on shadowgraph imaging during PLA in supercritical fluids, gas-like supercritical fluids, gaseous phase, liquid-like supercritical fluids, and liquid phase (the solvent being CO₂ in different phases) [163]. In their study, based on shadowgraph imaging of plasma and cavitation bubble, they divided the whole process in six phases after irradiation of target with laser (as shown in **figure 37**). Muneoka et al. reported that while all six phases existed in PLA in near critical point supercritical CO₂, only three phases for PLA in gases and four phases for PLA in liquids was reported. The details of these phases are shown in **figure 37**. During PLA in scCO₂ at near critical point, they reported a double layer cavitation bubble which comprised of an inner bubble and an outer shell. [163] This suggests that the nanoparticle formation conditions are much different during PLA in supercritical, gaseous, and liquid phases.

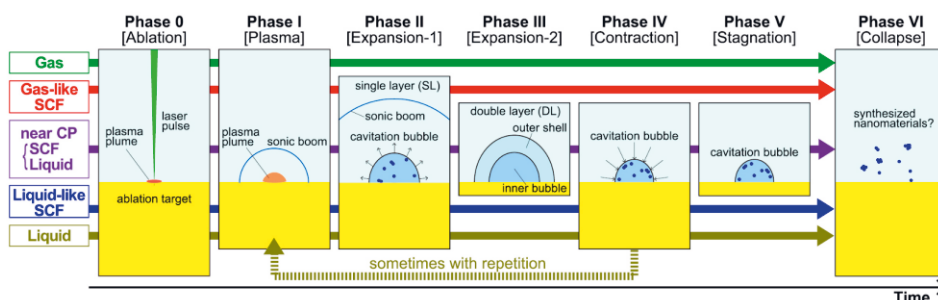


Figure 37. Schematic showing difference phases observed in the study by Muneoka et al. during PLA process from ablation (Phase 0) to nanoparticle formation (Phase 6) depending on whether the solvent was in gas phase, or gas-like supercritical fluid, or near critical point supercritical fluid, liquid-like supercritical fluid, or liquid phase. Adapted with permission from [163].

Plasma plume and cavitation bubble together form the reaction field where nanoparticles nucleate and grow. The spatial and temporal control of this reaction field by adjusting the solvent conditions is the key to materials processing [164] and controlling nanoparticle phase by PLA in high pressure media. Local pressure/temperature differences could trigger several reactions resulting in formation of mixed phases in nanoparticles [7]. Such pressure/temperature variations may result from higher ambient solvent pressure, as mentioned earlier. It is, therefore, likely that the high solvent pressure in PLA in scCO₂ compared to PLA in H₂O, could spatially and temporally change the PLA produced plasma plume and

cavitation bubble, leading to local fluctuations in temperature/pressure, which may support formation of mixed phase oxides. Supercritical fluids are known to exhibit large density fluctuations close to the critical point [128].

5.3.2 Formation of TiO₂-carbon core-shell nanoparticles by PLA in pressurized CO₂

In PLA process, the interaction of ultrashort laser pulse with the target material leads to ejection of ionized species of target to form a high temperature plasma plume over a timescale of few hundred nanoseconds, inside which, the clusters form and grow [35,58,110]. For PLA in scCO₂, the plasma formation and breakdown of CO₂ occurs over a timescale of few hundred nanoseconds, followed by cavitation bubble formation and its collapse at 2 μs and around 100 μs, respectively [130]. High temperature of plasma, reported between 3873–4873 °C [165] and 8273–12273 °C [166] depending on CO₂ pressure, leads to breakdown of CO₂ into atomic oxygen [130,166], atomic carbon [130], ions of carbon monoxide [166] and carbon [130]. This may oxidize the titanium ions, which later form titanium oxide nanoparticles, followed by deposition of the carbon on them, produced by plasma induced CO₂ decomposition.

After the plasma plume implodes, it generates cavitation bubble, wherein the ionized solvent and target species interact. In PLA in liquids at normal pressure, the cavitation bubble contains predominantly solvent species and not ablated material [126]. In context of this study, the titanium ions from target will interact with the previously plasma decomposed CO₂ in the cavitation bubble to form titanium oxides. High ambient pressure would result in shorter bubble lifetime and smaller bubble volume [131,162]. This could lead to faster quenching which may support formation of high temperature or meta-stable phases.

Cavitation bubble phenomenon during PLA in scCO₂ is reportedly similar to PLA in liquids during its growth stage while the bubble extinction stage is similar to PLA in gases [130]. During the cavitation bubble growth stage, the high temperature plasma species, released into it from the collapse of plasma, interact with ionized solvent species to form nanoparticles, which are then released to the surrounding fluid after the collapse of the bubble. In chapter 4, we observed PLA in H₂O leads to formation of mainly rutile TiO₂ nanoparticles. Rutile is indeed thermodynamically more stable form of TiO₂ than anatase [167]. However, by PLA in pressurized CO₂,

anatase-TiO₂ was the main phase of the nanoparticle despite the change in CO₂ pressure and temperature.

Huygh et al., based on density functional theory (DFT) simulations, reported that oxygen vacancies in anatase-TiO₂ can activate CO₂ dissociation and at a rather low temperature around 400 K [168]. The oxygen from CO₂ heals the vacancy while CO produced may either adsorb on particle surface. This phenomenon may have a vital role in further oxidizing the mixed phase oxides to form fully oxidized TiO₂. The CO can also decompose to form carbon via Boudouard reaction which can then form a carbon shell around the particle to form core-shell structure or the carbon can deposit around clusters of nanoparticles to form nanoparticle clusters with thick carbon layer, as observed in the STEM images in **figure 28**. This is shown as a schematic in **figure 38** for single particles. In the shell formation process, laser heating of the nanoparticles plays a vital role [169]. The particle core can also catalyze the shell formation process [71].

However, reverse Boudouard reaction can also happen above 760 °C when CO₂ combines with carbon to form CO which then may reduce TiO₂ to form oxygen deficient titanium oxides such as Ti₃O₅ or further replace oxygen with carbon to form titanium oxycarbide (Ti_xO_yC_z) [170]. Such phases were observed in the XRD spectra of nanoparticles. However, there is another pathway to form these oxides and oxycarbides. In a carbon rich environment, at temperatures over 2273 °C, TiO₂ and its other oxides become unstable and reduce to form Ti₃O₅ and Ti₂O₃ [171]. If the carbothermal reaction proceeds further, the phase changes to Ti_xO_yC_z or TiC. The phases Ti₃O₅ and Ti₍₁₎O_(0.5)C_(0.5) observed in XRD spectra could either be a result of carbothermal reduction [171] of TiO₂ or oxidation of titanium in an environment with insufficient amount of oxygen.

In situ studies with small angle x-ray scattering (SAXS), wide-angle x-ray scattering (WAXS), infrared (IR), shadowgraph imaging, and Raman spectroscopy will make good future scope of work to provide insight on this topic. For this, a new CO₂ system will have to be designed with more optical viewports to accommodate the measurements devices.

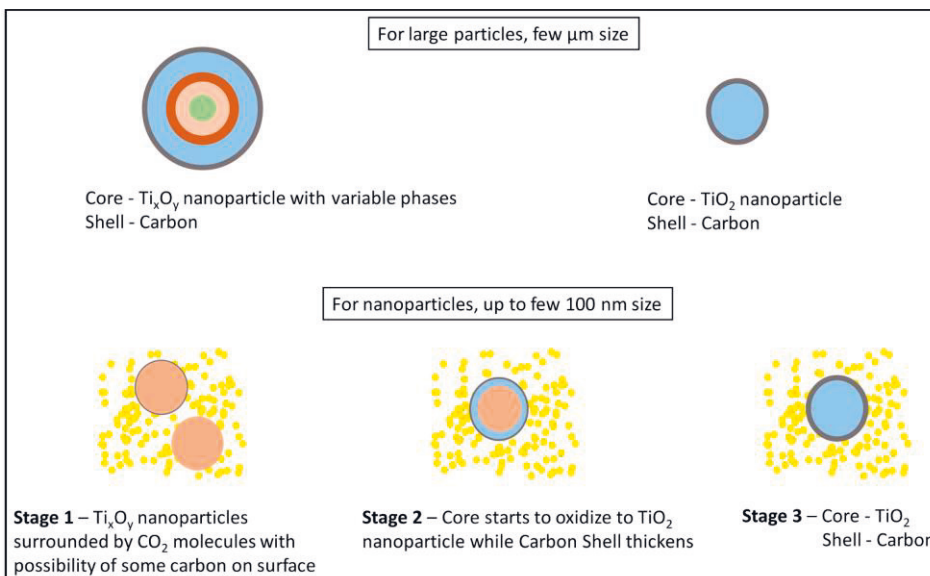


Figure 38. Schematic of a possible mechanism for decomposition of CO_2 and carbon layer formation on nanoparticles. The different colours in the particle corresponding to different layers that represent different phases of titanium oxide with blue representing fully oxidized TiO_2 . The small yellow spheres in the bottom image represent CO_2 molecules while the peach colour represents partially oxidized titanium oxide and the grey colour shell around particle represents carbon layer.

6 CONCLUDING REMARKS AND SUGGESTIONS FOR FUTURE WORK

In this thesis, results provide new insights to synthesizing nanoparticles by using PLA technique in H₂O, and supercritical CO₂ (scCO₂). Publications I and II deal exclusively with PLA in H₂O to demonstrate effect of laser power on nanoparticles and propose SAXS as a quick, promising method for nanoparticle size and size distribution measurement while publication III contributes to a comparative analysis of PLA in H₂O and PLA in scCO₂. Publication IV further demonstrates possibilities of solvent control (by changing pressure and temperature of CO₂) of PLA process on the size and phase of synthesized nanoparticles, and possibility to make core-shell nanoparticles by single step dry process.

The following points are a brief summary of the main conclusions of this thesis:

1. We demonstrated SAXS as a quick, promising particle size distribution measurement technique for size analysis directly from suspension stage of nanoparticles synthesized by PLAL. The results from SAXS were in good agreement with the tedious TEM measurements. This answers **the first research question**.
2. We demonstrated that by moving from PLA of titanium in H₂O at atmospheric pressure to PLA in scCO₂ at 10 MPa, we can synthesize meta-stable non-stoichiometric exotic oxide phases of titanium, that are well dispersed and non-agglomerated compared to mostly agglomerated, stable phase rutile-TiO₂ nanoparticles in PLA in H₂O. This answers **the second research question**. This suggests PLA in scCO₂ supports formation of meta-stable phase nanoparticles. Further, PLA in scCO₂, is not only single step method for synthesizing nanoparticles but additionally directly as dry nanoparticle powder.
3. We first reported synthesis of TiO₂-carbon core-shell nanoparticles by PLA in gaseous, liquid and supercritical CO₂. This is also the first report of PLA of a reactive metal in scCO₂ to produce nanoparticles with metal oxide core (Anatase-TiO₂) and carbon shell. The nanoparticles were mostly anatase-TiO₂. There were other non-stoichiometric and high temperature phases present such as Ti₂O₃ and Ti_xO_yC_z. The presence of these phases was

discussed based on thermodynamic analysis of the possible reactions during PLA of titanium in CO₂. Multiphase titanium

4. Additionally, we reported presence of carbon on nanoparticles synthesized by PLA in scCO₂ indicating breakdown of CO₂ to form carbon nanostructures, answering **the third research question** of this study that decomposition of CO₂ to produce carbon nanostructures at high pressure with laser (such as through ablation) is possible. For this we discussed mostly three mechanisms that could lead to breakdown of CO₂ to oxidize titanium and form carbon nanostructures around hot nanoparticles as well as present otherwise as independent carbon nanostructures.
5. We demonstrated size reduction of nanoparticles synthesized in PLA of titanium by: (1) Varying laser power, (PLA in H₂O)), and (2) by controlling CO₂ pressure and temperature (PLA in CO₂).

As a summary of this dissertation, this study shows control of nanoparticle size, size distribution, and phase by varying PLA process parameters such as laser parameters and solvent parameters. In addition, the pressure and temperature control of the solvent allows engineering of nanoparticles to some degree such as by nanoparticle synthesis in pressurized, supercritical CO₂. We demonstrated pressure and temperature control of CO₂ to control the nanoparticle size over the pressure range 5–40 MPa and temperature range 30–50 °C. Based on literature, we controlled the material science and processing of nanoparticles through spatial and temporal control of reaction fields – the plasma plume and cavitation bubble, by controlling the pressure and temperature of CO₂, which then controlled the nucleation and growth, and interaction of solute and solvent species.

For future work, in order to push this research topic further, in situ studies with SAXS, WAXS, IR imaging, shadowgraph imaging, and Raman spectroscopy would make interesting doctoral thesis topics. In addition, other interesting future works would be filling the gaps between parameters used in this dissertation, extrapolation to extreme conditions, expanding PLA in pressurized CO₂ to other metals, co-solvents, and environments. Further, changing laser and CO₂ parameters based on results from the aforementioned in-situ studies to scale-up the nanoparticle production to multigram per hour synthesis of dry nanoparticle powder as well as nanoparticle suspension on one hand, and on the other hand, producing nanoparticles from application-oriented point-of-view would be very exciting.

BIBLIOGRAPHY

- [1] A. Einstein, The Quantum Theory of Radiation, *Phys. Zeitschrift*. 18 (1917) 121–135.
- [2] T.H. Maiman, Stimulated Optical Radiation in Ruby, *Nature*. 187 (1960) 493–494. doi:10.1038/187493a0.
- [3] G. Pretzler, A. Saemann, A. Pukhov, D. Rudolph, T. Schätz, U. Schramm, P. Thirolf, D. Habs, K. Eidmann, G.D. Tsakiris, J. Meyer-ter-Vehn, K.J. Witte, Neutron production by 200 mJ ultrashort laser pulses, *Phys. Rev. E*. 58 (1998) 1165–1168. doi:10.1103/PhysRevE.58.1165.
- [4] A. Curtis, C. Calvi, J. Tinsley, R. Hollinger, V. Kaymak, A. Pukhov, S. Wang, A. Rockwood, Y. Wang, V.N. Shlyaptsev, J.J. Rocca, Micro-scale fusion in dense relativistic nanowire array plasmas, *Nat. Commun.* 9 (2018) 1077. doi:10.1038/s41467-018-03445-z.
- [5] S.B. Ogale, P.P. Patil, D.M. Phase, Y. V. Bhandarkar, S.K. Kulkarni, S. Kulkarni, S. V. Ghaisas, S.M. Kanetkar, V.G. Bhide, S. Guha, Synthesis of metastable phases via pulsed-laser-induced reactive quenching at liquid-solid interfaces, *Phys. Rev. B*. 36 (1987) 8237–8250. doi:10.1103/PhysRevB.36.8237.
- [6] P.P. Patil, D.M. Phase, S.A. Kulkarni, S. V. Ghaisas, S.K. Kulkarni, S.M. Kanetkar, S.B. Ogale, V.G. Bhide, Pulsed-laser-induced reactive quenching at liquid-solid interface: Aqueous oxidation of iron, *Phys. Rev. Lett.* 58 (1987) 238–241. doi:10.1103/PhysRevLett.58.238.
- [7] D. Zhang, B. Gökce, S. Barcikowski, Laser Synthesis and Processing of Colloids: Fundamentals and Applications, *Chem. Rev.* 117 (2017) 3990–4103. doi:10.1021/acs.chemrev.6b00468.
- [8] S. Barcikowski, G. Compagnini, Advanced nanoparticle generation and excitation by lasers in liquids, *Phys. Chem. Chem. Phys.* 15 (2013) 3022–3026. doi:10.1039/c2cp90132c.
- [9] A. Fujishima, K. Honda, Electrochemical Photolysis of Water at a Semiconductor Electrode, *Nature*. 238 (1972) 37–38. doi:10.1038/238037a0.
- [10] D. Friedmann, C. Mendive, D. Bahnemann, TiO₂ for water treatment: Parameters affecting the kinetics and mechanisms of photocatalysis, *Appl. Catal. B Environ.* 99 (2010) 398–406. doi:10.1016/j.apcatb.2010.05.014.
- [11] A. Fujishima, T.N. Rao, D. a. Tryk, Titanium dioxide photocatalysis, *J. Photochem. Photobiol. C Photochem. Rev.* 1 (2000) 1–21. doi:10.1016/S1389-5567(00)00002-2.
- [12] C.H. Ao, S.C. Lee, Indoor air purification by photocatalyst TiO₂ immobilized on an activated carbon filter installed in an air cleaner, *Chem. Eng. Sci.* 60 (2005) 103–109. doi:10.1016/j.ces.2004.01.073.

- [13] K. Tennakone, A.R. Kumarasinghe, P.M. Sirimanne, G.R.R.A. Kumara, Deposition of thin polycrystalline films of cuprous thiocyanate on conducting glass and photoelectrochemical dye-sensitization, *Thin Solid Films*. 261 (1995) 307–310. doi:10.1016/S0040-6090(95)06523-7.
- [14] I. Exnar, L. Kavan, S.Y. Huang, M. Grätzel, Novel 2 V rocking-chair lithium battery based on nano-crystalline titanium dioxide, *J. Power Sources*. 68 (1997) 720–722. doi:10.1016/S0378-7753(96)02581-5.
- [15] R. Wang, K. Hashimoto, A. Fujishima, M. Chikuni, E. Kojima, A. Kitamura, M. Shimohigoshi, T. Watanabe, Light-induced amphiphilic surfaces, *Nature*. 388 (1997) 431–432. doi:10.1038/41233.
- [16] N. Serpone, D. Dondi, A. Albini, Inorganic and organic UV filters: Their role and efficacy in sunscreens and sun care products, *Inorganica Chim. Acta*. 360 (2007) 794–802. doi:10.1016/j.ica.2005.12.057.
- [17] T. Suemori, J. Kato, T. Nakazawa, G. Akashi, A. Igarashi, Y. Hirai, Y. Kumagai, H. Kurata, Effects of light irradiation on bleaching by a 3.5% hydrogen peroxide solution containing titanium dioxide, *Laser Phys. Lett.* 5 (2008) 379–383. doi:10.1002/lapl.200710137.
- [18] Y. Suyama, M. Otsuki, S. Ogisu, R. Kishikawa, J. Tagami, M. Ikeda, H. Kurata, T. Cho, Effects of light sources and visible light-activated titanium dioxide photocatalyst on bleaching, *Dent. Mater. J.* 28 (2009) 693–699. doi:10.4012/dmj.28.693.
- [19] J.H. Braun, A. Baidins, R.E. Marganski, TiO₂ pigment technology: a review, *Prog. Org. Coatings*. 20 (1992) 105–138. doi:10.1016/0033-0655(92)80001-D.
- [20] N. Rahimi, R.A. Pax, E.M. Gray, Review of functional titanium oxides. I: TiO₂ and its modifications, *Prog. Solid State Chem.* 44 (2016) 86–105. doi:10.1016/j.progsolidchem.2016.07.002.
- [21] Z. Zhang, C.C. Wang, R. Zakaria, J.Y. Ying, Role of particle size in nanocrystalline TiO₂-based photocatalysts, *J. Phys. Chem. B*. 102 (1998) 10871–10878. doi:10.1021/jp982948+.
- [22] B. Liu, H.M. Chen, C. Liu, S.C. Andrews, C. Hahn, P. Yang, Large-scale synthesis of transition-metal-doped TiO₂ nanowires with controllable overpotential, *J. Am. Chem. Soc.* 135 (2013) 9995–9998. doi:10.1021/ja403761s.
- [23] C. Burda, Y. Lou, X. Chen, A.C.S. Samia, J. Stout, J.L. Gole, Enhanced Nitrogen Doping in TiO₂ Nanoparticles, *Nano Lett.* 3 (2003) 1049–1051. doi:10.1021/nl034332o.
- [24] D. Chen, Z. Jiang, J. Geng, Q. Wang, D. Yang, Carbon and Nitrogen Co-doped TiO₂ with Enhanced Visible-Light Photocatalytic Activity, *Ind. Eng. Chem. Res.* 46 (2007) 2741–2746. doi:10.1021/ie061491k.
- [25] P. Thakur, B. Tan, K. Venkatakrishnan, Multi-phase functionalization of titanium for enhanced photon absorption in the vis-NIR region, *Sci. Rep.* 5 (2015) 15354. doi:10.1038/srep15354.
- [26] P. Thakur, B. Tan, K. Venkatakrishnan, Multiphase titanium oxide nanomaterial for augmented vis-NIR photon absorption, *Sol. Energy Mater. Sol. Cells*. 152 (2016) 161–169. doi:10.1016/j.solmat.2016.03.037.

- [27] V.A. Zuñiga-Ibarra, S. Shaji, B. Krishnan, J. Johny, S. Sharma Kanakillam, D.A. Avellaneda, J.A.A. Martinez, T.K. Das Roy, N.A. Ramos-Delgado, Synthesis and characterization of black TiO₂ nanoparticles by pulsed laser irradiation in liquid, *Appl. Surf. Sci.* 483 (2019) 156–164. doi:10.1016/j.apsusc.2019.03.302.
- [28] J.F. Jenck, F. Agterberg, M.J. Droescher, Products and processes for a sustainable chemical industry: a review of achievements and prospects, *Green Chem.* 6 (2004) 544. doi:10.1039/b406854h.
- [29] D. Zhang, B. Gökce, S. Barcikowski, Laser Synthesis and Processing of Colloids: Fundamentals and Applications, *Chem. Rev.* 117 (2017) 3990–4103. doi:10.1021/acs.chemrev.6b00468.
- [30] J.A. Lopez-Sanchez, N. Dimitratos, C. Hammond, G.L. Brett, L. Kesavan, S. White, P. Miedziak, R. Tiruvalam, R.L. Jenkins, A.F. Carley, D. Knight, C.J. Kiely, G.J. Hutchings, Facile removal of stabilizer-ligands from supported gold nanoparticles, *Nat. Chem.* 3 (2011) 551–556. doi:10.1038/nchem.1066.
- [31] C. Uboldi, D. Bonacchi, G. Lorenzi, M.I. Hermanns, C. Pohl, G. Baldi, R.E. Unger, C.J. Kirkpatrick, Gold nanoparticles induce cytotoxicity in the alveolar type-II cell lines A549 and NCIH441, *Part. Fibre Toxicol.* 6 (2009) 18. doi:10.1186/1743-8977-6-18.
- [32] R. Lévy, N.T.K. Thanh, R.C. Doty, I. Hussain, R.J. Nichols, D.J. Schiffrin, M. Brust, D.G. Fernig, Rational and Combinatorial Design of Peptide Capping Ligands for Gold Nanoparticles, *J. Am. Chem. Soc.* 126 (2004) 10076–10084. doi:10.1021/ja0487269.
- [33] I. Ojea-Jimenez, V. Puentes, Instability of Cationic Gold Nanoparticle Bioconjugates: The Role of Citrate Ions, *J. Am. Chem. Soc.* 132 (2010) 5322–5322. doi:10.1021/ja101213s.
- [34] P. Anastas, N. Eghbali, Green Chemistry: Principles and Practice, *Chem. Soc. Rev.* 39 (2010) 301–312. doi:10.1039/B918763B.
- [35] V. Amendola, M. Meneghetti, Laser ablation synthesis in solution and size manipulation of noble metal nanoparticles., *Phys. Chem. Chem. Phys.* 11 (2009) 3805–3821. doi:10.1039/b900654k.
- [36] S. Petersen, S. Barcikowski, In Situ Bioconjugation: Single Step Approach to Tailored Nanoparticle-Bioconjugates by Ultrashort Pulsed Laser Ablation, *Adv. Funct. Mater.* 19 (2009) 1167–1172. doi:10.1002/adfm.200801526.
- [37] W. Qian, M. Murakami, Y. Ichikawa, Y. Che, Highly Efficient and Controllable PEGylation of Gold Nanoparticles Prepared by Femtosecond Laser Ablation in Water, *J. Phys. Chem. C.* 115 (2011) 23293–23298. doi:10.1021/jp2079567.
- [38] S. Kalele, S.W. Gosavi, J. Urban, S.K. Kulkarni, Nanoshell particles: Synthesis, properties and applications, *Curr. Sci.* 91 (2006) 1038–1052.
- [39] Y. Wang, X. Teng, J.-S. Wang, H. Yang, Solvent-Free Atom Transfer Radical Polymerization in the Synthesis of Fe₂O₃@Polystyrene Core–Shell Nanoparticles, *Nano Lett.* 3 (2003) 789–793. doi:10.1021/nl034211o.
- [40] Y. Kobayashi, M.A. Correa-Duarte, L.M. Liz-Marzán, Sol–Gel Processing of Silica-Coated Gold Nanoparticles, *Langmuir.* 17 (2001) 6375–6379. doi:10.1021/la010736p.
- [41] K.Z. Chen, Z.K. Zhang, Z.L. Cui, D.H. Zuo, D.Z. Yang, Catalytic properties of nanostructured hydrogen storage nickel particles with cerium shell structure,

- Nanostructured Mater. 8 (1997) 205–213. doi:10.1016/S0965-9773(97)00009-3.
- [42] D. Vollath, D. V Szabo, Coated Nanoparticles: A New Way to Improved Nanocomposites, *J. Nanoparticle Res.* 1 (1999) 235–242. doi:10.1023/A:1010060701507.
- [43] P. Biswas, C.Y. Wu, M.R. Zachariah, B. McMillin, Characterization of iron oxide-silica nanocomposites in flames: Part II. Comparison of discrete-sectional model predictions to experimental data, *J. Mater. Res.* 12 (1997) 714–723. doi:10.1557/JMR.1997.0106.
- [44] F. Yu, J.N. Wang, Z.M. Sheng, L.F. Su, Synthesis of carbon-encapsulated magnetic nanoparticles by spray pyrolysis of iron carbonyl and ethanol, *Carbon N. Y.* 43 (2005) 3018–3021. doi:10.1016/j.carbon.2005.06.008.
- [45] W. Chang, G. Skandan, H. Hahn, S.C. Danforth, B.H. Kear, Chemical vapor condensation of nanostructured ceramic powders, *Nanostructured Mater.* 4 (1994) 345–351. doi:10.1016/0965-9773(94)90144-9.
- [46] P.V. Kazakevich, A.V. Simakin, V.V. Voronov, G.A. Shafeev, D. Starikov, A. Bensaoula, Formation of Core-Shell Nanoparticles by Laser Ablation of Copper and Brass in Liquids, *Solid State Phenom.* 106 (2005) 23–26. doi:10.4028/www.scientific.net/SSP.106.23.
- [47] M.B. Gawande, A. Goswami, T. Asefa, H. Guo, A. V Biradar, D. Peng, R. Zboril, R.S. Varma, Core-shell nanoparticles: synthesis and applications in catalysis and electrocatalysis, *Chem. Soc. Rev.* 44 (2015) 7540–7590. doi:10.1039/C5CS00343A.
- [48] H. Feng, L. Tang, G. Zeng, Y. Zhou, Y. Deng, X. Ren, B. Song, C. Liang, M. Wei, J. Yu, Core-shell nanomaterials: Applications in energy storage and conversion, *Adv. Colloid Interface Sci.* 267 (2019) 26–46. doi:10.1016/j.cis.2019.03.001.
- [49] K.S. Kumar, V.B. Kumar, P. Paik, Recent Advancement in Functional Core-Shell Nanoparticles of Polymers: Synthesis, Physical Properties, and Applications in Medical Biotechnology, *J. Nanoparticles.* 2013 (2013) 1–24. doi:10.1155/2013/672059.
- [50] J. Park, T. Back, W.C. Mitchel, S.S. Kim, S. Elhamri, J. Boeckl, S.B. Fairchild, R. Naik, A.A. Voevodin, Approach to multifunctional device platform with epitaxial graphene on transition metal oxide, *Sci. Rep.* 5 (2015) 14374. doi:10.1038/srep14374.
- [51] J.-M. Lee, S.-B. Han, J.-Y. Kim, Y.-W. Lee, A.-R. Ko, B. Roh, I. Hwang, K.-W. Park, TiO₂@carbon core-shell nanostructure supports for platinum and their use for methanol electrooxidation, *Carbon N. Y.* 48 (2010) 2290–2296. doi:10.1016/j.carbon.2010.03.004.
- [52] Z. Yan, D.B. Chrisey, Pulsed laser ablation in liquid for micro-/nanostructure generation, *J. Photochem. Photobiol. C Photochem. Rev.* 13 (2012) 204–223. doi:10.1016/j.jphotochemrev.2012.04.004.
- [53] D. Vollath, Plasma Synthesis of Nanoparticles, *KONA Powder Part. J.* 25 (2007) 39–55. doi:10.14356/kona.2007007.
- [54] Q. Liu, X. Duan, C. Peng, *Novel Optical Technologies for Nanofabrication*, Springer Berlin Heidelberg, Berlin, Heidelberg, 2014. doi:10.1007/978-3-642-40387-3.
- [55] J. Neddersen, G. Chumanov, T.M. Cotton, Laser Ablation of Metals: A New Method for Preparing SERS Active Colloids, *Appl. Spectrosc.* 47 (1993) 1959–1964.

doi:10.1366/0003702934066460.

- [56] T. Sasaki, Y. Shimizu, N. Koshizaki, Preparation of metal oxide-based nanomaterials using nanosecond pulsed laser ablation in liquids, *J. Photochem. Photobiol. A Chem.* 182 (2006) 335–341. doi:10.1016/j.jphotochem.2006.05.031.
- [57] S. Dolgaev, A. Simakin, V. Voronov, Nanoparticles produced by laser ablation of solids in liquid environment, *Appl. Surf. Sci.* 186 (2002) 546–551.
- [58] V. Amendola, M. Meneghetti, What controls the composition and the structure of nanomaterials generated by laser ablation in liquid solution?, *Phys. Chem. Chem. Phys.* 15 (2013) 3027–3046. doi:10.1039/C2CP42895D.
- [59] N.G. Semaltianos, S. Logothetidis, N. Frangis, I. Tsiaoussis, W. Perrie, G. Dearden, K.G. Watkins, Laser ablation in water: A route to synthesize nanoparticles of titanium monoxide, *Chem. Phys. Lett.* 496 (2010) 113–116. doi:10.1016/j.cplett.2010.07.023.
- [60] A. V. Kabashin, M. Meunier, Synthesis of colloidal nanoparticles during femtosecond laser ablation of gold in water, *J. Appl. Phys.* 94 (2003) 7941. doi:10.1063/1.1626793.
- [61] J.-P. Sylvestre, A.V. Kabashin, E. Sacher, M. Meunier, Femtosecond laser ablation of gold in water: influence of the laser-produced plasma on the nanoparticle size distribution, *Appl. Phys. A* 80 (2005) 753–758. doi:10.1007/s00339-004-3081-4.
- [62] K. Saitow, T. Yamamura, T. Minami, Gold nanospheres and nanonecklaces generated by laser ablation in supercritical fluid, *J. Phys. Chem. C* 112 (2008) 18340–18349. <http://pubs.acs.org/doi/abs/10.1021/jp805978g>.
- [63] T. Tsuji, Y. Okazaki, Y. Tsuboi, M. Tsuji, Nanosecond Time-Resolved Observations of Laser Ablation of Silver in Water, *Jpn. J. Appl. Phys.* 46 (2007) 1533–1535. doi:10.1143/JJAP.46.1533.
- [64] M. Dell’Aglio, A. De Giacomo, S. Kohsakowski, S. Barcikowski, P. Wagener, A. Santagata, Pulsed laser ablation of wire-shaped target in a thin water jet: effects of plasma features and bubble dynamics on the PLAL process, *J. Phys. D: Appl. Phys.* 50 (2017) 185204. doi:10.1088/1361-6463/aa652a.
- [65] W.T. Nichols, T. Sasaki, N. Koshizaki, Laser ablation of a platinum target in water. II. Ablation rate and nanoparticle size distributions, *J. Appl. Phys.* 100 (2006) 114912. doi:10.1063/1.2390641.
- [66] A. De Giacomo, M. Dell’Aglio, A. Santagata, R. Gaudiuso, O. De Pascale, P. Wagener, G.C. Messina, G. Compagnini, S. Barcikowski, Cavitation dynamics of laser ablation of bulk and wire-shaped metals in water during nanoparticles production, *Phys. Chem. Chem. Phys.* 15 (2013) 3083–3092. doi:10.1039/C2CP42649H.
- [67] Y. Miyasaka, M. Hashida, T. Nishii, S. Inoue, S. Sakabe, Derivation of effective penetration depth of femtosecond laser pulses in metal from ablation rate dependence on laser fluence, incidence angle, and polarization, *Appl. Phys. Lett.* 106 (2015) 013101. doi:10.1063/1.4905353.
- [68] I. Vlădoiu, M. Stafe, C. Neagu, I.M. Popescu, Nanopulsed ablation rate of metals dependence on the laser fluence and wavelength in atmospheric air, *UPB Sci. Bull. Ser. A Appl. Math. Phys.* 70 (2008) 119–126.
- [69] Y. Kuwahara, T. Saito, M. Haba, T. Iwanaga, M. Sasaki, M. Goto, Nanosecond Pulsed

- Laser Ablation of Copper in Supercritical Carbon Dioxide, *Jpn. J. Appl. Phys.* 48 (2009) 040207. doi:10.1143/JJAP.48.040207.
- [70] K.Y. Niu, J. Yang, S.A. Kulinich, J. Sun, H. Li, X.W. Du, Morphology Control of Nanostructures via Surface Reaction of Metal Nanodroplets, *J. Am. Chem. Soc.* 132 (2010) 9814–9819. doi:10.1021/ja102967a.
- [71] G. Marzun, H. Bönemann, C. Lehmann, B. Spliethoff, C. Weidenthaler, S. Barcikowski, Role of Dissolved and Molecular Oxygen on Cu and PtCu Alloy Particle Structure during Laser Ablation Synthesis in Liquids, *ChemPhysChem.* 18 (2017) 1175–1184. doi:10.1002/cphc.201601315.
- [72] P.G. Kuzmin, G.A. Shafeev, G. Viau, B. Warot-Fonrose, M. Barberoglou, E. Stratakis, C. Fotakis, Porous nanoparticles of Al and Ti generated by laser ablation in liquids, *Appl. Surf. Sci.* 258 (2012) 9283–9287. doi:10.1016/j.apsusc.2011.08.108.
- [73] C. He, T. Sasaki, Y. Shimizu, N. Koshizaki, Synthesis of ZnO nanoparticles using nanosecond pulsed laser ablation in aqueous media and their self-assembly towards spindle-like ZnO aggregates, *Appl. Surf. Sci.* 254 (2008) 2196–2202. doi:10.1016/j.apsusc.2007.09.007.
- [74] H.S. Desarkar, P. Kumbhakar, A.K. Mitra, One-step synthesis of Zn/ZnO hollow nanoparticles by the laser ablation in liquid technique, *Laser Phys. Lett.* 10 (2013) 055903. doi:10.1088/1612-2011/10/5/055903.
- [75] R.K. Thareja, S. Shukla, Synthesis and characterization of zinc oxide nanoparticles by laser ablation of zinc in liquid, *Appl. Surf. Sci.* 253 (2007) 8889–8895. doi:10.1016/j.apsusc.2007.04.088.
- [76] G. Viau, V. Collière, L.-M. Lacroix, G.A. Shafeev, Internal structure of Al hollow nanoparticles generated by laser ablation in liquid ethanol, *Chem. Phys. Lett.* 501 (2011) 419–422. doi:10.1016/j.cplett.2010.11.032.
- [77] R. Mahfouz, F.J. Cadete Santos Aires, A. Brenier, B. Jacquier, J.C. Bertolini, Synthesis and physico-chemical characteristics of nanosized particles produced by laser ablation of a nickel target in water, *Appl. Surf. Sci.* 254 (2008) 5181–5190. doi:10.1016/j.apsusc.2008.02.022.
- [78] M. Mardis, N. Takada, S. Machmudah, Wahyudiono, K. Sasaki, H. Kanda, M. Goto, Nickel nanoparticles generated by pulsed laser ablation in liquid CO₂, *Res. Chem. Intermed.* 42 (2016) 4581–4590. doi:10.1007/s11164-015-2299-4.
- [79] G. Marzun, J. Nakamura, X. Zhang, S. Barcikowski, P. Wagener, Size control and supporting of palladium nanoparticles made by laser ablation in saline solution as a facile route to heterogeneous catalysts, *Appl. Surf. Sci.* 348 (2015) 75–84. doi:10.1016/j.apsusc.2015.01.108.
- [80] H. Zhang, C. Liang, Z. Tian, G. Wang, W. Cai, Single Phase Mn₃O₄ Nanoparticles Obtained by Pulsed Laser Ablation in Liquid and Their Application in Rapid Removal of Trace Pentachlorophenol, *J. Phys. Chem. C.* 114 (2010) 12524–12528. doi:10.1021/jp104510a.
- [81] H. Zhang, G. Duan, Y. Li, X. Xu, Z. Dai, W. Cai, Leaf-like Tungsten Oxide Nanoplatelets Induced by Laser Ablation in Liquid and Subsequent Aging, *Cryst. Growth Des.* 12 (2012) 2646–2652. doi:10.1021/cg300226r.

- [82] E. Jiménez, K. Abderrafi, R. Abargues, J.L. Valdés, J.P. Martínez-Pastor, Laser-Ablation-Induced Synthesis of SiO₂-Capped Noble Metal Nanoparticles in a Single Step, *Langmuir*. 26 (2010) 7458–7463. doi:10.1021/la904179x.
- [83] T. Sasaki, Y. Shimizu, N. Koshizaki, Preparation of metal oxide-based nanomaterials using nanosecond pulsed laser ablation in liquids, *J. Photochem. Photobiol. A Chem.* 182 (2006) 335–341. doi:10.1016/j.jphotochem.2006.05.031.
- [84] K. Saitow, Silicon Nanoclusters Selectively Generated by Laser Ablation in Supercritical Fluid, *J. Phys. Chem. B*. 109 (2005) 3731–3733. doi:10.1021/jp0442551.
- [85] A. De Giacomo, A. De Bonis, M. Dell’Aglia, O. De Pascale, R. Gaudiuso, S. Orlando, A. Santagata, G.S. Senesi, F. Taccogna, R. Teghil, Laser Ablation of Graphite in Water in a Range of Pressure from 1 to 146 atm Using Single and Double Pulse Techniques for the Production of Carbon Nanostructures, *J. Phys. Chem. C*. 115 (2011) 5123–5130. doi:10.1021/jp109389c.
- [86] L. Yang, P.W. May, L. Yin, Y. Huang, J.A. Smith, T.B. Scott, Symmetric organization of self-assembled carbon nitride, *Nanotechnology*. 18 (2007) 335605. doi:10.1088/0957-4484/18/33/335605.
- [87] L. Yang, P.W. May, Y. Huang, L. Yin, Hierarchical architecture of self-assembled carbon nitride nanocrystals, *J. Mater. Chem.* 17 (2007) 1255. doi:10.1039/b701914a.
- [88] O.R. Musaev, A.E. Midgley, J.M. Wrobel, J. Yan, M.B. Kruger, Fractal character of titania nanoparticles formed by laser ablation, *J. Appl. Phys.* 106 (2009) 054306. doi:10.1063/1.3208058.
- [89] H. Wu, R. Yang, B. Song, Q. Han, J. Li, Y. Zhang, Y. Fang, R. Tenne, C. Wang, Biocompatible Inorganic Fullerene-Like Molybdenum Disulfide Nanoparticles Produced by Pulsed Laser Ablation in Water, *ACS Nano*. 5 (2011) 1276–1281. doi:10.1021/nn102941b.
- [90] D.L. da Cunha, G.F.C. Pereira, J.F. Felix, J. Albino Aguiar, W.M. de Azevedo, Nanostructured hydrocerussite compound (Pb₃(CO₃)₂(OH)₂) prepared by laser ablation technique in liquid environment, *Mater. Res. Bull.* 49 (2014) 172–175. doi:10.1016/j.materresbull.2013.08.030.
- [91] A. De Bonis, A. Galasso, N. Ibris, A. Laurita, A. Santagata, R. Teghil, Rutile microtubes assembly from nanostructures obtained by ultra-short laser ablation of titanium in liquid, *Appl. Surf. Sci.* 268 (2013) 571–578. doi:10.1016/j.apsusc.2013.01.015.
- [92] K.Y. Niu, J. Yang, S.A. Kulinich, J. Sun, X.W. Du, Hollow Nanoparticles of Metal Oxides and Sulfides: Fast Preparation via Laser Ablation in Liquid, *Langmuir*. 26 (2010) 16652–16657. doi:10.1021/la1033146.
- [93] Z. Yan, R. Bao, D.B. Chrisey, Excimer laser ablation of a Pt target in water: the observation of hollow particles, *Nanotechnology*. 21 (2010) 145609. doi:10.1088/0957-4484/21/14/145609.
- [94] S. Yang, W. Cai, H. Zhang, H. Zeng, Y. Lei, A General Strategy for Fabricating Unique Carbide Nanostructures with Excitation Wavelength-Dependent Light Emissions, *J. Phys. Chem. C*. 115 (2011) 7279–7284. doi:10.1021/jp111873k.
- [95] D.C. Schinca, L.B. Scaffardi, F.A. Videla, G.A. Torchia, P. Moreno, L. Roso, Silver–silver oxide core–shell nanoparticles by femtosecond laser ablation: core and shell sizing by

- extinction spectroscopy, *J. Phys. D. Appl. Phys.* 42 (2009) 215102. doi:10.1088/0022-3727/42/21/215102.
- [96] A. Santagata, A. Guarnaccio, D. Pietrangeli, Á. Szegedi, J. Valyon, A. De Stefanis, A. De Bonis, R. Teghil, M. Sansone, D. Mollica, G.P. Parisi, Production of silver-silica core-shell nanocomposites using ultra-short pulsed laser ablation in nanoporous aqueous silica colloidal solutions, *J. Phys. D. Appl. Phys.* 48 (2015) 205304. doi:10.1088/0022-3727/48/20/205304.
- [97] R. Zamiri, A. Zakaria, R. Jorfi, G. Zamiri, M. Shokati Mojdehi, H. Abbastabar Ahangar, A. Khorsand Zak, Laser assisted fabrication of ZnO/Ag and ZnO/Au core/shell nanocomposites, *Appl. Phys. A*. 111 (2013) 487–493. doi:10.1007/s00339-012-7517-y.
- [98] X.D. Ren, R. Liu, L.M. Zheng, Y.P. Ren, Z.Z. Hu, H. He, Morphology selective preparation and formation mechanism of graphene nanoribbons from graphite by liquid-phase pulsed laser ablation, *Appl. Phys. Lett.* 108 (2016) 071904. doi:10.1063/1.4941801.
- [99] X.Z. Lin, P. Liu, J.M. Yu, G.W. Yang, Synthesis of CuO Nanocrystals and Sequential Assembly of Nanostructures with Shape-Dependent Optical Absorption upon Laser Ablation in Liquid, *J. Phys. Chem. C*. 113 (2009) 17543–17547. doi:10.1021/jp907237q.
- [100] Y. Wang, H. Zhang, Y. Zhu, Z. Dai, H. Bao, Y. Wei, W. Cai, Au-NP-Decorated Crystalline FeOCl Nanosheet: Facile Synthesis by Laser Ablation in Liquid and its Exclusive Gas Sensing Response to HCl at Room Temperature, *Adv. Mater. Interfaces*. 3 (2016) 1500801. doi:10.1002/admi.201500801.
- [101] C. Liang, Z. Tian, T. Tsuruoka, W. Cai, N. Koshizaki, Blue and green luminescence from layered zinc hydroxide/dodecyl sulfate hybrid nanosheets, *J. Photochem. Photobiol. A Chem.* 224 (2011) 110–115. doi:10.1016/j.jphotochem.2011.09.013.
- [102] L. Escobar-Alarcón, E. Velarde Granados, D.A. Solís-Casados, O. Olea-Mejía, M. Espinosa-Pesqueira, E. Haro-Poniatowski, Preparation of bismuth-based nanosheets by ultrasound-assisted liquid laser ablation, *Appl. Phys. A*. 122 (2016) 433. doi:10.1007/s00339-016-9992-z.
- [103] F. Mafuné, J. Kohno, Y. Takeda, T. Kondow, Formation of Gold Nanonetworks and Small Gold Nanoparticles by Irradiation of Intense Pulsed Laser onto Gold Nanoparticles, *J. Phys. Chem. B*. 107 (2003) 12589–12596. doi:10.1021/jp030173l.
- [104] F. Mafuné, T. Kondow, Selective laser fabrication of small nanoparticles and nanonetworks in solution by irradiation of UV pulsed laser onto platinum nanoparticles, *Chem. Phys. Lett.* 383 (2004) 343–347. doi:10.1016/j.cplett.2003.10.149.
- [105] A.A. Serkov, E.V. Barmina, P.G. Kuzmin, G.A. Shafeev, Self-assembly of nanoparticles into nanowires under laser exposure in liquids, *Chem. Phys. Lett.* 623 (2015) 93–97. doi:10.1016/j.cplett.2015.01.050.
- [106] A. Simakin, V. Voronov, G. Shafeev, R. Brayner, F. Bozon-Verduraz, Nanodisks of Au and Ag produced by laser ablation in liquid environment, *Chem. Phys. Lett.* 348 (2001) 182–186. doi:10.1016/S0009-2614(01)01136-8.
- [107] P. Liu, Y.L. Cao, C.X. Wang, X.Y. Chen, G.W. Yang, Micro- and Nanocubes of Carbon with C8-like and Blue Luminescence, *Nano Lett.* 8 (2008) 2570–2575. doi:10.1021/nl801392v.
- [108] P. Liu, C.X. Wang, X.Y. Chen, G.W. Yang, Controllable Fabrication and

- Cathodoluminescence Performance of High-index Facets GeO₂ Micro- and Nanocubes and Spindles upon Electrical-field-assisted Laser Ablation in Liquid, *J. Phys. Chem. C.* 112 (2008) 13450–13456. doi:10.1021/jp802529r.
- [109] S.Z. Khan, Y. Yuan, A. Abdolvand, M. Schmidt, P. Crouse, L. Li, Z. Liu, M. Sharp, K.G. Watkins, Generation and characterization of NiO nanoparticles by continuous wave fiber laser ablation in liquid, *J. Nanoparticle Res.* 11 (2009) 1421–1427. doi:10.1007/s11051-008-9530-9.
- [110] C.-Y. Shih, C. Wu, M. V. Shugaev, L. V. Zhigilei, Atomistic modeling of nanoparticle generation in short pulse laser ablation of thin metal films in water, *J. Colloid Interface Sci.* 489 (2017) 3–17. doi:10.1016/j.jcis.2016.10.029.
- [111] C.-Y. Shih, R. Streubel, J. Heberle, A. Letzel, M. V. Shugaev, C. Wu, M. Schmidt, B. Gökce, S. Barcikowski, L. V. Zhigilei, Two mechanisms of nanoparticle generation in picosecond laser ablation in liquids: the origin of the bimodal size distribution, *Nanoscale.* 10 (2018) 6900–6910. doi:10.1039/C7NR08614H.
- [112] C. Doñate-Buendía, F. Frömel, M.B. Wilms, R. Streubel, J. Tenkamp, T. Hupfeld, M. Nachev, E. Gökce, A. Weisheit, S. Barcikowski, F. Walther, J.H. Schleifenbaum, B. Gökce, Oxide dispersion-strengthened alloys generated by laser metal deposition of laser-generated nanoparticle-metal powder composites, *Mater. Des.* 154 (2018) 360–369. doi:10.1016/j.matdes.2018.05.044.
- [113] W.T. Nichols, T. Sasaki, N. Koshizaki, Laser ablation of a platinum target in water. III. Laser-induced reactions, *J. Appl. Phys.* 100 (2006) 114913. doi:10.1063/1.2390642.
- [114] Z. Lin, E. Leveugle, E.M. Bringa, L. V. Zhigilei, Molecular Dynamics Simulation of Laser Melting of Nanocrystalline Au, *J. Phys. Chem. C.* 114 (2010) 5686–5699. doi:10.1021/jp909328q.
- [115] S. Leyder, D. Grojo, P. Delaporte, W. Marine, M. Sentis, O. Utéza, Non-linear absorption of focused femtosecond laser pulses at 1.3 μ m inside silicon: Independence on doping concentration, *Appl. Surf. Sci.* 278 (2013) 13–18. doi:10.1016/j.apsusc.2012.10.174.
- [116] J. Lam, D. Amans, F. Chaput, M. Diouf, G. Ledoux, N. Mary, K. Masenelli-Varlot, V. Motto-Ros, C. Dujardin, γ -Al₂O₃ nanoparticles synthesised by pulsed laser ablation in liquids: a plasma analysis, *Phys. Chem. Chem. Phys.* 16 (2014) 963–973. doi:10.1039/C3CP53748J.
- [117] R. Zamiri, A. Zakaria, H.A. Ahangar, M. Darroudi, G. Zamiri, Z. Rizwan, G.P. Drummen, The effect of laser repetition rate on the LASiS synthesis of biocompatible silver nanoparticles in aqueous starch solution, *Int. J. Nanomedicine.* 8 (2013) 233. doi:10.2147/IJN.S36036.
- [118] K. Metwally, S. Mensah, G. Baffou, Fluence Threshold for Photothermal Bubble Generation Using Plasmonic Nanoparticles, *J. Phys. Chem. C.* 119 (2015) 28586–28596. doi:10.1021/acs.jpcc.5b09903.
- [119] A. Resano-Garcia, Y. Battie, A.E. Naciri, N. Chaoui, Interaction of a converging laser beam with a Ag colloidal solution during the ablation of a Ag target in water, *Nanotechnology.* 27 (2016) 215705. doi:10.1088/0957-4484/27/21/215705.
- [120] R. Fabbro, J. Fournier, P. Ballard, D. Devaux, J. Virmont, Physical study of laser-

- produced plasma in confined geometry, *J. Appl. Phys.* 68 (1990) 775–784. doi:10.1063/1.346783.
- [121] L. Berthe, R. Fabbro, P. Peyre, L. TOLLIER, E. Bartnicki, Shock waves from a water-confined laser-generated plasma, *J. Appl. Phys.* 82 (1997) 2826–2832. doi:10.1063/1.366113.
- [122] T. Tsuji, Y. Tsuboi, N. Kitamura, M. Tsuji, Microsecond-resolved imaging of laser ablation at solid–liquid interface: investigation of formation process of nano-size metal colloids, *Appl. Surf. Sci.* 229 (2004) 365–371. doi:10.1016/j.apsusc.2004.02.013.
- [123] K. Sasaki, N. Takada, Liquid-phase laser ablation, *Pure Appl. Chem.* 82 (2010) 1317–1327. doi:10.1351/PAC-CON-09-10-23.
- [124] W. Soliman, N. Takada, K. Sasaki, Growth Processes of Nanoparticles in Liquid-Phase Laser Ablation Studied by Laser-Light Scattering, *Appl. Phys. Express.* 3 (2010) 035201. doi:10.1143/APEX.3.035201.
- [125] V. Lazic, S. Jovicic, M. Carpanese, Laser induced bubbles inside liquids: Transient optical properties and effects on a beam propagation, *Appl. Phys. Lett.* 101 (2012) 054101. doi:10.1063/1.4739851.
- [126] J. Lam, J. Lombard, C. Dujardin, G. Ledoux, S. Merabia, D. Amans, Dynamical study of bubble expansion following laser ablation in liquids, *Appl. Phys. Lett.* 108 (2016) 074104. doi:10.1063/1.4942389.
- [127] W. Leitner, Designed to dissolve, *Nature.* 405 (2000) 129–130. doi:10.1038/35012181.
- [128] N. Takada, S. Machmudah, H. Goto, Wahyudiono, M. Goto, K. Sasaki, Characteristics of optical emission intensities and bubblelike phenomena induced by laser ablation in supercritical fluids, *Jpn. J. Appl. Phys.* 53 (2014) 010213. doi:10.7567/JJAP.53.010213.
- [129] S. Machmudah, Y. Kuwahara, M. Sasaki, M. Goto, Nano-structured particles production using pulsed laser ablation of gold plate in supercritical CO₂, *J. Supercrit. Fluids.* 60 (2011) 63–68. doi:10.1016/j.supflu.2011.04.008.
- [130] T. Kato, S. Stauss, S. Kato, K. Urabe, M. Baba, T. Suemoto, K. Terashima, Pulsed laser ablation plasmas generated in CO₂ under high-pressure conditions up to supercritical fluid, *Appl. Phys. Lett.* 101 (2012) 224103. doi:10.1063/1.4767839.
- [131] K. Sasaki, T. Nakano, W. Soliman, N. Takada, Effect of Pressurization on the Dynamics of a Cavitation Bubble Induced by Liquid-Phase Laser Ablation, *Appl. Phys. Express.* 2 (2009) 046501. doi:10.1143/APEX.2.046501.
- [132] N. Takada, T. Nakano, K. Sasaki, Influence of additional external pressure on optical emission intensity in liquid-phase laser ablation, *Appl. Surf. Sci.* 255 (2009) 9572–9575. doi:10.1016/j.apsusc.2009.04.087.
- [133] M.S. Plesset, A. Prosperetti, Bubble Dynamics and Cavitation, *Annu. Rev. Fluid Mech.* 9 (1977) 145–185. doi:10.1146/annurev.fl.09.010177.001045.
- [134] W. Soliman, T. Nakano, N. Takada, K. Sasaki, Modification of Rayleigh–Plesset Theory for Reproducing Dynamics of Cavitation Bubbles in Liquid-Phase Laser Ablation, *Jpn. J. Appl. Phys.* 49 (2010) 116202. doi:10.1143/JJAP.49.116202.
- [135] S. Stauss, K. Urabe, H. Muneoka, K. Terashima, Pulsed Laser Ablation in High-Pressure Gases, Pressurized Liquids and Supercritical Fluids: Generation, Fundamental

- Characteristics and Applications, in: *Appl. Laser Ablation - Thin Film Depos. Nanomater. Synth. Surf. Modif., InTech*, 2016. doi:10.5772/65455.
- [136] S. Barcikowski, A. Plech, K.S. Suslick, A. Vogel, Materials synthesis in a bubble, *MRS Bull.* 44 (2019) 382–391. doi:10.1557/mrs.2019.107.
- [137] T. Hupfeld, G. Laurens, S. Merabia, S. Barcikowski, B. Gökce, D. Amans, Dynamics of laser-induced cavitation bubbles at a solid–liquid interface in high viscosity and high capillary number regimes, *J. Appl. Phys.* 127 (2020) 044306. doi:10.1063/1.5116111.
- [138] S. Nakahara, S. Stauss, T. Kato, T. Sasaki, K. Terashima, Synthesis of higher diamondoids by pulsed laser ablation plasmas in supercritical CO₂, *J. Appl. Phys.* 109 (2011) 123304 (1–8). doi:10.1063/1.3599887.
- [139] S. Machmudah, N. Takada, H. Kanda, K. Sasaki, M. Goto, Fabrication of gold and silver nanoparticles with pulsed laser ablation under pressurized CO₂, *Adv. Nat. Sci. Nanosci. Nanotechnol.* 4 (2013) 045011. doi:10.1088/2043-6262/4/4/045011.
- [140] M. Mardis, Wahyudiono, N. Takada, H. Kanda, M. Goto, Formation of Au-carbon nanoparticles by laser ablation under pressurized CO₂, *Asia-Pacific J. Chem. Eng.* 13 (2018) e2176. doi:10.1002/apj.2176.
- [141] K.I. Saitow, Y. Okamoto, Y.F. Yano, Fractal of gold nanoparticles controlled by ambient dielectricity: Synthesis by laser ablation as a function of permittivity, *J. Phys. Chem. C.* 116 (2012) 17252–17258. doi:10.1021/jp304109h.
- [142] M. Procházka, Probing applications of laser-ablated Ag colloids in SERS spectroscopy: Improvement of ablation procedure and SERS spectral testing, *Anal. Chem.* 69 (1997) 5103–5108. doi:10.1021/ac970683+.
- [143] A. Schwenke, P. Wagener, S. Nolte, S. Barcikowski, Influence of processing time on nanoparticle generation during picosecond-pulsed fundamental and second harmonic laser ablation of metals in tetrahydrofuran, *Appl. Phys. A.* 104 (2011) 77–82. doi:10.1007/s00339-011-6398-9.
- [144] F. Mafuné, J. Kohno, Y. Takeda, T. Kondow, H. Sawabe, Formation of Gold Nanoparticles by Laser Ablation in Aqueous Solution of Surfactant, *J. Phys. Chem. B.* 105 (2001) 5114–5120. doi:10.1021/jp0037091.
- [145] A. Pyatenko, H. Wang, N. Koshizaki, T. Tsuji, Mechanism of pulse laser interaction with colloidal nanoparticles, *Laser Photon. Rev.* 7 (2013) 596–604. doi:10.1002/lpor.201300013.
- [146] G. Ledoux, D. Amans, C. Dujardin, K. Masenelli-Varlot, Facile and rapid synthesis of highly luminescent nanoparticles via pulsed laser ablation in liquid, *Nanotechnology.* 20 (2009) 445605. doi:10.1088/0957-4484/20/44/445605.
- [147] M. Kalus, N. Bärsch, R. Streubel, E. Gökce, S. Barcikowski, B. Gökce, How persistent microbubbles shield nanoparticle productivity in laser synthesis of colloids – quantification of their volume, dwell dynamics, and gas composition, *Phys. Chem. Chem. Phys.* 19 (2017) 7112–7123. doi:10.1039/C6CP07011F.
- [148] D. Werner, S. Hashimoto, Improved Working Model for Interpreting the Excitation Wavelength- and Fluence-Dependent Response in Pulsed Laser-Induced Size Reduction of Aqueous Gold Nanoparticles, *J. Phys. Chem. C.* 115 (2011) 5063–5072. doi:10.1021/jp109255g.

- [149] A. Agbabiaka, M. Wilfong, C. Park, Small Angle X-Ray Scattering Technique for the Particle Size Distribution of Nonporous Nanoparticles, *J. Nanoparticles*. 2013 (2013) 11. doi:<http://dx.doi.org/10.1155/2013/640436>.
- [150] J. Lam, D. Amans, C. Dujardin, G. Ledoux, A.-R. Allouche, Atomistic Mechanisms for the Nucleation of Aluminum Oxide Nanoparticles, *J. Phys. Chem. A*. 119 (2015) 8944–8949. doi:[10.1021/acs.jpca.5b05829](https://doi.org/10.1021/acs.jpca.5b05829).
- [151] X.-D. Wang, X.-F. Gao, C.-J. Xuan, S.X. Tian, Dissociative electron attachment to CO₂ produces molecular oxygen, *Nat. Chem.* 8 (2016) 258–263. doi:[10.1038/nchem.2427](https://doi.org/10.1038/nchem.2427).
- [152] Z. Lu, Y.C. Chang, Q.-Z. Yin, C.Y. Ng, W.M. Jackson, Evidence for direct molecular oxygen production in CO₂ photodissociation, *Science* (80-.). 346 (2014) 61–64. doi:[10.1126/science.1257156](https://doi.org/10.1126/science.1257156).
- [153] D.R. Gaskell, *Introduction to the Thermodynamics of Materials*, Taylor and Francis, London, 1995.
- [154] H.J. Jung, M.Y. Choi, One-pot synthesis of graphitic and nitrogen-doped graphitic layers on nickel nanoparticles produced by pulsed laser ablation in liquid: Solvent as the carbon and nitrogen source, *Appl. Surf. Sci.* 457 (2018) 1050–1056. doi:[10.1016/j.apsusc.2018.07.036](https://doi.org/10.1016/j.apsusc.2018.07.036).
- [155] P. Wagener, J. Jakobi, C. Rehbock, V.S.K. Chakravadhanula, C. Thede, U. Wiedwald, M. Bartsch, L. Kienle, S. Barcikowski, Solvent-surface interactions control the phase structure in laser-generated iron-gold core-shell nanoparticles, *Sci. Rep.* 6 (2016) 1–12. doi:[10.1038/srep23352](https://doi.org/10.1038/srep23352).
- [156] D. Reyes-Coronado, G. Rodríguez-Gattorno, M.E. Espinosa-Pesqueira, C. Cab, R. de Coss, G. Oskam, Phase-pure TiO₂ nanoparticles: anatase, brookite and rutile, *Nanotechnology*. 19 (2008) 145605. doi:[10.1088/0957-4484/19/14/145605](https://doi.org/10.1088/0957-4484/19/14/145605).
- [157] Y. Wang, N. Herron, Nanometer-sized semiconductor clusters: materials synthesis, quantum size effects, and photophysical properties, *J. Phys. Chem.* 95 (1991) 525–532. doi:[10.1021/j100155a009](https://doi.org/10.1021/j100155a009).
- [158] K.M. Reddy, S. V. Manorama, A.R. Reddy, Bandgap studies on anatase titanium dioxide nanoparticles, *Mater. Chem. Phys.* 78 (2003) 239–245. doi:[10.1016/S0254-0584\(02\)00343-7](https://doi.org/10.1016/S0254-0584(02)00343-7).
- [159] P. Wagener, S. Ibrahimkutty, A. Menzel, A. Plech, S. Barcikowski, Dynamics of silver nanoparticle formation and agglomeration inside the cavitation bubble after pulsed laser ablation in liquid, *Phys. Chem. Chem. Phys.* 15 (2013) 3068–3074. doi:[10.1039/C2CP42592K](https://doi.org/10.1039/C2CP42592K).
- [160] S. Ibrahimkutty, P. Wagener, T.D.S. Rolo, D. Karpov, A. Menzel, T. Baumbach, S. Barcikowski, A. Plech, A hierarchical view on material formation during pulsed-laser synthesis of nanoparticles in liquid, *Sci. Rep.* 5 (2015) 16313. doi:[10.1038/srep16313](https://doi.org/10.1038/srep16313).
- [161] M. Koizumi, S.A. Kulinich, Y. Shimizu, T. Ito, Slow dynamics of ablated zone observed around the density fluctuation ridge of fluid medium, *J. Appl. Phys.* 114 (2013) 214301. doi:[10.1063/1.4834517](https://doi.org/10.1063/1.4834517).
- [162] S.A. Kulinich, T. Kondo, Y. Shimizu, T. Ito, Pressure effect on ZnO nanoparticles prepared via laser ablation in water, *J. Appl. Phys.* 113 (2013) 033509. doi:[10.1063/1.4775733](https://doi.org/10.1063/1.4775733).

- [163] H. Muneoka, S. Himeno, K. Urabe, S. Stauss, M. Baba, T. Suemoto, K. Terashima, Dynamics of cavitation bubbles formed by pulsed-laser ablation plasmas near the critical point of CO₂, *J. Phys. D. Appl. Phys.* 52 (2019) 025201. doi:10.1088/1361-6463/aae44a.
- [164] K. Urabe, T. Kato, S. Stauss, S. Himeno, S. Kato, H. Muneoka, M. Baba, T. Suemoto, K. Terashima, Dynamics of pulsed laser ablation in high-density carbon dioxide including supercritical fluid state, *J. Appl. Phys.* 114 (2013). doi:10.1063/1.4824538.
- [165] T. Machara, A. Kawashima, A. Iwamae, S. Mukasa, T. Takemori, T. Watanabe, K. Kurokawa, H. Toyota, S. Nomura, Spectroscopic measurements of high frequency plasma in supercritical carbon dioxide, *Phys. Plasmas*. 16 (2009) 033503. doi:10.1063/1.3091927.
- [166] T. Furusato, N. Ashizuka, T. Kamagahara, Y. Matsuda, T. Yamashita, M. Sasaki, T. Kiyan, Y. Inada, Anomalous plasma temperature at supercritical phase of pressurized CO₂ after pulsed breakdown followed by large short-circuit current, *IEEE Trans. Dielectr. Electr. Insul.* 25 (2018) 1807–1813. doi:10.1109/TDEI.2018.007213.
- [167] Z.-H. Cui, F. Wu, H. Jiang, First-principles study of relative stability of rutile and anatase TiO₂ using the random phase approximation, *Phys. Chem. Chem. Phys.* 18 (2016) 29914–29922. doi:10.1039/C6CP04973G.
- [168] S. Huygh, A. Bogaerts, E.C. Neyts, How Oxygen Vacancies Activate CO₂ Dissociation on TiO₂ Anatase (001), *J. Phys. Chem. C*. 120 (2016) 21659–21669. doi:10.1021/acs.jpcc.6b07459.
- [169] T. Salminen, M. Honkanen, T. Niemi, Coating of gold nanoparticles made by pulsed laser ablation in liquids with silica shells by simultaneous chemical synthesis, *Phys. Chem. Chem. Phys.* 15 (2013) 3047–3051. doi:10.1039/C2CP42999C.
- [170] A. Hajalilou, M. Hashim, R. Ebrahimi-Kahizsangi, I. Ismail, N. Sarami, Synthesis of titanium carbide and TiC–SiO₂ nanocomposite powder using rutile and Si by mechanically activated sintering, *Adv. Powder Technol.* 25 (2014) 1094–1102. doi:10.1016/j.apt.2014.02.008.
- [171] J. Kim, S. Kang, Stable phase domains of the TiO₂–Ti₃O₅–Ti₂O₃–TiO–Ti(C_xO_y)–TiC system examined experimentally and via first principles calculations, *J. Mater. Chem. A*. 2 (2014) 2641–2647. doi:10.1039/C3TA14633B.

APPENDIX

Appendix 1: Panalytical's HighScore Plus XRD data for Titanium Oxide $\text{Ti}_1\text{O}_{0.89}$

Appendix 2: Panalytical's HighScore Plus XRD data for Titanium Oxide Carbide $\text{Ti}_1\text{C}_{0.5}\text{O}_{0.5}$

Appendix 3: Panalytical's HighScore Plus XRD data for Titanium Oxide Ti_3O_5

Appendix 1

Panalytical's HighScore Plus XRD data for Titanium Oxide $\text{TiO}_{0.89}$

REFERENCE CODE	01-078-0720					
Compound Name	Titanium Oxide					
Chemical Formula	$\text{Ti}_1\text{O}_{0.89}$					
Crystal system	Cubic					
Peak List						
No.	h	k	l	d [Å]	2Theta [deg]	Intensity [%]
1	1	1	1	2.41910	37.135	63.6
2	2	0	0	2.09500	43.146	100.0
3	2	2	0	1.48139	62.662	45.7
4	3	1	1	1.26333	75.141	15.9
5	2	2	2	1.20955	79.114	11.5

Appendix 2

Panalytical's HighScore Plus XRD data for Titanium Oxide Carbide $\text{Ti}_1\text{C}_{0.5}\text{O}_{0.5}$

REFERENCE CODE		04-021-7420					
Compound Name	Titanium Oxide Carbide						
Chemical Formula	$\text{Ti}_1\text{C}_{0.5}\text{O}_{0.5}$						
Crystal system	Cubic						
Peak List							
No.	h	k	l	d [Å]	2Theta [deg]	Intensity [%]	
1	1	1	1	2.47510	36.265	69.7	
2	2	0	0	2.14350	42.122	100.0	
3	2	2	0	1.51568	61.091	46.6	
4	3	1	1	1.29258	73.159	17.5	
5	2	2	2	1.23755	76.989	11.9	
6	4	0	0	1.07175	91.899	4.6	

Appendix 3

Panalytical's HighScore Plus XRD data for Titanium Oxide Ti_3O_5

REFERENCE CODE		04-007-8868				
Compound Name	Titanium Oxide					
Chemical Formula	Ti_3O_5					
Crystal system	Monoclinic					
Peak List						
No.	h	k	l	d [Å]	2Theta [deg]	Intensity [%]
1	0	0	1	9.74406	9.068	5.8
2	0	0	2	4.87203	18.194	3.7
3	2	0	1	4.18883	21.193	23.0
4	1	1	0	3.57254	24.903	100.0
5	-2	0	2	3.44965	25.806	6.3
6	0	0	3	3.24802	27.438	31.1
7	0	2	0	1.93000	47.046	37.7
8	-5	1	2	1.61683	56.904	17.7
9	4	2	0	1.49365	62.091	0.1
10	-4	2	3	1.36880	68.493	3.3
11	1	3	0	1.27486	74.346	2.1
12	6	0	5	1.24515	79.601	0.8

PUBLICATIONS

PUBLICATION

I

Pulsed Laser Ablation-Induced Green Synthesis of TiO₂ Nanoparticles and Application of Novel Small Angle X-Ray Scattering Technique for Nanoparticle Size and Size Distribution Analysis

A. Singh, J. Vihinen, E. Frankberg, L. Hyvärinen, M. Honkanen, and E. Levänen

Nanoscale Research. Letters, Vol. 11, p. 447

<https://doi.org/10.1186/s11671-016-1608-1>


Publication reprinted with the permission of the copyright holders.

NANO EXPRESS

Open Access



Pulsed Laser Ablation-Induced Green Synthesis of TiO₂ Nanoparticles and Application of Novel Small Angle X-Ray Scattering Technique for Nanoparticle Size and Size Distribution Analysis

Amandeep Singh^{1*} , Jorma Vihinen², Erka Frankberg¹, Leo Hyvärinen¹, Mari Honkanen¹ and Erkki Levänen¹

Abstract

This paper aims to introduce small angle X-ray scattering (SAXS) as a promising technique for measuring size and size distribution of TiO₂ nanoparticles. In this manuscript, pulsed laser ablation in liquids (PLAL) has been demonstrated as a quick and simple technique for synthesizing TiO₂ nanoparticles directly into deionized water as a suspension from titanium targets. Spherical TiO₂ nanoparticles with diameters in the range 4–35 nm were observed with transmission electron microscopy (TEM). X-ray diffraction (XRD) showed highly crystalline nanoparticles that comprised of two main photoactive phases of TiO₂: anatase and rutile. However, presence of minor amounts of brookite was also reported. The traditional methods for nanoparticle size and size distribution analysis such as electron microscopy-based methods are time-consuming. In this study, we have proposed and validated SAXS as a promising method for characterization of laser-ablated TiO₂ nanoparticles for their size and size distribution by comparing SAXS- and TEM-measured nanoparticle size and size distribution. SAXS- and TEM-measured size distributions closely followed each other for each sample, and size distributions in both showed maxima at the same nanoparticle size. The SAXS-measured nanoparticle diameters were slightly larger than the respective diameters measured by TEM. This was because SAXS measures an agglomerate consisting of several particles as one big particle which slightly increased the mean diameter. TEM- and SAXS-measured mean diameters when plotted together showed similar trend in the variation in the size as the laser power was changed which along with extremely similar size distributions for TEM and SAXS validated the application of SAXS for size distribution measurement of the synthesized TiO₂ nanoparticles.

Keywords: Nanoparticles, Pulsed laser ablation in liquids, Nanoparticle synthesis, Nanoparticle size and size distribution analysis, TEM, SAXS, XRD

Background

Nanotechnology has eminently transformed the technology sector in the last few decades. It includes the atomic level analysis and manipulation of materials. It has been the center of interest for material scientists, chemists, and physicists from the past several decades. The production of nanoparticles accounts for a substantial portion in the field

of nanotechnology. This includes production and processing of nanoparticles of several materials such as metals, semiconductors, carbon, metal oxides, and metal carbides.

The prevailing methods for the production of nanomaterials such as graphene are chemical vapor deposition and chemical exfoliation that are toxic and batch-type processes [1]. As these processes use toxic chemicals, therefore, they are precarious and potentially detrimental for the environment. Ogale et al. in 1992 discovered formation of nanoparticles when materials immersed in water were ablated by a pulsed laser [2]. Pulsed laser

* Correspondence: amandeep.singh@tut.fi

¹Department of Materials Science, Tampere University of Technology, P. O. Box 589, FIN 33101 Tampere, Finland

Full list of author information is available at the end of the article

ablation in liquids (PLAL) allows production of nanoparticles with no by-products [3]. In this method, irradiation of a target material with ultra-short laser pulse leads to formation of high-temperature plasma and removal of material, which has been termed as pulsed laser ablation [4]. Researchers have reported synthesis of nanoparticles of pure metal, metal oxide, and metal carbide by pulsed laser ablation [5–11]. With this clean and versatile technique, high-purity nanoparticle can be synthesized, which are well suited for functionalization [12–14]. The determination of the size and size distribution of nanoparticles, as part of their characterization, is of utmost importance in order to effectively use nanoparticles. The control of nanoparticle size is indispensable; however, in order to control it, it is necessary to quantify the size. The size of nanoparticles can be analyzed by various methods such as dynamic light scattering (DLS), atomic force microscopy (AFM), transmission electron microscopy (TEM), scanning electron microscopy (SEM), differential mobility analysis (DMA), and small angle X-ray scattering (SAXS) [15]. SAXS has several advantages over the conventional methods that are used to analyze the nanoparticles. The list types of samples that can be analyzed by SAXS are extensive, and the sample preparation is very quick especially when compared to preparation for electron microscopy samples. Another advantage of the technique is that the measurements are more reliable since the analysis is made over a much larger number of particles than what can be measured from TEM images [15]. DLS and DMA are not able to evaluate particles in thin films while it is possible with SAXS. DLS measurement relies on the temperature and concentration of the solution [16]. Agbabiaka et al. have proposed small angle X-ray scattering as a promising method for measurement of nanoparticle size [15]. Vippola et al. have reported SAXS as an excellent method for size analysis of small spherical particles [17]. However, this technique has never been applied and verified for pulsed laser-ablated TiO_2 nanoparticles to the best of our knowledge. So, the aim is synthesis of TiO_2 nanoparticles followed by application and verification of small angle X-ray scattering for characterization of TiO_2 nanoparticle size.

The present study deals with (i) synthesis of TiO_2 nanoparticles by PLAL, (ii) characterization of TiO_2 nanoparticles, and (iii) application and verification of SAXS for size and size distribution analysis of TiO_2 nanoparticles.

Methods

For carrying out the pulsed laser ablation test, the experimental setup (schematic shown in Fig. 1) consisted of a nanosecond 85W fiber laser (1062 nm, pulse length 500 ns, 25 kHz), titanium target, test vessel, and a computer-controlled XY scanner connected to the laser

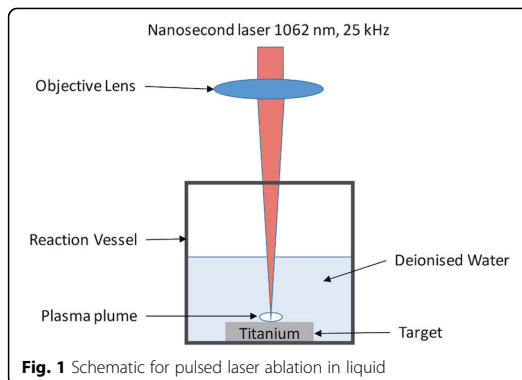


Fig. 1 Schematic for pulsed laser ablation in liquid

to scan it on a predetermined area on the target. The target, immersed in deionized water (DIW), was irradiated with this laser from the top, perpendicular to the plane of the target. The laser beam was focused on the target using a lens having focal length 160 mm. The maximum laser fluence possible with this laser was 58.92 J/cm^2 . As the spot diameter of the laser varied with the laser power, the measured laser fluences of the laser also varied from 34.65 J/cm^2 at 20 % laser power (LP) to 58.92 J/cm^2 at 40 % LP and to 43.22 J/cm^2 at 50 % LP. The ablation threshold fluence for titanium was reported to be $\sim 4.5 \text{ J/cm}^2$ with an Nd:YAG laser (1064 nm, pulse length 4.5 ns, 10 kHz) [18].

Materials and Synthesis

Titanium (99.99 % pure), obtained from Goodfellow Cambridge Limited, in the form of foil of thickness 3.2 mm, length 50 mm, and width 50 mm was cut into several smaller targets by using Struers Accutom-50 precision cutter. All these targets were identical in size, $15 \text{ mm} \times 15 \text{ mm}$, and ablated area on target surface was $8 \text{ mm} \times 8 \text{ mm}$ for each target in ablation experiments. For the experiments, only DIW was used and no chemicals were used for the nanoparticle synthesis. Small LDPE bottles, ordered from VWR International Limited, were used for storing the synthesized nanoparticle suspensions. The ultrasonically cleaned target was fixed inside the test vessel at its base and then filled with DIW such that the thickness of the water film above the target was 5 mm. For each ablation experiment, the scanning area or ablated area was $8 \text{ mm} \times 8 \text{ mm}$ and the scanning speed was 2000 mm/s. The scanning parameters were the same for each target in all ablation experiments. The direction of scanning was top to bottom followed by right to left which was repeated loop by loop of the scanning cycles. Each scanning loop was 2.566 s long. The number of loops was 720 corresponding to an ablation test of 30-min duration. This high value of scanning

speed was chosen in order to have the least number of laser pulses coincident at a point.

Characterization of Synthesized Particles

TEM imaging was performed with a Jeol JEM-2010 microscope. For imaging the nanoparticles, the acceleration voltage for TEM was 200 kV in each case. The TEM samples were prepared from freshly ablated suspensions so that there is least agglomeration. Nanoparticle dispersions were dropped on copper grids with a holey carbon film. From the same samples, electron diffraction patterns were also obtained. These techniques were used to characterize the shape, size, and crystallinity of nanoparticles. X-ray diffraction and X-ray scattering measurements were performed on a Panalytical Empyrean Multipurpose Diffractometer with anode material copper. It used Cu K α radiation (wavelength 0.15418 nm) powered by X-ray generator at 45 kV and 40 mA and a solid-state pixel detector, PIXcel3D, which measured the scattered intensities as a function of scattering angle (2θ). For X-ray diffraction (XRD) measurements, the scan range was 20.00°–80.95° with a 0.05° step size. It used a soller slit with 0.04 radian opening. For SAXS measurements, the scan range was from -0.12° to 5.01° with a 0.01° step size and it utilized a parallel beam X-ray mirror for Cu radiation. SAXS was performed on nanoparticle suspensions while for XRD measurements, the nanoparticle suspensions were dried to obtain nanoparticle powder. For SAXS sample, equal volume of each suspension was enclosed between two Mylar foils (which were X-ray transparent) and finally placed between the respective circular transmission holders for each SAXS sample. DIW enclosed between two Mylar foils was used as the background sample. The phase identification of the peaks in the XRD pattern was done with Panalytical HighScore Plus software (version 3.0.5).

Measurement of Nanoparticle Size and Size Distribution

The nanoparticle sizes were measured by SAXS and compared with the nanoparticle size measurements from TEM image analysis done manually. With SAXS measurement, we obtained the mean particle size, most frequent particle size, and the size distribution of particles by volume. The experimental data from SAXS was analyzed by Panalytical's EasySAXS software (version 2.0a) to obtain the volume-weighted particle size distribution, D_v , by indirect Fourier transform method. With this method, the result from EasySAXS is a plot between particle size and distribution volume ratio, i.e., $D_v(R)$, showing size distribution of nanoparticles by volume. In the second method used, the diameters of 100 nanoparticles were measured from TEM images. This method was time-consuming. After measuring the diameters, the data was represented in the form of a histogram in order

to analyze the size distribution. Mean diameter of the nanoparticle was calculated from 100 measured diameters. Finally, in order to observe the pattern and compare both the measuring techniques, the histogram from TEM image analysis was plotted along with size distribution curve obtained from SAXS measurement. The samples for SAXS were prepared several hours after ablation while TEM samples were prepared from freshly ablated suspensions. In order to know the crystallite size, peak analysis was performed on the peaks in the XRD pattern by using Panalytical HighScore Plus software (version 3.0.5) which uses line profile analysis algorithm based on the Scherrer equation for determination of crystallite size.

Results and Discussion

The process of PLAL can be divided into five stages: (i) irradiation of target with pulsed laser to form plasma, (ii) relaxation of plasma and formation of a cavitation bubble, (iii) nucleation and growth of nanoparticle in the cavitation bubble, (iv) collapse of the cavitation bubble to release nanoparticles in surrounding liquid, and (v) irradiation of synthesized nanoparticles by laser pulses. With PLAL, the nanoparticles are formed by two distinct ablation phenomena, one is with the jet-shaped shadow that ejects solid fragments and droplets from the surface and the second is the formation and growth of nanoparticles from ejected target atoms inside the cavitation bubble [19]. With a microsecond laser pulses, the material removal from the target surface is predominantly by vaporization and boiling while with nanosecond and picosecond laser pulses, there is a coexistence of both direct photoionization and thermal ablation mechanisms, such as vaporization and boiling [20]. The generation and growth of nanoparticles occurs inside the cavitation bubbles, where the ejected atoms, clusters, and droplets collide and aggregate to form nanoparticles [19, 21]. This is followed by a collapse of the cavitation bubble to release the nanoparticles into the surrounding liquid [21]. This collapse of the cavitation bubble occurred, for instance, 610 μ s after irradiation in a study by Lazic et al. when they used a 9.5 ns, 1064 nm Nd:YAG laser [22].

Titanium is chemically active and reacts strongly with the vapors of surrounding liquid resulting in formation of titanium compounds, and in this regard, PLAL is a chemical bottom-up process. During PLAL, the surface titanium atoms are removed when the laser fluence is more than the ablation threshold of titanium. The removed material forms a plasma plume. The optical breakdown of the target occurs due to irradiation by laser pulse to form plasma directly from solid [8]. The cavitation bubbles formed as a result of expansion of plasma consist of not only ablated species from the target but also solvent molecules. Lam et al. studied the

bubble expansion following PLAL and reported the presence of mostly solvent molecules in the cavitation bubble [23]. The extreme conditions of the plasma plume and cavitation bubbles provide a thermodynamic window in which metastable phases can also be formed along with the stable phases; however, phase transformation is possible as the process proceeds. For PLAL in DIW, the formation of hydrated products is possible when unusual focusing configurations are used, such as when the target is not at focus but just under focus so that the laser causes breakdown of water just above it [14]. However, in our experiments, the laser was focused on the target surface. Other phases can form also, but as mentioned earlier, further transformations can happen as the process continues. The ablation of titanium target dipped under 5-mm deionized water was observed to begin at a laser fluence of ~ 13.85 J/cm².

The experiments were conducted with the pulsed laser at 25-kHz repetition rate, which means the delay between two laser pulses was 40 μ s. This is much shorter than the time duration of a cavitation bubble which is usually ~ 300 – 680 μ s depending on laser parameters and solvent properties. This results in strong screening of the laser for every pulse after the first pulse. The fully expanded cavitation bubble acts as a negative lens and strongly defocusses the incident laser beam, thereby reducing the laser fluence at the target surface. This strong defocusing of subsequent laser pulses by bubble formed by previous pulse causes screening of laser pulses and results in irregular ablation by the successive pulses [22]. With the laser and scanning parameters used (25 kHz repetition rate, 500 ns pulse duration, 2000 mm/s scanning speed, and 8×8 mm scanning area), the distance between two laser pulses on the target surface was 80 μ m. This is smaller than the spot size of the laser, especially after the defocusing caused by cavitation bubbles. Due to this, re-ablation on the same spot occurs which raises the temperature of the plasma formed by previous laser pulse. Moreover, in PLAL using a nanosecond laser, there is a temporal overlap between the laser pulses and the ablated material. The plasma plume

formed by the laser pulse absorbs part of the energy from the subsequent laser pulse and results in optical shielding of the target from the laser pulses [14]. This also increases the temperature of the plasma plume and decreases in the energy absorbed by the target surface. As the PLAL process continues, more and more nanoparticles are released in the surrounding solvent which interact with the incident laser pulses and absorb its energy. The laser beam in the experiments is focused at the target, so the synthesized nanoparticles undergo laser processing without laser beam focusing on them. For this configuration with a nanosecond laser, Pyantenko et al. reported that the nanoparticles get intensely heated by the energy absorbed from the laser pulses and can evaporate or explode to form smaller fragments, thereby causing size reduction [24]. Werner et al. concluded that the photothermal mechanism alone (without Coulomb explosion) can explain this pulsed laser-induced size reduction of nanoparticles with nanosecond pulsed laser [25].

Characterization of Nanoparticles by TEM and XRD

The synthesized suspensions were found to contain spherical nanoparticles when analyzed with TEM. In Fig. 2a–c, the TEM images show the nanoparticles synthesized at 20 % LP, 40 % LP, and 50 % LP were all almost perfectly round. The nanoparticles assume spherical shape in order to minimize the interfacial energy. The nuclei consisting of cluster of atoms coalesce with other nuclei to form polycrystalline nanoparticles [14]. The presence of almost perfectly round nanoparticles implies that when nuclei coalesce, either they are melted or their temperature is high enough to ensure the mobility of surface atoms [20]. However, the aggregate of nanoparticles can also undergo melting, fusing, and merging to form larger spherical nanoparticles if the laser fluence is high enough [24]. The nanoparticle suspension synthesized by 20 % LP, Fig. 2a, consisted of nanoparticles whose diameters varied from ~ 4 to ~ 35 nm with about 80 % of the nanoparticles less than 14 nm in diameter.

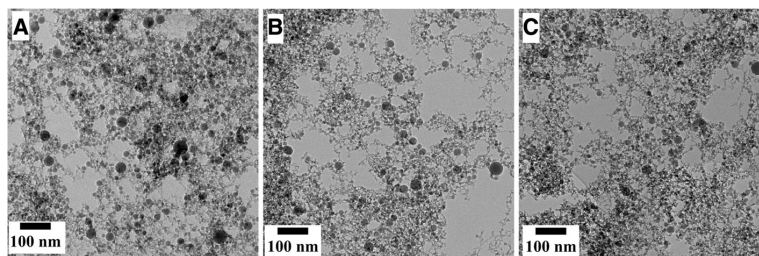
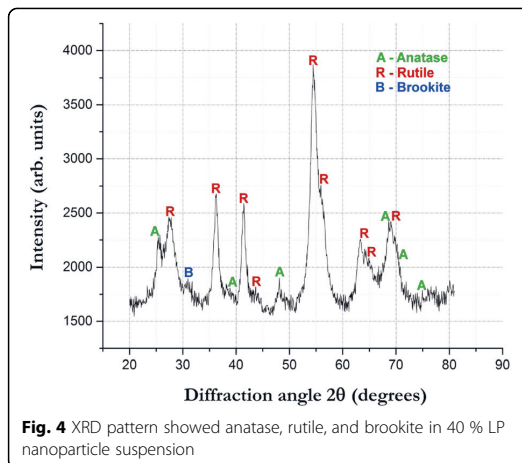


Fig. 2 TEM images show round nanoparticles synthesized at (a) 20 %, (b) 40 %, and (c) 50 % LP

The TEM images in Fig. 3 show web-like structure of nanoparticles synthesized at (a) 20 % LP, (b) 40 % LP, and (c) 50 % LP. At this contrast, the particles can be easily distinguished. Ledoux et al. also reported this web-like structure of nanoparticles formed as a result of PLAL [26]. Also, evident from Fig. 3 is the decrease in size of particles from panel a to b to finally c. The scale bar is 20 nm, and the dimension of scale bars in each image is the same. Another important observation from Fig. 3 is the presence of mostly small nanoparticles; however, relatively larger nanoparticles were also present. This indicates a bimodal size distribution for the synthesized nanoparticles. Such bimodal size distributions of nanoparticles produced by PLAL were also reported by Meunier and Meneghetti [14, 27]. Further analysis of these two observations, (i) decrease in mean size and (ii) size distribution, is covered in the “Particle size analysis” section.

Electron diffraction patterns from TEM samples of all three suspensions indicated mainly crystalline particles which agrees with XRD results (Fig. 4) as high and sharp peaks were visible in XRD pattern indicating high crystallinity. Phase identification with XRD showed that the particles synthesized by PLAL of titanium were TiO₂ nanoparticles. They were present in the form of multiphase titania, consisting of photoactive allotropes, mostly anatase and rutile. Due to small size of particles, broadening of the peaks occurred. The most important peaks for anatase ($2\theta = 25.4$), and rutile ($2\theta = 27.4$), were detected along with many other peaks corresponding to them in the XRD pattern as shown in Fig. 4. The small peak at $2\theta = 30.8$, which is the highest intensity peak for brookite, indicated its presence. As the peak is quite weak, it signifies presence of extremely small amount of brookite. Rutile was the major phase of the nanoparticles while anatase and, in particular, brookite were the minor phases. These X-ray diffraction patterns were very similar for all three suspensions, and the ratio of TiO₂ phases was also the same indicating that the amount of titania phases synthesized does not vary with the change in laser power for the laser and scanning parameters



used. In addition, as anticipated, there were no titanium peaks in the pattern which signifies that all the atoms and clusters of titanium, ablated or droplets ejected from the target, interacted with the solution species. This is understandable considering titanium is chemically active metal, and unlike noble metals, it should not form pure metal nanoparticles.

Particle Size Analysis

Manual measurement of the nanoparticle size from the TEM images gives a number distribution. It is a time-consuming method, and the total number of particles examined is a very small fraction of the total number of nanoparticles. So, it can be argued whether the TEM sample is representative of the bulk of the suspension. In contrast, SAXS gives volume size distribution and corresponding mean diameter by measurements from much more nanoparticles compared to TEM. The SAXS measurement follows a parametric distribution model method. In this distribution model method, the particle shape is assumed to be the same, spherical in this case, while the size of the particle varies [15].

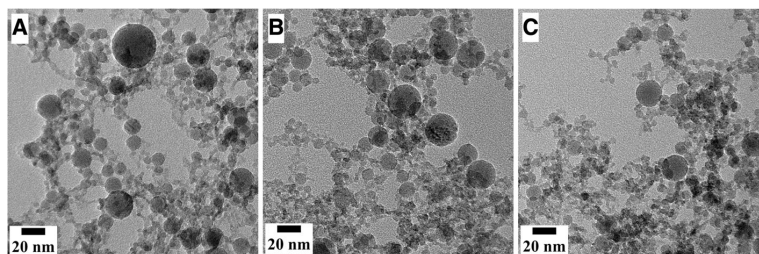
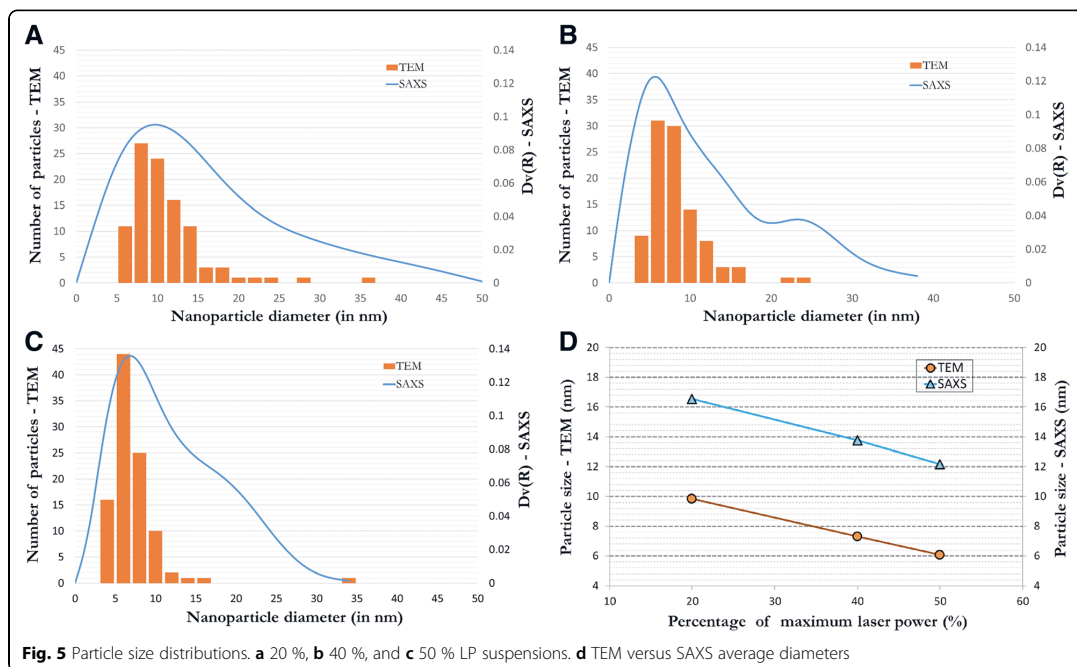


Fig. 3 TEM images show nanoparticles forming web-like structure (a) 20 %, (b) 40 %, and (c) 50 % LP suspensions

In order to compare the two techniques, TEM and SAXS, the size distributions were plotted on the same plot. Figure 5a–c shows the histogram of nanoparticle diameter versus the number of particles on the left y-axis, which was determined from TEM images manually, along with $Dv(R)$ from SAXS on the right y-axis versus the same nanoparticle diameter on the x-axis. The particle size distribution information from the histograms (obtained from TEM) is appropriately represented by the size distribution curve (bimodal size distribution obtained from SAXS). In each case, the curve seems to be following the histogram very well. In Fig. 5a, the size distribution curve and histogram follow each other well. The histogram shows the maxima at 8–10-nm nanoparticle diameter which is extremely close to the maxima of SAXS-measured size distribution curve at 10-nm nanoparticle diameter. This is followed by a drop in the number of nanoparticles for both measurements as the nanoparticle diameter increases. In Fig. 5b, the maximum of the size distribution curve lies yet again extremely close to the maxima of histogram. The histogram and size distribution curve both show the presence of increased number of nanoparticles with diameter 22–24 nm after a minimum at around 19-nm diameter. In Fig. 5c, the maxima of both histogram and size distribution coincide at around 6-nm nanoparticle diameter. Another important observation was the size distribution, determined by both techniques, became narrower with the increase in the

laser power from 20 to 40 % to finally 50 %. This is due to photothermal melting-evaporation and explosive fragmentation of larger nanoparticles to form smaller nanoparticles which narrowed the size distribution [24, 25]. These mechanisms for interaction between laser pulses and target materials change if the pulse duration of the laser is shortened, such as in femtosecond and picosecond lasers, the mechanism changes to Coulomb explosion. Werner et al. have established a thermodynamic model to interpret the effect of laser parameters on the size reduction mechanisms for nanoparticles [25]. The results from both techniques, SAXS and TEM, are consistent with each other for the measurement of TiO_2 nanoparticle size distribution.

The mean nanoparticle diameters showed in Fig. 5a–c were 9.84, 7.31, and 6.06 nm, respectively, from TEM images, while for the same samples analyzed by SAXS measurement, the mean nanoparticle diameters were 16.54, 13.76, and 12.16 nm, respectively. The measured mean nanoparticle diameters in SAXS technique and from analysis of TEM images varied from each other for the same samples. The nanoparticle diameters measured by TEM image analysis were smaller compared to the respective nanoparticle diameters measured by SAXS measurement. The crystallite sizes were measured from XRD pattern of the dried 40 % LP suspension (Fig. 4). The Scherrer results from XRD pattern using Panalytical's HighScore Plus software (version 3.0.5) showed that



crystallite sizes were in the range 3.9 to 13.3 nm with a mean crystallite size of 8.01 nm. For the same sample, the mean diameter of TiO₂ nanoparticle measured by TEM and SAXS was 7.31 and 13.76 nm. The TEM-measured particle size was in agreement with the crystallite sizes measured by XRD. However, the SAXS-measured nanoparticle diameters were slightly higher than TEM-measured diameters for each sample. There are some important reasons for this slight deviation from TEM-measured nanoparticle diameters.

Firstly, while TEM image analysis gives a number size distribution, the SAXS measurement gives volume size distribution. So, in SAXS measurement, the mean volume of sphere is measured which is then converted into the corresponding mean diameter of nanoparticle. Thus, the principle of determination of mean diameter for both measurement techniques is different. This can be explained by assuming three spherical nanoparticles with diameters 2, 6, and 10 nm. According to TEM image analysis with a number distribution, the mean particle diameter is 6 nm while with SAXS measurement, which is volume distribution, the mean particle diameter is 7.42 nm (the three spherical nanoparticles with diameters 2, 6, and 10 nm correspond to volumes of 4.18, 113.04, and 523.33 nm³, respectively. This gives an average volume of 213.52 nm³, from which the SAXS-deduced average diameter is 7.42 nm).

Secondly, it is well known that in XRD, the diffraction occurs at the periphery of the crystallite (for bulk samples) and through the volume (for thin samples such as nanoparticles) while in X-ray scattering, elastic scattering of the X-rays occurs at the phase boundary. Due to this, while measuring with SAXS, several primary particles that are joint in the form of an agglomerate cannot be distinguished, and therefore, we obtain the size of agglomerate and not the primary particle. Due to this, SAXS measures an agglomerate as one big particle which gives a higher volume and consequently increases the mean nanoparticle diameter in the volume size distribution measurement. However, with TEM, we can see and distinguish the agglomerates from primary particles. The measured mean diameter from SAXS, 13.76 nm, is still very close to the mean particle size measured by TEM, which indicates that most particles were present as primary particles along with the presence of a small number of agglomerates containing few particles. Furthermore, from the SAXS measurement of the same sample, the most frequent diameter of the nanoparticles in 40 % LP suspension (Fig. 5b) was 7 nm. This is in agreement with the aforementioned hypothesis regarding presence of mostly primary particles along with a small number of agglomerates. This is also consistent with the TEM- and XRD-measured sizes, 7.31 and 8.01 nm, respectively. In addition, this is evident also

from the Fig. 5b showing TEM histogram and SAXS-measured size distribution, both of which have maxima at the same particle size. Furthermore, if we see the trend of change in mean nanoparticle diameter from Fig. 5d, it is exactly the same for both measurement techniques indicating good agreement between the results from both techniques. The similarities in the plotted curves and the trend evidence the universality of the established SAXS measurement technique for the particle size and size distribution analysis of TiO₂ nanoparticles.

Finally, it is important to mention that the SAXS was sensitive to the concentration of the nanoparticle suspension. In several samples, the absorption factor was not in the range 1.5–5. According to Panalytical's guidelines for EasySAXS software, the results are then not reliable. Absorption factor less than 1.5 indicated that concentration of particles was so low that there was no conclusive difference between the nanoparticles and the background in SAXS measurement. For the same reasons, the suspensions with low particle concentration rendered so few amount of powder that it was not XRD detectable. With such small amounts of nanoparticle powders, specific surface area analysis by gas adsorption (BET) was also out of question. All these samples were obtained as a result of 30 min of ablation time. In order to increase the concentration, the ablation time can be increased. However, this was a batch process, and higher ablation times lead to increased laser processing of the already synthesized nanoparticles and result in stability issues with the suspension as the temperature of the liquid rises. Lam et al. limited the irradiation time to 20 min in order to keep the thermodynamic conditions stable throughout the experiment [28]. Although we propose SAXS for size and size distribution measurement of these nanoparticles, we still propose the use of TEM for determination of shape and appearance of nanoparticles, as we do not obtain this information from SAXS.

Conclusions

Pulsed laser ablation in deionized water was demonstrated to be a promising method to synthesize TiO₂ nanoparticles from titanium target. With 500-ns laser at 25 kHz scanning an area of 8 × 8 mm at a speed of 2000 mm/s, we determined that there was (i) temporal overlap between the laser pulses and the ablated material, (ii) strong screening of laser pulses by cavitation bubbles, and (iii) re-ablation. TEM results showed that the nanoparticles synthesized were spherical in shape, ranging in size from 4 to 35 nm with 80 % of them with diameters smaller than 14 nm for the suspension synthesized at 20 % laser power. XRD results indicated that the nanoparticles constituted mainly two allotropes of titania: anatase and rutile. The weak peak for

brookite indicated its presence as a minor phase. Rutile was found to be the major phase of the synthesized nanoparticles.

For size distribution measurement of these nanoparticles, SAXS was introduced and evaluated with promising results. The SAXS-measured particle size distribution measurements were consistent with TEM. Both showed that the size distribution of nanoparticles became narrower with the increase in laser power from 20 to 40 % to finally 50 % while at the same time, the nanoparticles also became finer. This was attributed to explosive fragmentation of larger nanoparticles to form smaller nanoparticles and photothermal melting-evaporation of all nanoparticles during irradiation. Due to the difference in measurement type and sensitivity towards agglomerates, SAXS-measured diameters were slightly higher than TEM-measured diameters. However, the trend in the variation in the mean nanoparticle size with laser power determined for 20 % LP, 40 % LP, and 50 % LP suspensions by both techniques, SAXS and TEM, was exactly the same, which fortifies the discussion and the consistency in the results from both techniques. Based on the well-founded discussion, the SAXS-measured nanoparticle size and size distribution results are evidently propitious, noble, and promising. We propose SAXS as a promising method to measure particle size and size distribution of PLAL-synthesized TiO₂ nanoparticles. However, in order to obtain comprehensive information on the shape and appearance of nanoparticles, we propose using TEM.

Abbreviations

AFM: Atomic force microscopy; DLS: Dynamic light scattering; DMA: Differential mobility analysis; D_v(R): Distribution volume ratio; LP: Laser power; PLAL: Pulsed laser ablation in liquids; SAXS: Small angle X-ray scattering; SEM: Scanning electron microscopy; TEM: Transmission electron microscopy; XRD: X-ray diffraction

Authors' Contributions

AS is the corresponding author who was predominantly responsible for researching the background of this study, planning the experiments, and writing the manuscript. JV provided the pulsed laser, laser scanner, and training of its usage to AS. LH performed the XRD and SAXS measurements. MH was responsible for TEM imaging and ED pattern analysis. EF and EL supervised this work and contributed to the valuable discussions. All authors have read and approved the final manuscript.

Competing Interests

The authors declare that they have no competing interests.

Author details

¹Department of Materials Science, Tampere University of Technology, P. O. Box 589, FIN 33101 Tampere, Finland. ²Department of Mechanical Engineering and Industrial Systems, Tampere University of Technology, P. O. Box 589, FIN 33101 Tampere, Finland.

Received: 10 June 2016 Accepted: 31 August 2016

Published online: 05 October 2016

References

- Zurutuza A, Marinelli C (2014) Challenges and opportunities in graphene commercialization. *Nat Nanotechnol* 9:730–734. doi:10.1038/nnano.2014.225

- Ogale SB, Malshe AP, Kanetkar SM, Kshirsagar ST (1992) Formation of diamond particulates by pulsed ruby laser irradiation of graphite immersed in benzene. *Solid State Commun* 84:371–373. doi:10.1016/0038-1098(92)90479-5
- Sasaki T, Shimizu Y, Koshizaki N (2006) Preparation of metal oxide-based nanomaterials using nanosecond pulsed laser ablation in liquids. *J Photochem Photobiol A Chem* 182:335–341. doi:10.1016/j.jphotochem.2006.05.031
- Urabe K, Kato T, Stauss S et al (2013) Dynamics of pulsed laser ablation in high-density carbon dioxide including supercritical fluid state. *J Appl Phys* 114:143303. doi:10.1063/1.4824538
- Machmudah S, Takada N, Kanda H et al (2013) Fabrication of gold and silver nanoparticles with pulsed laser ablation under pressurized CO₂. *Adv Nat Sci Nanosci Nanotechnol* 4:045011. doi:10.1088/2043-6262/4/4/045011
- Saitow K, Yamamura T, Minami T (2008) Gold nanospheres and nanonecklaces generated by laser ablation in supercritical fluid. *J Phys Chem C* 112:18340–18349
- Machmudah S, Kuwahara Y, Sasaki M, Goto M (2011) Nano-structured particles production using pulsed laser ablation of gold plate in supercritical CO₂. *J Supercrit Fluids* 60:63–68. doi:10.1016/j.supflu.2011.04.008
- Yan Z, Chrisey DB (2012) Pulsed laser ablation in liquid for micro-/nanostructure generation. *J Photochem Photobiol C: Photochem Rev* 13: 204–223. doi:10.1016/j.jphotochemrev.2012.04.004
- Dolgaev S, Simak A, Voronov V (2002) Nanoparticles produced by laser ablation of solids in liquid environment. *Appl Surf Sci* 186:546–551
- Semaltianos NG, Logothetidis S, Frangis N et al (2010) Laser ablation in water: a route to synthesize nanoparticles of titanium monoxide. *Chem Phys Lett* 496:113–116. doi:10.1016/j.cplett.2010.07.023
- Yang L, May PW, Yin L et al (2007) Growth of diamond nanocrystals by pulsed laser ablation of graphite in liquid. *Diam Relat Mater* 16:725–729. doi:10.1016/j.diamond.2006.11.010
- Petersen S, Barcikowski S (2009) In situ bioconjugation: single step approach to tailored nanoparticle-bioconjugates by ultrashort pulsed laser ablation. *Adv Funct Mater* 19:1167–1172. doi:10.1002/adfm.200801526
- Qian W, Murakami M, Ichikawa Y, Che Y (2011) Highly efficient and controllable PEGylation of gold nanoparticles prepared by femtosecond laser ablation in water. *J Phys Chem C* 115:23293–23298. doi:10.1021/jp2079567
- Amendola V, Meneghetti M (2009) Laser ablation synthesis in solution and size manipulation of noble metal nanoparticles. *Phys Chem Chem Phys* 11: 3805–3821. doi:10.1039/b900654k
- Agbabiaka A, Wiltfong M, Park C (2013) Small angle X-ray scattering technique for the particle size distribution of nonporous nanoparticles. *J Nanoparticles* 2013:11. doi: http://dx.doi.org/10.1155/2013/640436
- Sasaki A (2005) Size distribution analysis of nanoparticles using small angle X-ray scattering technique. *Rigaku J* 22:31–38
- Vippola M, Valkonen M, Sarlin E et al (2016) Insight to nanoparticle size analysis—novel and convenient image analysis method versus conventional techniques. *Nanoscale Res Lett* 11:169. doi:10.1186/s11671-016-1391-z
- Vlădoiu I, Stafe M, Neagu C, Popescu IM (2008) Nanopulsed ablation rate of metals dependence on the laser fluence and wavelength in atmospheric air. *UPB Sci Bull Ser A Appl Math Phys* 70:119–126
- Tsuji T, Okazaki Y, Tsuboi Y, Tsuji M (2007) Nanosecond time-resolved observations of laser ablation of silver in water. *Jpn J Appl Phys* 46:1533–1535. doi:10.1143/JJAP.46.1533
- Amendola V, Meneghetti M (2013) What controls the composition and the structure of nanomaterials generated by laser ablation in liquid solution? *Phys Chem Chem Phys* 15:3027–3046. doi:10.1039/C2CP42895D
- Soliman W, Takada N, Sasaki K (2010) Growth processes of nanoparticles in liquid-phase laser ablation studied by laser-light scattering. *Appl Phys Express* 3:035201. doi:10.1143/APEX.3.035201
- Lazic V, Jovicevic S, Carpanese M (2012) Laser induced bubbles inside liquids: transient optical properties and effects on a beam propagation. *Appl Phys Lett* 101:054101. doi:10.1063/1.4739851
- Lam J, Lombard J, Dujardin C et al (2016) Dynamical study of bubble expansion following laser ablation in liquids. *Appl Phys Lett* 108:074104. doi:10.1063/1.4942389
- Pyatenko A, Wang H, Koshizaki N, Tsuji T (2013) Mechanism of pulse laser interaction with colloidal nanoparticles. *Laser Photon Rev* 7:596–604. doi:10.1002/lpor.201300013
- Werner D, Hashimoto S (2011) Improved working model for interpreting the excitation wavelength- and fluence-dependent response in pulsed laser-induced size reduction of aqueous gold nanoparticles. *J Phys Chem C* 115: 5063–5072. doi:10.1021/jp109255g

26. Ledoux G, Amans D, Dujardin C, Masenelli-Varlot K (2009) Facile and rapid synthesis of highly luminescent nanoparticles via pulsed laser ablation in liquid. *Nanotechnology* 20:445605. doi:10.1088/0957-4484/20/44/445605
27. Kabashin AV, Meunier M (2003) Synthesis of colloidal nanoparticles during femtosecond laser ablation of gold in water. *J Appl Phys* 94:7941. doi:10.1063/1.1626793
28. Lam J, Amans D, Chaput F et al (2014) γ -Al₂O₃ nanoparticles synthesised by pulsed laser ablation in liquids: a plasma analysis. *Phys Chem Chem Phys* 16:963–973. doi:10.1039/C3CP53748J

Submit your manuscript to a SpringerOpen[®] journal and benefit from:

- Convenient online submission
- Rigorous peer review
- Immediate publication on acceptance
- Open access: articles freely available online
- High visibility within the field
- Retaining the copyright to your article

Submit your next manuscript at ► springeropen.com

PUBLICATION

II

Effect of laser power on yield of TiO₂ nanoparticles synthesized by pulsed laser ablation in water

A. Singh, J. Vihinen, E. Frankberg, L. Hyvärinen, M. Honkanen, and E. Levänen

Journal of Ceramic Science and Technology, Vol. 8, pp. 39–44

[https://doi.org/ 10.4416/JCST2016-00071](https://doi.org/10.4416/JCST2016-00071)

Publication reprinted with the permission of the copyright holders.

Effect of Laser Power on Yield of TiO₂ Nanoparticles Synthesized by Pulsed Laser Ablation in Water

A. Singh^{*1}, J. Vihinen², E. Frankberg¹, L. Hyvärinen¹, M. Honkanen¹, E. Levänen¹

¹Department of Materials Science, Tampere University of Technology, P. O. Box 589, FIN 33101 Tampere, Finland

²Department of Mechanical Engineering and Industrial Systems, Tampere University of Technology, P. O. Box 589, FIN 33101 Tampere, Finland

received September 19, 2016; received in revised form November 15, 2016; accepted December 9, 2016

Abstract

In this study, the pulsed laser ablation in liquids (PLAL) technique was used on titanium in deionized water at different laser powers to understand its effect on the synthesis yield of nanoparticles. A 500-ns 1062-nm fiber laser at 25 kHz was used to effect PLAL of titanium to produce nanoparticles. TEM images of the synthesized nanoparticles showed spherical particles ranging from 3–32 nm in diameter. The electron diffraction pattern and high peaks in the wide-angle x-ray scattering (WAXS) pattern indicated high crystallinity of nanoparticles. WAXS results showed nanoparticles were allotropes of titania: rutile and anatase. Synthesis yield measurements indicated an increase in yield with the increase in laser power as long as the increase in laser fluence remains proportional to the increase in laser power. However, the yield increased proportionally with the increase in laser fluence. The analysis of the chosen laser pulse duration and repetition rate showed an increase in the yield with longer pulse duration and higher repetition rate.

Keywords: Nanoparticles, synthesis yield, pulsed laser ablation in liquids, WAXS, laser fluence

I. Introduction

Synthesis and use of nanoparticles accounts for a large part of the burgeoning nanoparticle industry in the world. Photoactive TiO₂ nanoparticles have several applications such as water purification, self-cleaning, anti-bacterial, and anti-fogging^{1,2}. The use of pulsed laser ablation in liquids (PLAL) has been well reported by many researchers for the synthesis of nanoparticles of metals and metal oxides^{3–6}. PLAL has been reported as a green method for the production of nanomaterials with reproducible results and it costs about €20k for the experimental equipment including the laser⁷. In PLAL, a pulsed laser irradiates a target that is dipped in a solvent to produce nanoparticles. The optical breakdown of the water by the pulsed laser leads to the formation of cavitation bubbles, inside which the generation and growth of nanoparticles occur^{8,9}. Upon the collapse of the cavitation bubble, these nanoparticles are released into the surrounding liquid to form a nanoparticle suspension⁹. The synthesis parameters are classified into two groups: laser parameters (such as laser power, fluence, duration, wavelength and repetition rate) and material parameters (such as target material, solvent, temperature and pressure of the system)¹⁰.

Due to the lack of universally defined procedures for PLAL¹⁰, and availability of numerous laser and material

parameters, there are no conclusive results on the effect of laser parameters, such as laser power and laser fluence, on the synthesis yield of TiO₂ nanoparticles. This study aims to fill this research gap by experimental investigation of the variation in synthesis yield of nanoparticles. In this study, we determined how the laser parameters – laser power and laser fluence – affect the synthesis yield of TiO₂ nanoparticles.

II. Materials and Methods

A suspension of nanoparticles was obtained via irradiation of titanium metal plate (99.99 % pure, Goodfellow Cambridge Ltd) by 85W 500-nanosecond fiber laser at 1062 nm output using a XY scanner. The laser was an SPI 85 Watt fiber laser obtained from SPI Lasers Limited with the model name SPI SP-085-W-HS-M-B-Y(02). The beam quality factor or beam propagation factor M² was 3.7. The laser was controlled by SPI's software G4 Laser control (version 4.0). The scanner was a GSI HB X-10 with an aperture of 10 mm and consisted of two mirrors. The optics consisted of a Linos f-theta Ronar objective lens with 160 mm focal length obtained from LINOS photonics. The scanner was controlled by SCAPS software SAM-Light (version 3.0.5) from SCAPS GmbH. The laser beam was focused on the titanium target by the f-theta lens on a predetermined area 8 mm x 8 mm on the titanium target. The pulse duration was 500 ns and repetition rate was 25 kHz. The maximum pulse energy of the laser was 3.4 mJ

* Corresponding author: amandeep.singh@tut.fi

per pulse and was available at 500-nanosecond pulse duration, which is the time for which the laser pulse irradiates the target. The maximum laser fluence of the laser was 58.92 J/cm^2 . The scanning speed was 2000 mm/s for each experiment. The collimated laser beam diameter was 8.5 mm provided by the manufacturer of the laser SPI Lasers Ltd. At this speed, the scanner took 2.566 seconds to complete one loop on an area of $8 \text{ mm} \times 8 \text{ mm}$. Each experiment consisted of 720 loops, which corresponds to an ablation time of 30 minutes. During irradiation of the titanium target, the plasma plume formed as a result of ablation, was clearly visible with the naked eye. A visible blue coloration of DIW was observed after about 20 loops due to laser ablation of titanium resulting in the removal of material from target to the surrounding liquid DIW.

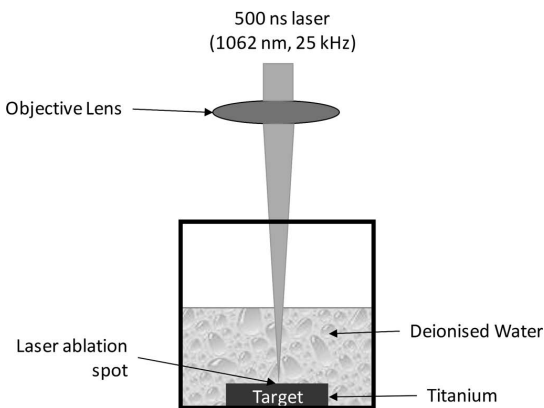


Fig. 1: Schematic of pulsed laser ablation of titanium in deionized water.

PLAL of titanium plate was performed in deionized water (DIW) with laser powers 12% , 15% , 18% , 20% , 30% , 40% , and 50% of the maximum laser power. The titanium targets, $15 \text{ mm} \times 15 \text{ mm}$, were completely identical for ablation experiments at each chosen laser power. The thickness of DIW film above titanium target was 5 mm . As the ablation was performed in water, the focusing of the laser depended not only on the target position relative to the focusing lens but also on the thickness of the water film on top of target. Due to higher refractive index of water (1.33) compared to air (1.00), the 5-mm -thick layer of DIW above the target shifts the focal plane as a result of optical refraction in water. So, the laser must be focused on the target only after adjusting the water film thickness, which in this case was 5 mm . In all the experiments, the target-objective lens distance and thickness of water film was the same in order to have identical focusing conditions. The ablation time was also the same, 30 minutes, in each case to synthesize nanoparticle suspensions. The laser beam was incident at an angle of 90° relative to the target surface plane to effect ablation (as shown in Fig. 1). The vessel containing the titanium target dipped in DIW was placed on a horizontal platform and the irradiation was performed from the top at an angle of 90° as mentioned earlier. All laser and scanning parameters were exactly same for all samples and the only variable parameter was the laser power which was used for controlling the

laser fluence. The pulse energy and laser output varied linearly with each other. The correlation was determined experimentally using a FieldMaxII-TOP energy meter and PM300F-50 sensor from Coherent Inc. (USA). Therefore, the term laser power is synonymous with pulse energy, and so this manuscript can also be interpreted as the “Effect of the laser pulse energy on the yield of TiO_2 nanoparticles synthesized by pulsed laser ablation.” The spot diameters were measured for different laser powers by ablating the target in air medium at normal atmosphere pressure and room temperature and measuring the diameter of the ablated crater from the optical microscopy images. The parameters used for the laser and scanner were 500 ns pulse duration, 25 kHz repetition rate, 2000 mm/s scanning speed. As mentioned earlier, the beam quality factor M^2 was 3.7 , which for an ideal laser should be 1 . Due to this, the spot diameter varied with the variation in laser power.

The samples for measuring the synthesis yield were prepared from these synthesized suspensions. Small LDPE bottles, ordered from VWR International Limited, were used for storing the synthesized nanoparticle suspensions. 10 ml of each suspension type was then pipetted to the respective vial and dried in a heat cabin at a constant temperature of 120°C to obtain the nanoparticle powder. These dried powders were then weighed to measure the yield of nanoparticles for varying laser powers. Since the ablation time in each case was 30 minutes, the mass of nanoparticles produced is proportional to the productivity of nanoparticles for each value of laser power.

The obtained suspensions were characterized by means of transmission electron microscopy (TEM) and wide-angle x-ray scattering (WAXS). TEM images of the nanoparticles were taken using a Jeol JEM-2010 microscope. Imaging in each case was performed at 200 kV acceleration voltage. TEM samples were prepared from droplets of the synthesized suspensions dried out on carbon-coated copper grids. A Panalytical Empyrean Multipurpose Diffractometer with anode material copper using $\text{CuK}\alpha$ radiation ($\lambda = 0.15418 \text{ nm}$) was used for WAXS measurements. It was powered by an x-ray generator at 45 kV and 40 mA . It consisted of a solid-state pixel detector, PIXcel3D, which measured the scattered intensities as a function of the scattering angle (2θ). To prepare the WAXS sample, an equal volume of each suspension was enclosed between two Mylar foils which were x-ray transparent. They were then placed between the respective circular transmission holders for each sample. The background sample was DIW enclosed between two Mylar foils. The phase identification from WAXS pattern was done with Panalytical HighScore Plus software (version 3.0.5). The scan range was from 5.0° to 54.9° with a 0.026° step size.

III. Results and Discussion

This study used a 1062-nm fiber laser, which is a near-infrared region (NIR) laser. This raises question about the interaction of the 1062-nm fiber laser with water, or precisely how significant is the absorption of the laser light by DIW. Altunoğlu *et al.* reported that the absorption coefficient of water is minimal from a wavelength of 800 nm

and till 1150 nm in NIR¹¹. Due to insignificant absorption, wavelengths between 800 nm and 1000 nm constitute to form the highest optical transmission window, also known as “imaging window” for the laser light in water. The absorption coefficient of water at 1062 nm also lies in this highest optical transmission window in NIR. 1319, 1320 nm, and 1470 nm are some of the specific wavelengths for high absorption coefficient of light by water in NIR¹². Due to this, in our study, there was insignificant absorption of laser light by water. However, the quenching of target, and especially target surface undergoing ablation, resulted in heating of water. The ablation of titanium target in DIW was observed to begin at a laser fluence of 13.85 J/cm². In literature, the ablation threshold of titanium with a 4.5-ns Nd:YAG laser at 10 kHz was reported to be 4.5 J/cm² in air¹³. This implies a threefold increase in the threshold in DIW compared to air. In literature, similar results were reported by Kabashin *et al.*, in which the ablation threshold of gold was found to be five times higher in water compared to vacuum¹⁴. The ablation was caused by the pulsed laser at 25 kHz repetition rate which means that the time interval between two laser pulses was 40 μs. This is several times shorter than the duration of cavitation bubble ~ 600 μs. This suggests that the subsequent laser pulses pass through the cavitation bubble, which acts as a negative lens and leads to defocusing of the laser. In our previous study, we have discussed the photothermal mechanism for nanoparticle formation by pulsed laser ablation in DIW with the same laser and laser parameters as in this study⁶. With a nanosecond laser, the nanoparticles are formed by photothermal mechanisms, such as vaporization and boiling¹⁵. So, with this 500-ns laser, we can exclude “Coulomb explosion” as a nanoparticles formation mechanism.

Fig. 2 shows TEM images of nanoparticles synthesized by laser ablation of titanium. The nanoparticles were

spherical in shape and formed a web-like network in which all particles are joined to form a cluster of nanoparticles (Fig. 2b). There are then several individual clusters in the nanoparticles suspensions. The size range of nanoparticles measured from TEM images in Fig. 2 (a) was 3–32 nm with a mean diameter of 8.1 nm. When the nuclei-containing clusters of ablated metal atoms join to form nanoparticles inside the cavitation bubbles, the temperature is high enough to cause melting of these nuclei to form spherical nanoparticles¹⁰. The spherical shape results in minimizing the interfacial energy.

ED pattern analysis and high peaks in the WAXS pattern (Fig. 3) indicated that the nanoparticles synthesized were crystalline. WAXS analysis of nanoparticle suspension synthesized at 20% laser power showed that the nanoparticles were titania (TiO₂) allotropes; rutile and anatase. The highest-intensity peaks detected for rutile and anatase were at scattering angles (2θ) 27.4° and 25.3° respectively. The formation of an oxide of titanium was anticipated since the solvent, DIW, is a source of oxygen. There were no peaks in the pattern for any other titanium compounds or titanium metal. Absence of peaks for titanium is understandable considering its high chemical reactivity, unlike noble metals, such as Au and Ag, that can form pure metal nanoparticles upon ablation in water. The formation of hydrated products has been reported to be favored when using unusual laser focusing configurations, such as when the target is placed below the focus, which causes the breakdown of water⁷. In our study, the laser was focused at the target surface with a f-theta lens within ± 0.01 mm from focus. The absence of other titanium oxides could also be due to phase transformation happening during the laser-induced irradiation of the already-synthesized nanoparticles.

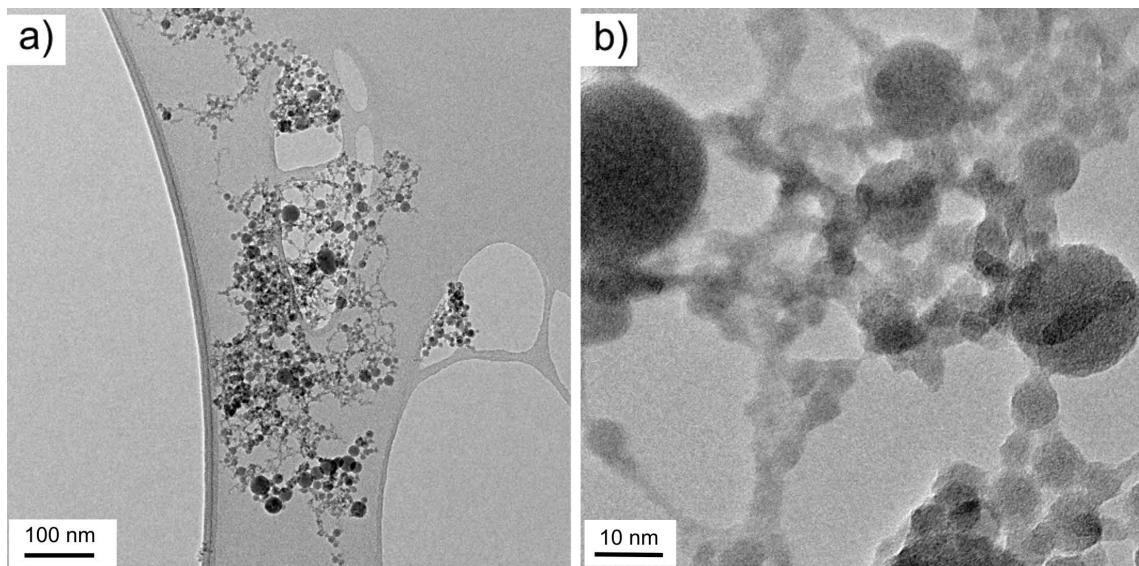


Fig. 2: TEM images show (a) synthesized nanoparticles were spherical with diameters from 3 nm to 32 nm (b) nanoparticles bound in web-like network.

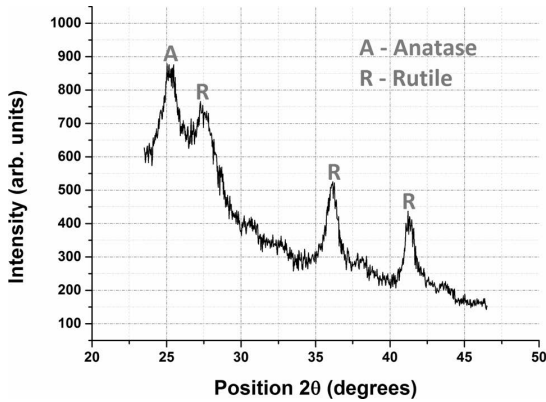


Fig. 3: Wide-angle x-ray scattering pattern shows nanoparticles were rutile and anatase.

The synthesis yield for all the samples was measured according to aforementioned method explained in the experimental section. When plotted against the laser power, the weights of the samples containing nanoparticles followed a trend as shown in Fig. 4. The yield increased from 12 % laser power to 40 % laser power after which it drops at 50 % laser power even though the laser power is increasing.

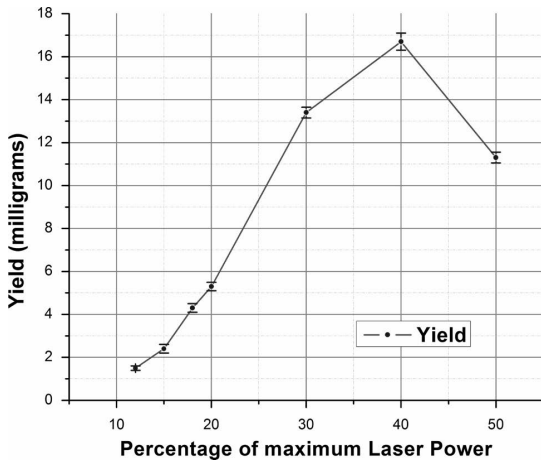


Fig. 4: Graph showing the effect of laser power on synthesis yield of nanoparticles.

To understand this, laser fluence values were determined by measuring spot diameters for the laser beam at different laser powers. Here, laser fluence is defined as the ratio of the laser pulse energy to the laser spot area. The minimum spot diameter was 50 μm and stayed constant till 20 % laser power. However, the spot diameter became larger in value as the laser power was increased from 20 % to finally 100 % of the maximum laser power. Kabashin *et al.* (2003) reported that with the increase in pulse energy, which is synonymous with an increase in laser power, the productivity of nanoparticles increases almost proportionally¹⁴. Keeping the laser fluence the same, higher spot size leads to increased yield of nanoparticles¹⁰. In our study, the spot size of the laser remained unchanged with the increase in laser power from 12 – 20 % laser power, and increased from 50 μm at 20 % laser power to only 54.2 μm

at 40 % laser power. This led to an almost steady increase in the laser fluence with the increase in laser pulse energy (Fig. 5). Due to this, the productivity of the nanoparticles increased almost linearly with the increase in laser power till 40 % laser power (Fig. 4), which is consistent with results reported by Kabashin *et al.* (2003), mentioned earlier. At 50 % laser power, however, the laser spot size increased with the increase in laser power, resulting in decreased laser fluence. This increase in the spot size has been attributed to the high beam quality factor 3.7 as mentioned in the experimental section earlier. So, the energy of the laser pulse at 50 % laser power was focused on a much larger area compared to 40 % laser power. Due to this, at 50 % laser power, we observed a drop in the yield of nanoparticles. The decrease in the yield is because of two competing laser parameters affecting the ablation rate, namely, increase in pulse energy, and decrease in laser fluence. The ablation rate (units $\mu\text{m}/\text{pulse}$) is the layer thickness of material ablated for a given pulse. The ablation rate increases with increase in pulse energy and laser fluence^{13, 14}. At 50 % laser power, compared to 40 % laser power, the competing mechanisms affecting the yield of nanoparticles are (i) reduced ablation rate due to decrease in laser fluence, and (ii) increased ablation due to increased pulse energy leading to higher temperature of plasma causing more ablation by melting and evaporation. However, the increase in laser pulse energy, in this case, was not sufficient to overcome the decrease in laser fluence, and consequently resulted in a decreased yield of nanoparticles. This hypothesis is further supported by comparing the yield at 30 % and 50 % laser power from Fig. 4 in which the yield is higher for 30 % laser power. The laser pulse energy at 30 % and 50 % laser power were 1.02 mJ and 1.70 mJ per pulse respectively. From Fig. 5, the observed laser fluences at 30 % and 50 % laser power were 46.75 J/cm^2 and 41.53 J/cm^2 respectively. The comparison of laser energy and laser fluence at 30 % and 50 % with their corresponding yields indicates that the variation in the yield of nanoparticles follows the variation in the laser fluence. In addition, the variation in the yield of nanoparticles also follows the variation in laser power (and pulse energy) as long as there is insignificant change in the spot diameter, which means a steady increase in laser fluence with the increase in pulse energy. The variation in the spot diameter is a result of high beam quality factor of 3.7. This correlation elucidates the variation of yield with laser power and laser fluence.

The ablation rate increases with higher repetition rate resulting in higher yield because at higher repetition rates up to few tens of kHz, such as 25 kHz in this case, the mean temperature at the laser spot is much higher than room temperature, causing more ablation¹⁰. At low repetition rates, the time interval between the pulses is long enough for the laser spot to cool down to room temperature. This is however, not possible at high repetition rates such as 25 kHz in our experiments, due to which the mean laser spot temperature is higher. In this study, a 500-ns laser was used, which signifies that the pulse duration was 500 ns. This resulted in overlap of laser pulses with the plasma plume causing plasma shielding of the laser pulses and absorption of energy from laser pulses by the plasma plume.

With a nanosecond laser, the laser pulse and ablated material coexist for longer time as compared to a picosecond or femtosecond laser¹⁰. This further increases the temperature, pressure and duration of the plasma plume¹⁰. Due to this, the yield of nanoparticles increases compared to when the laser pulses do not overlap with the plasma plume. This temporal overlapping of subsequent laser pulses on plasma plume improves the homogeneity of the plasma plume, which in turn results in a narrower size distribution compared to ablation with picosecond or femtosecond laser pulses¹⁰. Furthermore, this increased temperature of the plasma plume also raises the temperature of the target which subsequently increases the yield as the plasma heats up the target to cause more ablation by melting and evaporation¹⁴. This analysis signifies that long pulse duration (nanosecond laser) and optimum repetition rate of few tens of kHz leads to an increase in the yield of nanoparticles. The yield in TiO₂ nanoparticles from laser ablation of titanium using laser at visible and UV wavelengths is of interest to the authors for future work.

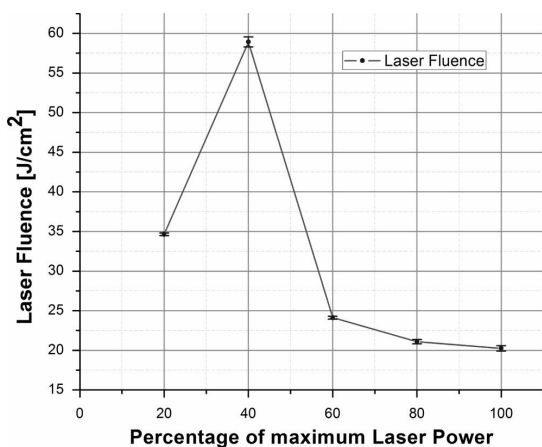


Fig. 5: Graph shows experimentally calculated laser fluence values at different laser powers.

IV. Conclusions

We report the successful synthesis of nanoparticles by PLA of titanium in deionized water at different laser powers and investigated experimentally the variation in the yield of nanoparticles with laser power. TEM results showed spherical nanoparticles 3–32 nm in diameter in the nanoparticle suspensions synthesized, forming a web-like network. ED pattern and WAXS results showed that the nanoparticles were crystalline and consisted of two titania allotropes: rutile and anatase. The yield measurements indicated that the synthesis yield of TiO₂ nanoparticles increases linearly with the increase in laser power (synonymous to pulse energy in this study) as long as the laser fluence increases with laser power. When the laser fluence does not increase proportionally with the increase in laser power, then two competing mechanisms determine the synthesis yield: (i) increased ablation rate due to increased pulse energy, and (ii) decreased ablation due to

reduction in laser fluence. The analysis showed that the yield increases proportionally with the increase in laser fluence. When the beam quality factor M^2 is high, such as 3.7 in our study, the variation of yield of nanoparticles is described more appropriately by laser fluence than by laser power or pulse energy, since a high M^2 value leads to variation in spot size with the increase in pulse energy. The discussion of the chosen laser parameters revealed that with longer pulse duration and higher repetition rate, the yield of nanoparticles increases.

References

- Friedmann, D., Mendive, C., Bahnemann, D.: TiO₂ for water treatment: parameters affecting the kinetics and mechanisms of photocatalysis, *Appl. Catal. B Environ.*, **99**, 398–406, (2010).
- Fujishima, A., Rao, T.N., Tryk, D.: Titanium dioxide photocatalysis, *J. Photochem. Photobiol. C Photochem. Rev.*, **1**, 1–21, (2000).
- Machmudah, S., Takada, N., Kanda, H., Sasaki, K., Goto, M.: Fabrication of gold and silver nanoparticles with pulsed laser ablation under pressurized CO₂, *Adv. Nat. Sci. Nanosci. Nanotechnol.*, **4**, 045011, (2013).
- Saitow, K., Yamamura, T., Minami, T.: Gold nanospheres and nanonecklaces generated by laser ablation in supercritical fluid, *J. Phys. Chem. C*, **112**, 18340–18349, (2008).
- Semaltianos, N.G. et al.: Laser ablation in water: A route to synthesize nanoparticles of titanium monoxide, *Chem. Phys. Lett.*, **496**, 113–116, (2010).
- Singh, A. et al.: Pulsed laser ablation-induced green synthesis of TiO₂ nanoparticles and application of novel small angle X-ray scattering technique for nanoparticle size and size distribution analysis, *Nanoscale Res. Lett.*, **11**, 447, (2016).
- Amendola, V., Meneghetti, M.: Laser ablation synthesis in solution and size manipulation of noble metal nanoparticles, *Phys. Chem. Chem. Phys.*, **11**, 3805–3821, (2009).
- Tsuji, T., Okazaki, Y., Tsuboi, Y., Tsuji, M.: Nanosecond time-resolved observations of laser ablation of silver in water, *Jpn. J. Appl. Phys.*, **46**, 1533–1535, (2007).
- Soliman, W., Takada, N., Sasaki, K.: Growth processes of nanoparticles in liquid-phase laser ablation studied by laser-light scattering, *Appl. Phys. Express*, **3**, 035201, (2010).
- Amendola, V., Meneghetti, M.: What controls the composition and the structure of nanomaterials generated by laser ablation in liquid solution? *Phys. Chem. Chem. Phys.*, **15**, 3027–3046, (2013).
- Altinoğlu, E. İ., Adair, J.H.: Near infrared imaging with nanoparticles. *Wiley Interdiscip. Rev. Nanomedicine Nanobiotechnology*, **2**, 461–477. (2010).
- Yu, D.-Y., Chen, H.-C., Chang, S.-Y., Hsiao, Y.-C., Chang, C.-J.: Comparing the effectiveness of 1064 vs. 810 nm wavelength endovascular laser for chronic venous insufficiency (Varicose Veins), *LASER Ther.*, **22**, 247–253, (2013).
- Vlădoiu, I., Stafe, M., Neguțu, C., Popescu, I.M.: Nanopulsed ablation rate of metals dependence on the laser fluence and wavelength in atmospheric air, *UPB Sci. Bull. Ser. A Appl. Math. Phys.*, **70**, 119–126, (2008).
- Kabashin, A.V., Meunier, M.: Synthesis of colloidal nanoparticles during femtosecond laser ablation of gold in water, *J. Appl. Phys.*, **94**, 7941, (2003).
- Werner, D., Hashimoto, S.: Improved working model for interpreting the excitation wavelength- and fluence-dependent response in pulsed laser-induced size reduction of aqueous gold nanoparticles, *J. Phys. Chem. C*, **115**, 5063–5072, (2011).

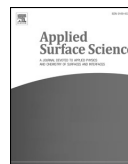
PUBLICATION III

Multiphase Ti_xO_y nanoparticles by pulsed laser ablation of titanium in supercritical CO_2

A. Singh, T. Salminen, M. Honkanen, J. Vihinen, L. Hyvärinen, and E. Levänen

Journal of Applied Surface Science, Vol. 476, pp. 822–827
<https://doi.org/10.1016/j.apsusc.2019.01.172>

Publication reprinted with the permission of the copyright holders.



Full length article

Multiphase Ti_xO_y nanoparticles by pulsed laser ablation of titanium in supercritical CO_2

Amandeep Singh^{a,*}, Turkka Salminen^b, Mari Honkanen^b, Jorma Vihinen^c, Leo Hyvärinen^a, Erkki Levänen^a

^a Materials Science, Faculty of Engineering and Natural Sciences, Tampere University, P. O. Box 589, FIN 33101 Tampere, Finland

^b Tampere Microscopy Center, Tampere University, P. O. Box 692, FIN 33101 Tampere, Finland

^c Faculty of Engineering and Natural Sciences, Tampere University, P. O. Box 589, FIN 33101 Tampere, Finland



ARTICLE INFO

Keywords:

Pulsed laser ablation
Supercritical fluids
Multiphase titanium oxides
Non-stoichiometric compounds
Metastable phases

ABSTRACT

In this paper, we demonstrate pulsed laser ablation (PLA) in supercritical CO_2 (sc CO_2) as a promising method to synthesize multiphase Ti_xO_y nanoparticles from a titanium target. These results are compared against PLA of titanium in H_2O . By means of transmission electron microscopy, we observed spherical-shaped, well-dispersed non-agglomerate crystalline nanoparticles by PLA in sc CO_2 while PLA in H_2O produced spherical-shaped as well as randomly shaped nanoparticles that joined to form web-like networks. Raman spectroscopy and x-ray diffraction showed nanoparticles synthesized in sc CO_2 consisted of anatase- TiO_2 , Ti_2O_3 and $TiO_{0.89}$ while nanoparticles synthesized in H_2O were mainly rutile- TiO_2 , with possibility of presence of brookite- TiO_2 . This indicates PLA in sc CO_2 favours formation of metastable phases (anatase- TiO_2 , Ti_2O_3 and $TiO_{0.89}$) while PLA in H_2O results in mostly stable phase (rutile- TiO_2).

1. Introduction

Titanium dioxide (TiO_2) has been a material of great interest in the scientific community as well as industry after its excellent photocatalytic properties were reported by Fujishima and Honda in 1972 [1]. It is now one of the most commonly used photocatalysts with numerous applications such as dye-sensitized solar cells [2], lithium ion batteries [3], water purification [4], and air purification [5]. TiO_2 has a band gap at approximately 3 eV, and thus requires blue or UV light to be active. There have been significant efforts to increase the absorption in the visible range by doping TiO_2 with non-metals (such as N, C) [6,7] and transition metals (such as Co, Rh, V, Fe, Cr, and Mn) [8]. Thakur et al. [9,10] reported production of nanomaterials of dopant free multiphase titanium oxides with increased absorption in vis-NIR region and average band gap of 2.39 eV. This behaviour of enhanced absorption spectrum of these nanomaterials was reportedly due to (i) presence of multiple titanium oxide phases absorbing at different wavelengths, (ii) synthesized by a “unique fusion of plume formation and vapour condensation mechanism”, and (iii) brought about by “interaction of ultra-short laser pulses and titanium substrate” using femtosecond laser ablation [10].

Amongst the nanoparticle synthesis methods, as evident from the

increase in the publications in last decade by a factor of 15 [11], pulsed laser ablation in liquids (PLAL) has been extensively explored as a simple, versatile and green method [12,13]. Significant efforts have been made specially to understand plasma and cavitation dynamics in PLAL [14–16]. A shortcoming of this method has been low nanoparticle productivity, however, the latest demonstrations have shown production rates of up to 4 g/h [17] for Au, Ag, Ti, Cu, Al and Pt. With the production of nanoparticles of metals, ceramics, alloys, and semi-conductors, PLAL has been demonstrated to be a promising method for production of variety of nanoparticles [18,19].

In PLAL, the liquid surrounding the target has a significant role on the morphology, structure and phase of the synthesized nanoparticles [13]. Kuwahara et al. reported that during PLA of copper in pressurized CO_2 , the ablation efficiency was several tens of times higher at elevated pressure [20]. In supercritical fluids, such as supercritical CO_2 (sc CO_2), the PLA-induced plasma has been reported to be dense consisting of highly active species, allowing the synthesis of exotic nanomaterials [21]. As a typical supercritical fluid, sc CO_2 , it is possible to change its solvent power just by changing the temperature and pressure. Owing to its zero surface tension, it penetrates and leaves nanostructures unharmed. Additionally, particle synthesis with sc CO_2 is a green process because CO_2 is non-toxic, rather inert, and recyclable in process and

* Corresponding author.

E-mail addresses: amandeep.singh@tut.fi (A. Singh), turkka.salminen@tut.fi (T. Salminen), mari.honkanen@tut.fi (M. Honkanen), jorma.vihinen@tut.fi (J. Vihinen), leo.hyvarinen@tut.fi (L. Hyvärinen), erkki.levanen@tut.fi (E. Levänen).

<https://doi.org/10.1016/j.apsusc.2019.01.172>

Received 30 August 2018; Received in revised form 14 December 2018; Accepted 18 January 2019

Available online 23 January 2019

0169-4332/ © 2019 Elsevier B.V. All rights reserved.

owing to its low critical point (7.4 MPa, 31.1 °C) [22], it is a low energy process especially compared to supercritical H₂O (22.1 MPa, 374 °C) [23]. Combination of plasma and supercritical fluids is sometimes advantageous also because of the synergic effect of highly reactive plasma species and superior transport properties of supercritical fluids [24]. Saitow first reported synthesis of silicon nanoclusters [25], as well as, gold nanospheres and nanonecklaces [26] by PLA in scCO₂. Nakahara et al. demonstrated PLA in scCO₂ as a promising method for synthesizing higher diamondoids, that are typically difficult to synthesize [27].

In our study, a titanium target was ablated in scCO₂ at 10 MPa and 50 °C using a 250 ns 1064 nm pulsed fiber laser at 101 kHz. To the best of our knowledge, this is the first study that demonstrates production of multiphase Ti_xO_y nanoparticles from titanium by PLA in scCO₂. The synthesized nanoparticles were studied by transmission electron microscope (TEM), x-ray diffraction (XRD), and Raman spectroscopy. By discussing the key results from (i) TEM, XRD and Raman for the nanoparticles and their phases formed from titanium by PLA in scCO₂, as well as (ii) their comparison with similar analysis from PLA of titanium in H₂O, this study demonstrates the potential of PLA in scCO₂ for synthesis of well-dispersed metastable multiphase nanomaterials without the use of liquid.

2. Experimental

2.1. Materials

A titanium sheet (99.99% pure), obtained from Goodfellow Cambridge Ltd., 3.2 mm thick and 50 × 50 mm, was cut into 15 × 15 mm sized target for the experiment. Carbon dioxide (≥99.8% pure with O₂ ≤ 20 ppm, H₂O ≤ 100 ppm) was obtained from Oy AGA Ab.

2.2. Pulsed laser ablation in scCO₂ and H₂O: setup and nanoparticle synthesis

The schematic in Fig. 1 shows the experimental setup for PLA in scCO₂. The experimental set-up consisted of a 70 W fiber laser ($\lambda = 1064$ nm) with a pulse duration of 250 ns and a repetition rate of 101 kHz. An 80 mm F-theta lens was used to focus the laser beam on the titanium target fixed inside the reaction chamber. The target was fixed using two neodymium magnets on a magnetic steel plate attached to the target holder and placed inside the chamber so that laser irradiates the target surface perpendicularly. The laser irradiated the titanium target for a 30-minute ablation period. The PLA in scCO₂ experiment was performed using a Thar Technologies Inc. RESS 250 system (Pittsburg, USA). The reaction chamber, made of 316SS steel, was suitable for pressures up to 60 MPa and temperatures up to 150 °C. It consisted of heating rods built into the walls and two sapphire windows, one of which was used to introduce the laser pulses into the chamber. There was no cooling system installed with the high-pressure chamber. The PC-controlled automatic back-pressure regulator (ABPR) meticulously governed the depressurization rate of the CO₂ after the ablation process ended. BPR was used only to depressurize at the end of ablation process, so not to avoid pressure increase. CO₂ (gas) was flushed through the reaction chamber prior to ablation in order to reduce the amount of ambient atmospheric gases inside the chamber, in particular to alleviate the effects of O₂ and N₂. CO₂ was pumped into the chamber using a high-pressure piston-pump at a constant rate of 20 g/min until the pressure stabilized at 10 MPa. The temperature of the reaction chamber was set to 50 °C. After the chamber pressure and temperature stabilized at 10 MPa and 50 °C respectively, laser beam scanned an area of 6 × 6 mm at a scanning rate of 2 m/s. After 30 min of laser ablation followed by depressurisation, the nanoparticles were collected from the chamber as a powder. The pressure and temperature sensors had an accuracy of 0.05 MPa and 1.1 °C respectively, as guaranteed by the supplier of the CO₂ system. The pressure sensor was just before the inlet valve of BPR while the temperature sensor was fitted inside the vessel. As the end of 30 min ablation, the pressure and

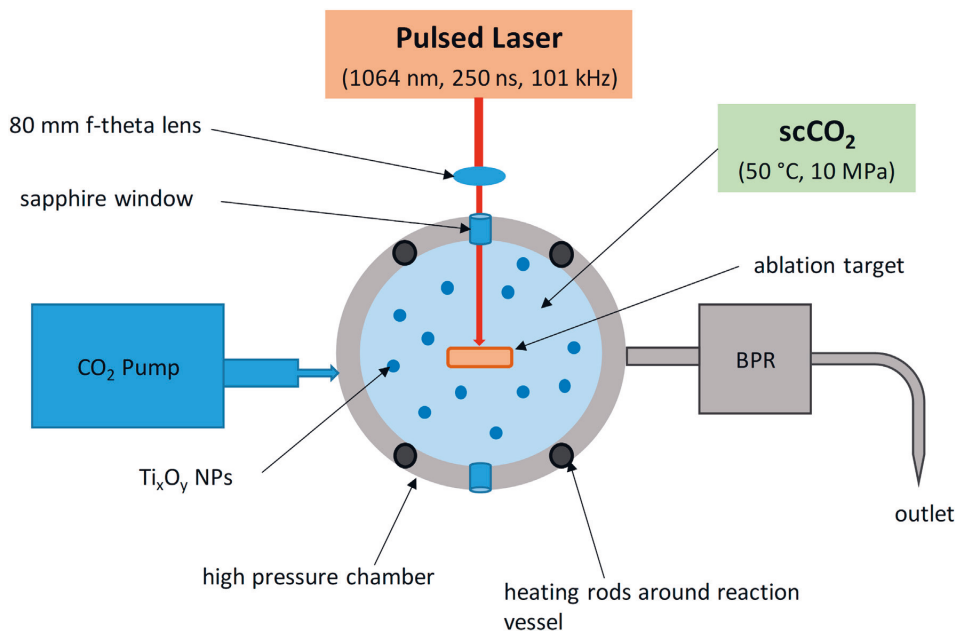


Fig. 1. Schematic of PLA in scCO₂.

temperature inside the chamber soared to 10.7 MPa and 59.4 °C respectively.

For PLA in H₂O, the schematic and set-up of equipment is explained in our previous publication [28]. However, the laser and its parameters used were same as in the aforementioned PLA in scCO₂ experiment and ablation time was 30 min. The water film thickness above the target was 4 mm. The loss in laser transmission was measured to be same for 13 mm thick sapphire window (PLA in scCO₂) and 4 mm thick water film above target (PLA in H₂O). After the experiment, the nanoparticles were collected in the form of nanoparticle suspension.

2.3. Characterization methods

Jeol JEM-2010 TEM was used for imaging the nanoparticles to characterize the shape and size of nanoparticles. A high resolution TEM (Jeol, JEM-2200FS HRTEM) was used for high resolution imaging of nanoparticles. The TEM samples for nanoparticles obtained from PLA in scCO₂ were prepared by directly touching the TEM copper grids with a holey carbon film on dry nanoparticles from reaction chamber. TEM samples for nanoparticle suspensions from PLA in H₂O were made by dropping the suspension on copper grid with holey carbon film and allowing them to dry. Selected area electron diffraction (SAED) patterns were also obtained from the same TEM samples to study the crystallinity of samples.

XRD measurements were performed on a Panalytical Empyrean Multipurpose Diffractometer with a CuK α x-ray source ($\lambda = 0.15418$ nm) and a solid-state pixel detector, PIXcel3D, which measured the scattered intensities as a function of scattering angle (2 θ). The x-ray generator was powered at 45 kV and 40 mA. For XRD measurements, the scan range was 20.00°–80.95° with a 0.05° step size. It used a soller slit with 0.04 rad opening. The phase identification of the peaks in the XRD pattern was performed with Panalytical HighScore Plus software (version 3.0.5) from the database PDF-4+ of the International Centre for Diffraction data (Database version 4.1065). For further phase analysis, the Raman spectra were measured using Renishaw inVia Qontor Raman microscope. A 532 nm wavelength laser was used for excitation. For both XRD and Raman, the sample was as-deposited nanoparticle powders (from PLA in scCO₂) on the non-ablated part of the target. So, we can expect high peaks for titanium metal in the XRD pattern, however, not in the Raman plot since metals are not Raman active. The nanoparticle suspension from PLA in H₂O was dried to obtain powder of nanoparticles upon which XRD and Raman was performed.

3. Results and discussion

3.1. Comparative TEM analysis for PLA in scCO₂ and PLA in H₂O

Fig. 2a and b show the TEM micrographs for nanoparticles synthesized by PLA of titanium in scCO₂. The TEM images show uniformly dispersed spherical nanoparticles (Fig. 2a). The formation of round nanoparticles with PLA is well reported and is attributed to the diffusion of hot surface atoms on nanoparticles as well as melting of already synthesized nanoparticles because of laser processing in order to decrease interfacial energy [10]. In the SAED pattern (Fig. 2a inset), crystalline rings were observed indicating the presence of mainly nanocrystalline particles. It is noteworthy to mention we did not observe any large nanospheres in this study such as the ones reported in a study by Saitow et al. where they observed 400 nm large gold nanospheres as a result of PLA in scCO₂ at relatively higher CO₂ densities (1.7 g/cm³) [26]. In our study, the CO₂ density varies between 0.34 and 0.38 g/cm³ for pressures and temperatures mentioned in the experimental section. At smaller densities, PLA in supercritical fluids such as CO₂ and trifluoromethane (CHF₃) leads to formation of nanoparticles few tens of nanometers in diameter, while at higher densities, it leads to formation of large nanospheres and nanonecklaces [26,29].

Fig. 3a and b show the TEM micrographs of the nanoparticles synthesized by PLA of titanium in H₂O. In the TEM images, round nanoparticles were observed to form web-like structures. Others have reported formation of similar web-like structure upon PLA in H₂O [30]. In addition, with higher magnification (Fig. 3b), randomly shaped nanoparticles were observed that joined with each other as well as with the spherical bigger nanoparticle indicating agglomeration. SAED pattern taken from this region (Fig. 3a inset) showed crystalline rings and spots and maybe also diffuse rings, indicating presence of crystalline and possibly some amorphous forms.

In PLA in scCO₂, the nanoparticles were uniformly dispersed and non-agglomerated. This may occur due to the polar nature of synthesized nanoparticles surrounded by scCO₂, which is non-polar and has zero surface tension. For PLA in scCO₂ (Fig. 2a and b), randomly shaped nanoparticles observed for PLA in H₂O (Fig. 3a and b), were not observed. In case of PLA in scCO₂, in theory, the electrical double layer, that usually surrounds the nanoparticles in aqueous medium, should be absent. In addition, no hydrogen is involved in the process, so the possibility of firstly hydrogen bonding of the particles and secondly presence of OH⁻, H₃O⁺, and H⁺ ions can be eliminated due to which no agglomeration was observed. This suggests PLA in scCO₂ in a promising method for synthesis of well-dispersed non-agglomerated spherical-shaped nanoparticles via a dry process. Later after the process is finished, it is however possible that H₂O (moisture) adsorbs on the nanoparticles when exposed to the ambient environment outside the reaction chamber causing some agglomeration.

3.2. Comparative phase analysis – Raman and XRD of the nanoparticles

Raman measurements from the nanoparticle powder on the target surface (Fig. 4a) synthesized by PLA in scCO₂ indicated presence of mainly anatase-TiO₂ with the possibility of minor amounts of titanium (III) oxide (Ti₂O₃). The broad features might belong to smaller peaks of anatase, titanium(III) oxide (Ti₂O₃) or other titanium oxides. Raman analysis did not show peaks at 222, 420 or 605 cm⁻¹ corresponding to TiC indicating absence of titanium carbides. The Raman spectra for nanoparticles synthesized by PLA in H₂O (Fig. 4b) showed two prominent peaks at 440 cm⁻¹ and 610 cm⁻¹ indicating presence of mostly rutile-TiO₂. The peak at around 150 cm⁻¹ suggests presence of anatase, brookite or a combination of both. In addition to those, the broad pedestal up to 900 cm⁻¹ may signify presence of disordered or amorphous material.

XRD results for PLA in scCO₂ synthesized nanoparticles (Fig. 5a) corroborated the presence of anatase-TiO₂ and titanium(III) oxide (Ti₂O₃). Additionally, XRD, indicated presence of a non-stoichiometric oxide of titanium - TiO_{0.89}, which is a high-temperature phase. XRD from the samples prepared in H₂O (Fig. 5b) strongly indicates that the material is mostly rutile-TiO₂. There were four prominent peaks observed for rutile-TiO₂ at 27.4, 36.0, 41.2, and 54.3°. The broadened peak at 54.3 also has a shoulder due to another rutile peak at 56.6°. The peaks in XRD pattern are broadened due to small size of nanoparticles. The small peak at 25.3° may correspond to brookite-TiO₂. The broadened small peaks between 62 and 70° correspond to rutile-TiO₂ or a combination of rutile-TiO₂ and brookite-TiO₂ phase. This agrees with the Raman results that rutile was the main phase and along with trace amounts of brookite. Interestingly, from the Raman and XRD investigation, we observe formation of mostly metastable phases in PLA in scCO₂ – anatase TiO₂, Ti₂O₃ and TiO_{0.89}, while PLA in H₂O resulted in mostly stable phase – rutile TiO₂.

3.3. Comparative analysis of source of oxidation

CO₂ has low reactivity; however, in the presence of high-temperature high-pressure plasma, its dissociation forms O⁻/O₂⁻, with which the ablated plasma species can react. The minimum energy path for the dissociation of CO₂ leads to CO and O⁻, which can further combine to

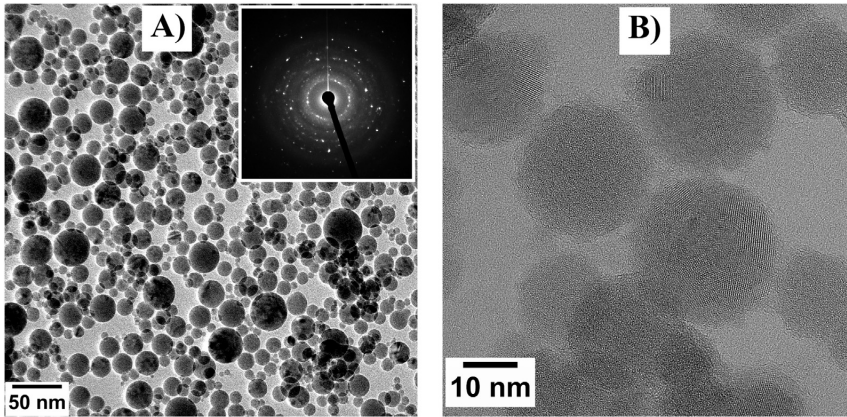


Fig. 2. TEM micrographs (a and b) and SAED pattern (as inset in a) from nanoparticles synthesized by PLA in $s\text{CO}_2$.

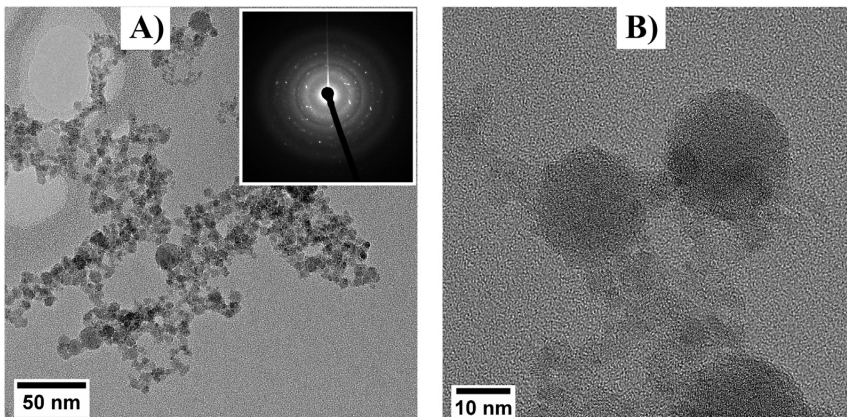


Fig. 3. TEM micrographs (a and b) and SAED pattern (as inset in a) from nanoparticles synthesized by PLA in H_2O .

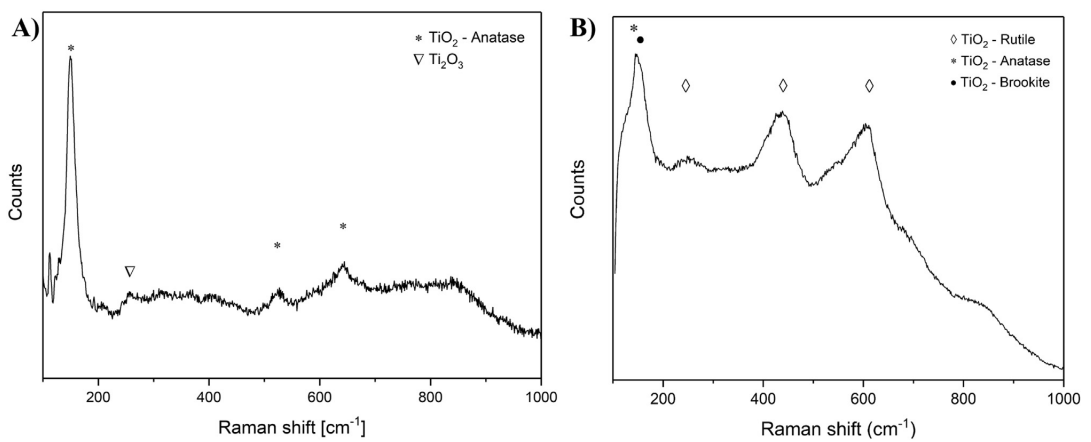


Fig. 4. Raman spectra of nanoparticles formed by (a) PLA in $s\text{CO}_2$ and (b) PLA in H_2O .

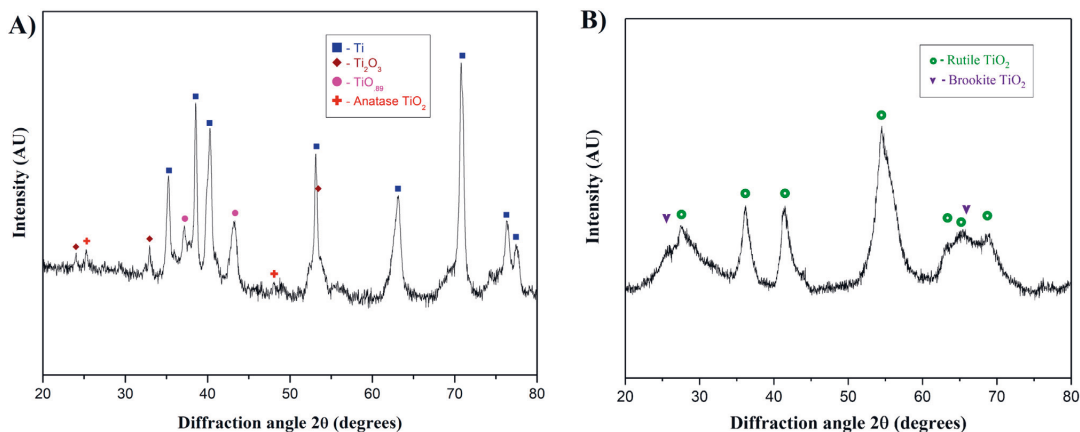


Fig. 5. XRD pattern of nanoparticles formed by (a) PLA in scCO₂ and (b) PLA in H₂O.

form CO₂ and O₂. Under extreme conditions, CO₂ can dissociate directly to carbon and molecular oxygen through vacuum ultraviolet photo-dissociation [31] or dissociative electron attachment [32]. For PLA in H₂O, the laser ablated materials react with oxygen [33], that is either dissolved in water [34] or bound to water molecule which can be made available by plasma-induced water splitting [35].

According to Ellingham diagram [36], CO₂ is more oxidizing than H₂O at temperatures below 1000 K. However, in our experiments the samples prepared in H₂O were completely oxidised which can be explained if the oxygen, that is dissolved in the water, is responsible for the oxidation. Thorough thermodynamic analysis of this process is beyond the scope of this study.

Although carbide compounds were not observed in this study, PLA in scCO₂ at higher CO₂ pressures will make an interesting future scope of work to reveal the consequential effect of variation in plasma and cavitation bubble dynamics (or dynamics of the bubble-like hollow) on nanoparticle size, morphology, and phase.

4. Conclusion

In summary, production of well-dispersed non-agglomerated Ti_xO_y nanoparticles by PLA of titanium in scCO₂ was successfully demonstrated via green synthesis using only supercritical CO₂ as the solvent. The results from this technique were compared against results from PLA of titanium in H₂O. The nanoparticles were studied by TEM, Raman microscopy and XRD. TEM showed spherical-shaped, well-dispersed crystalline nanoparticles. By PLA in scCO₂, we also report absence of any web-like networks or unwanted randomly shaped nanoparticles that were observed for nanoparticles synthesized in PLA in H₂O. Raman and XRD indicated nanoparticles synthesized by PLA in scCO₂ were anatase-TiO₂, Ti₂O₃, and TiO_{0.89}. For nanoparticles synthesized by PLA in H₂O, Raman and XRD indicated presence of mostly rutile-TiO₂ along with trace amounts of brookite-TiO₂. This suggests that PLA in scCO₂ favours formation of metastable phases and forms with crystallographic defects and vacancies such as TiO_{0.89}, while PLA in H₂O favours formation of mostly stable phase such as rutile-TiO₂.

Acknowledgements

This work was supported by European Commission's Horizon 2020 project 'NanoStencil' - Proposal number 767285. We acknowledge the provision of facilities and technical support by Aalto University at OtaNano - Nanomicroscopy Center (Aalto-NMC). We acknowledge senior scientist Dr. Hua Jiang for performing high resolution TEM studies

at Aalto University. This work made use of Tampere Microscopy Center facilities at Tampere University.

Declaration

The authors declare no conflict of interest.

References

- [1] A. Fujishima, K. Honda, Electrochemical photolysis of water at a semiconductor electrode, *Nature* 238 (1972) 37–38, <https://doi.org/10.1038/238037a0>.
- [2] K. Tennakone, A.R. Kumarasinghe, P.M. Sirmanne, G.R.R.A. Kumara, Deposition of thin polycrystalline films of cuprous thiocyanate on conducting glass and photo-electrochemical dye-sensitization, *Thin Solid Films* 261 (1995) 307–310, [https://doi.org/10.1016/S0040-6090\(95\)06523-7](https://doi.org/10.1016/S0040-6090(95)06523-7).
- [3] I. Exnar, L. Kavan, S.Y. Huang, M. Grätzel, Novel 2 V rocking-chair lithium battery based on nano-crystalline titanium dioxide, *J. Power Sources* 68 (1997) 720–722, [https://doi.org/10.1016/S0378-7753\(96\)02581-5](https://doi.org/10.1016/S0378-7753(96)02581-5).
- [4] D. Friedmann, C. Mendive, D. Bahnemann, TiO₂ for water treatment: parameters affecting the kinetics and mechanisms of photocatalysis, *Appl. Catal. B Environ.* 99 (2010) 398–406, <https://doi.org/10.1016/j.apcatb.2010.05.014>.
- [5] A. Fujishima, T.N. Rao, D.A. Tryk, Titanium dioxide photocatalysis, *J Photochem Photobiol C: Photochem Rev* 1 (2000) 1–21, [https://doi.org/10.1016/S1389-5567\(00\)00002-2](https://doi.org/10.1016/S1389-5567(00)00002-2).
- [6] C. Burda, Y. Lou, X. Chen, A.C.S. Samia, J. Stout, J.L. Gole, Enhanced nitrogen doping in TiO₂ nanoparticles, *Nano Lett.* 3 (2003) 1049–1051, <https://doi.org/10.1021/nl034332o>.
- [7] D. Chen, Z. Jiang, J. Geng, Q. Wang, D. Yang, Carbon and nitrogen co-doped TiO₂ with enhanced visible-light photocatalytic activity, *Ind. Eng. Chem. Res.* 46 (2007) 2741–2746, <https://doi.org/10.1021/ie061491k>.
- [8] B. Liu, H.M. Chen, C. Liu, S.C. Andrews, C. Hahn, P. Yang, Large-scale synthesis of transition-metal-doped TiO₂ nanowires with controllable overpotential, *J. Am. Chem. Soc.* 135 (2013) 9995–9998, <https://doi.org/10.1021/ja403761s>.
- [9] P. Thakur, B. Tan, K. Venkatakrishnan, Multi-phase functionalization of titanium for enhanced photon absorption in the vis-NIR region, *Sci. Rep.* 5 (2015) 15354, <https://doi.org/10.1038/srep15354>.
- [10] P. Thakur, B. Tan, K. Venkatakrishnan, Multiphase titanium oxide nanomaterial for augmented vis-NIR photon absorption, *Sol. Energy Mater. Sol. Cells* 152 (2016) 161–169, <https://doi.org/10.1016/j.solmat.2016.03.037>.
- [11] S. Barcikowski, F. Devesa, K. Moldenhauer, Impact and structure of literature on nanoparticle generation by laser ablation in liquids, *J. Nanopart. Res.* 11 (2009) 1883–1893, <https://doi.org/10.1007/s11051-009-9765-0>.
- [12] D. Zhang, B. Gökce, S. Barcikowski, Laser synthesis and processing of colloids: fundamentals and applications, *Chem. Rev.* 117 (2017) 3990–4103, <https://doi.org/10.1021/acs.chemrev.6b00468>.
- [13] H. Zeng, X.-W. Du, S.C. Singh, S.A. Kulnich, S. Yang, J. He, W. Cai, Nanomaterials via laser ablation/irradiation in liquid: a review, *Adv. Funct. Mater.* 22 (2012) 1333–1353, <https://doi.org/10.1002/adfm.201102295>.
- [14] J. Lam, D. Amans, F. Chaput, M. Diouf, G. Ledoux, N. Mary, K. Masenelli-Varlot, V. Motto-Ros, C. Dujardin, γ-Al₂O₃ nanoparticles synthesised by pulsed laser ablation in liquids: a plasma analysis, *Phys. Chem. Chem. Phys.* 16 (2014) 963–973, <https://doi.org/10.1039/C3CP53748J>.
- [15] R. Tanabe, T.T.P. Nguyen, T. Sugiura, Y. Ito, Bubble dynamics in metal nanoparticle formation by laser ablation in liquid studied through high-speed laser stroboscopic videography, *Appl. Surf. Sci.* 351 (2015) 327–331, <https://doi.org/10.1016/j>.

- apsusc.2015.05.030.
- [16] J. Lam, J. Lombard, C. Dujardin, G. Ledoux, S. Merabia, D. Amans, Dynamical study of bubble expansion following laser ablation in liquids, *Appl. Phys. Lett.* 108 (2016) 074104, <https://doi.org/10.1063/1.4942389>.
- [17] R. Streubel, S. Barcikowski, B. Göcke, Continuous multigram nanoparticle synthesis by high-power, high-repetition-rate ultrafast laser ablation in liquids, *Opt. Lett.* 41 (2016) 1486, <https://doi.org/10.1364/OL.41.001486>.
- [18] Z. Yan, D.B. Chrisey, Pulsed laser ablation in liquid for micro-/nanoparticle generation, *J Photochem Photobiol C: Photochem Rev* 13 (2012) 204–223, <https://doi.org/10.1016/j.jphotochemrev.2012.04.004>.
- [19] V. Amendola, M. Meneghetti, What controls the composition and the structure of nanomaterials generated by laser ablation in liquid solution? *Phys. Chem. Chem. Phys.* 15 (2013) 3027–3046, <https://doi.org/10.1039/C2CP42895D>.
- [20] Y. Kuwahara, T. Saito, M. Haba, T. Iwanaga, M. Sasaki, M. Goto, Nanosecond pulsed laser ablation of copper in supercritical carbon dioxide, *Jpn. J. Appl. Phys.* 48 (2009) 040207, <https://doi.org/10.1143/JJAP.48.040207>.
- [21] K. Urabe, T. Kato, S. Stauss, S. Himeno, S. Kato, H. Muneoka, M. Baba, T. Suemoto, K. Terashima, Dynamics of pulsed laser ablation in high-density carbon dioxide including supercritical fluid state, *J. Appl. Phys.* 114 (2013) 143303, <https://doi.org/10.1063/1.4824538>.
- [22] W. Leitner, Designed to dissolve, *Nature* 405 (2000) 129–130, <https://doi.org/10.1038/35012181>.
- [23] N. Takada, S. Machmudah, Characteristics of optical emission intensities and bubblelike phenomena induced by laser ablation in supercritical fluids, *Jpn. J. Appl. Phys.* 53 (2014) 010213-1–010213-8 <http://iopscience.iop.org/1347-4065/53/1/010213>.
- [24] T. Tomai, K. Katahira, H. Kubo, Y. Shimizu, T. Sasaki, N. Koshizaki, K. Terashima, Carbon materials syntheses using dielectric barrier discharge microplasma in supercritical carbon dioxide environments, *J. Supercrit. Fluids* 41 (2007) 404–411, <https://doi.org/10.1016/j.supflu.2006.12.003>.
- [25] K. Saitow, Silicon nanoclusters selectively generated by laser ablation in supercritical fluid, *J. Phys. Chem. B* 109 (2005) 3731–3733, <https://doi.org/10.1021/jp0442551>.
- [26] K. Saitow, T. Yamamura, T. Minami, Gold nanospheres and nanonecklaces generated by laser ablation in supercritical fluid, *J. Phys. Chem. C* 112 (2008) 18340–18349, <https://doi.org/10.1021/jp805978g>.
- [27] S. Nakahara, S. Stauss, T. Kato, T. Sasaki, K. Terashima, Synthesis of higher diamondoids by pulsed laser ablation plasmas in supercritical CO₂, *J. Appl. Phys.* 109 (2011) 1–8, <https://doi.org/10.1063/1.3599887>.
- [28] A. Singh, J. Vihinen, E. Frankberg, L. Hyvärinen, M. Honkanen, E. Levänen, Pulsed laser ablation-induced green synthesis of TiO₂ nanoparticles and application of novel small angle X-ray scattering technique for nanoparticle size and size distribution analysis, *Nanoscale Res. Lett.* 11 (2016) 447, <https://doi.org/10.1186/s11671-016-1608-1>.
- [29] K.I. Saitow, Y. Okamoto, Y.F. Yano, Fractal of gold nanoparticles controlled by ambient dielectricity: synthesis by laser ablation as a function of permittivity, *J. Phys. Chem. C* 116 (2012) 17252–17258, <https://doi.org/10.1021/jp304109h>.
- [30] G. Ledoux, D. Amans, C. Dujardin, K. Masenelli-Varlot, Facile and rapid synthesis of highly luminescent nanoparticles via pulsed laser ablation in liquid, *Nanotechnology* 20 (2009) 445605, <https://doi.org/10.1088/0957-4484/20/44/445605>.
- [31] Z. Lu, Y.C. Chang, Q.-Z. Yin, C.Y. Ng, W.M. Jackson, Evidence for direct molecular oxygen production in CO₂ photodissociation, *Science* 346 (2014) 61–64, <https://doi.org/10.1126/science.1257156> (80-).
- [32] X.-D. Wang, X.-F. Gao, C.-J. Xuan, S.X. Tian, Dissociative electron attachment to CO₂ produces molecular oxygen, *Nat. Chem.* 8 (2016) 258–263, <https://doi.org/10.1038/nchem.2427>.
- [33] J. Lam, D. Amans, C. Dujardin, G. Ledoux, A.-R. Allouche, Atomistic mechanisms for the nucleation of aluminum oxide nanoparticles, *J. Phys. Chem. A* 119 (2015) 8944–8949, <https://doi.org/10.1021/acs.jpca.5b05829>.
- [34] G. Marzun, H. Bönemann, C. Lehmann, B. Spliethoff, C. Weidenthaler, S. Barcikowski, Role of dissolved and molecular oxygen on Cu and PtCu alloy particle structure during laser ablation synthesis in liquids, *ChemPhysChem* 18 (2017) 1175–1184, <https://doi.org/10.1002/cphc.201601315>.
- [35] M. Kalus, N. Bärsch, R. Streubel, E. Göcke, S. Barcikowski, B. Göcke, How persistent microbubbles shield nanoparticle productivity in laser synthesis of colloids – quantification of their volume, dwell dynamics, and gas composition, *Phys. Chem. Chem. Phys.* 19 (2017) 7112–7123, <https://doi.org/10.1039/C6CP07011F>.
- [36] D.R. Gaskell, *Introduction to the Thermodynamics of Materials*, Taylor and Francis, London, 1995.

PUBLICATION IV


Carbon coated TiO₂ nanoparticles prepared by pulsed laser ablation in liquid, gaseous and supercritical CO₂

A. Singh, T. Salminen, M. Honkanen, J.-P. Nikkanen, T. Vuorinen, R. Kari, J. Vihinen, E. Levänen

Nanotechnology, Vol. 31, p. 085602
<https://doi.org/10.1016/j.apsusc.2019.01.172>

Publication reprinted with the permission of the copyright holders.

Carbon coated TiO₂ nanoparticles prepared by pulsed laser ablation in liquid, gaseous and supercritical CO₂

Amandeep Singh¹ , Turkka Salminen², Mari Honkanen², Juha-Pekka Nikkanen¹, Tommi Vuorinen³, Risto Kari¹, Jorma Vihinen⁴ and Erkki Levänen¹

¹Materials Science and Environmental Engineering Unit, Faculty of Engineering and Natural Sciences, PO Box 527 FI-33014, Tampere University, Tampere, Finland

²Tampere Microscopy Center, PO Box 692, FI-33014, Tampere University, Tampere, Finland

³VTT Technical Research Centre of Finland Ltd, PO Box 1300, FI-33101, Tampere, Finland

⁴Mechanical Engineering Unit, Faculty of Engineering and Natural Sciences, PO Box 527 FI-33014, Tampere University, Tampere, Finland

E-mail: amandeep.singh@tuni.fi

Received 7 July 2019, revised 20 September 2019

Accepted for publication 1 November 2019

Published 26 November 2019



CrossMark

Abstract

We report on the synthesis of TiO₂ nanoparticles using nanosecond pulse laser ablation of titanium in liquid, gaseous and supercritical CO₂. The produced particles were observed to be mainly anatase-TiO₂ with some rutile-TiO₂. In addition, the particles were covered by a carbon layer. Raman and x-ray diffraction data suggested that the rutile content increases with CO₂ pressure. The nanoparticle size decreased and size distribution became narrower with the increase in CO₂ pressure and temperature, however the variation trend was different for CO₂ pressure compared to temperature. Pulsed laser ablation in pressurized CO₂ is demonstrated as a single step method for making anatase-TiO₂/carbon nanoparticles throughout the pressure and temperature ranges 5–40 MPa and 30 °C–50 °C, respectively.

Keywords: pulsed laser ablation, supercritical fluids, core-shell particles, nanoparticle size control, anatase-TiO₂ Raman XPS XRD, metastable phase, high pressure CO₂

(Some figures may appear in colour only in the online journal)

Introduction

Titanium dioxide is among the most studied nanomaterials as it is an important photocatalytically active material with applications such as in water purification [1], lithium ion batteries [2], and solar cells [3]. Combining TiO₂ with carbon nanostructures such as graphene to form graphene/TiO₂ heterostructures has been reported as a new optical and electronic device platform with dual functionality of field effect and photosensitivity in bottom gated field effect transistors [4]. In another study, the presence of core-shell TiO₂-carbon structures as a support material was reported to enhance the catalytic activity of a Pt catalyst and improve its

stability in direct methanol fuel cells compared to traditionally used Pt catalyst with carbon black support [5]. Core-shell nanoparticles of various compositions have extensive applications and have been well highlighted in the recent reviews reporting their use in catalysis and electrocatalysis [6], energy storage and conversion (such as in lithium ion batteries, supercapacitors, and quantum dot solar cells) [7], and medical biotechnology (such as in molecular bioimaging, drug delivery, and cancer treatment) [8]. Techniques for preparing core-shell nanoparticles include chemical vapour deposition [9], wet-chemistry based methods such as sol-gel synthesis [10], and polymerization [11], physical methods such as flame synthesis [12], plasma-based

synthesis [13, 14] and spray pyrolysis [15]. Pulsed laser ablation in liquids (PLAL) for core-shell nanoparticle generation [16] is another physical method that, similar to the other physical methods, is an *in situ* synthesis process, requires little sample preparation, few synthesis steps and unlike in wet-chemistry methods, does not require environmentally hazardous solvents. Due to high yield relative to solid educt mass and no waste of reagents, it may further save waste management and disposal costs compared to chemical methods [17].

PLAL is often called a green technique as it can be used to synthesize nanoparticles without the need of toxic chemicals [17]. The synthesis of well-dispersed unagglomerated nanoparticles of titanium oxides has been demonstrated in supercritical carbon dioxide (scCO₂) [18]. In the supercritical state, CO₂ may penetrate and leave nanostructures unharmed due to absence of surface tension. The surrounding fluid in pulsed laser ablation (PLA) plays an important role on the phase, structure and morphology of nanoparticles. In the first study on PLA of gold in scCO₂, Saitow *et al* reported that nanoparticles consisted of two size distributions: nanoparticles with average diameters 30 nm and around 500 nm [19]. Production of nanoparticles from various materials has been reported using PLA in scCO₂. The target materials include silicon [20], gold [19], silver [21], copper [22], pyrolytic graphite [23] and titanium [18]. In addition to the laser parameters and the ablated material, the CO₂ temperature and pressure is important as it changes the properties of scCO₂ to be either liquid-like or gas-like which may further affect the nanoparticle size, morphology and phase. In a previous study, the effect of scCO₂ pressure, density and temperature on a gold target has been reported [24]. However, there are no studies on generation of core-shell nanoparticles by PLA when CO₂ is in the supercritical regime, to the best of our knowledge. Previously, PLA in pressurized CO₂ has been demonstrated to form metal-core carbon-shell nanoparticles of Ni-carbon in gaseous CO₂ [25] and Au-carbon in liquid and gaseous CO₂ [26].

This study demonstrates single-step synthesis of TiO₂-carbon core-shell nanoparticles from titanium by PLA in pressurized CO₂ in liquid, gaseous and supercritical state. This demonstrates the potential of PLA in scCO₂ for synthesis of core-shell particles. We report on the effect of CO₂ pressure and temperature on the size, size distribution and phase of core-shell nanoparticles synthesized in liquid, gaseous and scCO₂. The effect of different test condition i.e. supercritical state CO₂ against liquid and gaseous CO₂ is also reported. PLA in pressurized CO₂ was carried out using a 250 ns pulse fibre laser with wavelength of 1062 nm and repetition rate of 101 kHz to synthesize nanoparticles. Scanning transmission electron microscopy, (S)TEM, x-ray photoelectron spectroscopy (XPS), Raman, x-ray diffraction (XRD), and ultraviolet-visible (UV-Vis) spectroscopy techniques were used to study the synthesized nanoparticles and evaluate the effect of CO₂ pressures 5–40 MPa and temperatures 30 °C–50 °C on the nanoparticle size, size distribution and phase.

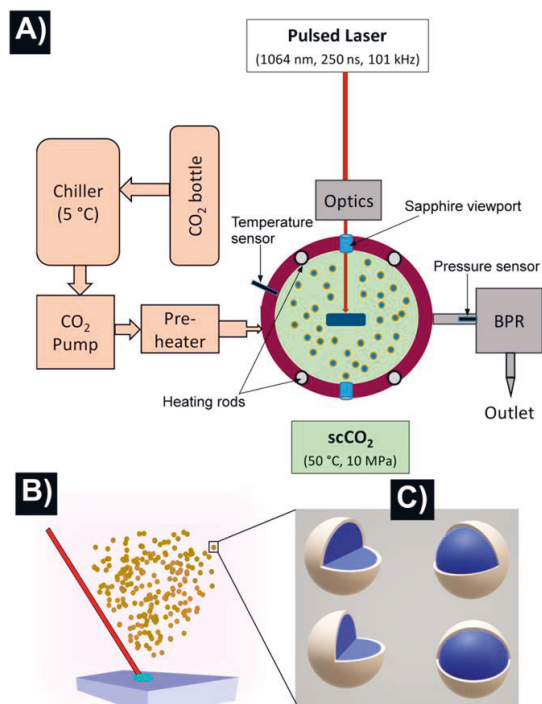


Figure 1. Shows (a) schematic of the experimental setup, (b) schematic of ablation of titanium to produce nanoparticles, (c) synthesized nanoparticles consist of core-shell type nanoparticles.

Experimental

Nanosecond laser ablation in liquid, gaseous and supercritical CO₂

PLA in CO₂ was carried out using a 250 ns pulse fibre laser with wavelength of 1062 nm, and repetition rate of 101 kHz. The laser beam was focused using an 80 mm telecentric f-Theta lens to a spot diameter of 35 μ m on the titanium target and scanned on an area of 64 mm². The beam energy was 690 μ J per pulse for 101 kHz repetition rate. The experimental set-up consisted of a titanium target (99.99% pure, Goodfellow Cambridge Ltd) fitted inside the autoclave (made of stainless steel 316 with pressure and temperature limits of 62 MPa and 150 °C, respectively) in such a way that it could be scanned with the laser through the sapphire optical viewport as shown in the schematic (figure 1(a)). Figure 1(b) shows the schematic inside the autoclave where laser irradiates the target and nanoparticles are synthesized. Figure 1(c) shows a schematic of these nanoparticles that consisted of mostly core-shell nanoparticles. The ablation experiments were conducted at five different CO₂ pressures: 5, 10, 15, 20 and 40 MPa. CO₂ (>99.8% pure) was pumped into the autoclave with a high-pressure piston pump. CO₂ was cooled to 5 °C in the chiller before being pumped. Between the pump and the autoclave, CO₂ passed through a heat exchanger where it was warmed and converted to scCO₂. The heating

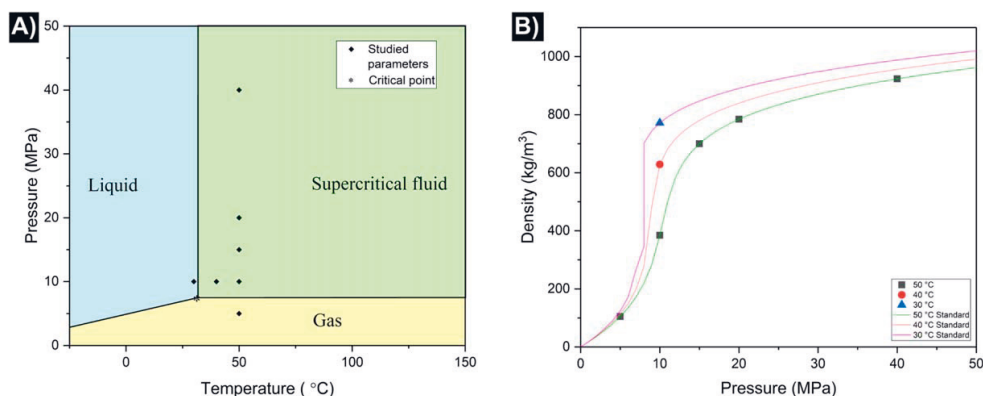


Figure 2. (a) Experimental parameters used in this study are plotted on CO₂ phase diagram, (b) CO₂ densities corresponding to the experimental parameters used are plotted against the standard CO₂ curves at 30 °C, 40 °C and 50 °C.

rods, installed in the walls of the autoclave, were used to heat it to 30 °C, 40 °C, and 50 °C for the corresponding experiments. After the temperature and pressure stabilized at the desired value, the target was ablated with the laser for 30 min using a scanning speed of 2 m s⁻¹ to cover a 7 × 7 mm pattern. To collect the nanoparticle powder, the autoclave was depressurized with an automatic backpressure regulator at a rate of 5 s MPa⁻¹. The pressure sensor with an accuracy of 0.05 MPa was located just before the inlet valve of backpressure regulator while the temperature sensor with accuracy of 1.1 °C was located inside the chamber. This study comprised of seven PLA tests in pressurized CO₂, five in scCO₂, one in liquid CO₂ and one in gaseous CO₂. To study the effect of CO₂ pressure and temperature, the tests may be divided in two parts: (1) CO₂ temperature fixed at 50 °C while five different pressures 5, 10, 15, 20, and 40 MPa were tested, and (2) CO₂ pressure fixed at 10 MPa while different temperatures 30 °C, 40 °C and 50 °C were tested. The pressure and temperature values of these tests are marked in figure 2(a). In figure 2(b), the symbols represent the densities for the selected CO₂ parameters in this study while the standard curves taken from the National Institute of Standards and Technology, US Department of Commerce [27] show the variation of CO₂ density with pressure for three temperatures 30 °C, 40 °C, and 50 °C.

Characterization methods

The nanoparticle powders were characterized by using a Jeol-JEM F200 (S)TEM with a Jeol Dual electron energy dispersive spectrometer (EDS), Renishaw InVia Qontor Raman microscope, Panalytical Empyrean Multipurpose Diffractometer for XRD, PHI Quantum 2000 for XPS and by Shimadzu spectrophotometer for determination of band-gap energy.

For (S)TEM, the samples were prepared by touching the TEM copper grid containing holey carbon film with the nanoparticle powder. From the TEM images, diameters of 400 nanoparticles were measured using Image J software

(Version 1.50i) and to estimate the size distributions and average particle size for each sample. STEM-EDS was used in line analysis and spot analysis mode to analyse the variation in the elemental composition of the nanoparticles and the layer on them. Phase analysis of the nanoparticle powders was analysed with the Renishaw InVia Qontor Raman microscope using a 532 nm laser. The laser power was 0.175 μW. The XRD patterns of the nanoparticle powders were obtained using the Panalytical Empyrean Multipurpose Diffractometer with a CuKα x-ray source at wavelength of 0.1541 nm. The scattered intensities were measured using a solid-state pixel detector, PIXcel3D attached to the diffractometer. The x-ray generator operating values were 45 kV and 40 mA. The data was collected in the range of $2\theta = 10.00^\circ$ – 80.00° and for a step size of $2\theta = 0.02^\circ$. Panalytical HighScore Plus software (version 3.0.5) was used for the identification of phases in the XRD pattern based on the database PDF-4 + of the International Centre for Diffraction data (version 4.1065). The XPS analysis was performed with PHI Quantum 2000 spectrometer with an Al 1486.6 eV mono x-ray source at 24.3 W. The XPS sample was prepared carefully spreading the nanoparticle powder on top of a double-sided tape that was attached to a metal plate. The measurement was done with a stationary beam with a beam diameter of 100 μm. The optical properties of the material were studied using a spectrophotometer (Shimadzu UV 3600) in reflectance mode. The absorbance spectra were measured for the wavelength range 300–900 nm. The plotted Tauc-plots were used to estimate the band-gap energy of the material.

Results and discussion

The visual appearance of the nanoparticles was bluish-white when the autoclave was opened and did not change during several months of storage. The nanoparticles were in the form of dry and loose powder. The results and discussion is divided into two sections. First section deals with the analysis of

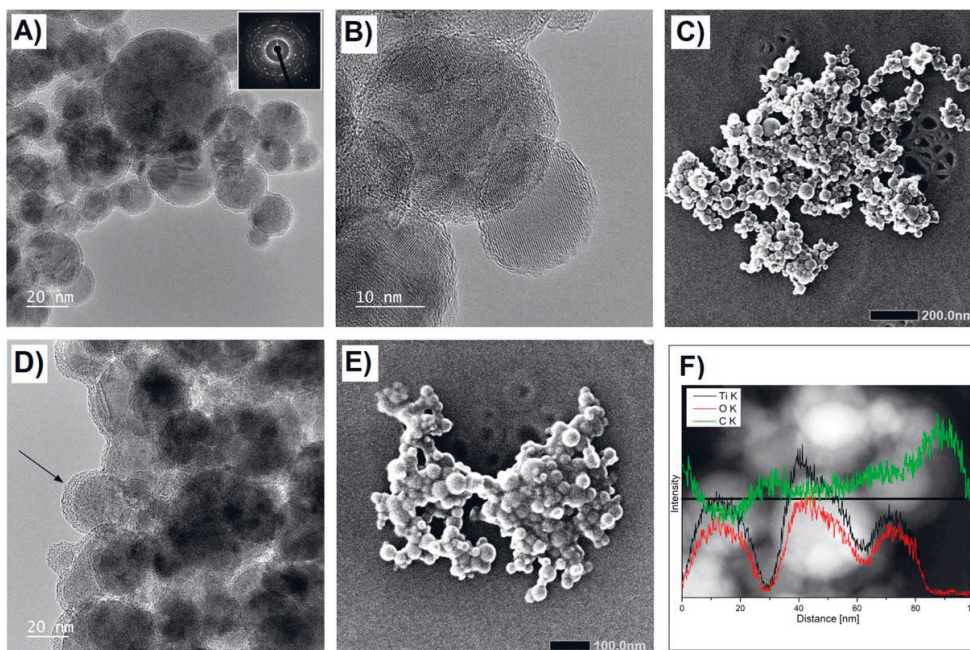


Figure 3. Nanoparticles with thin carbon layer: (a) TEM images of core-shell type nanoparticles and electron diffraction pattern (inset) indicating crystalline particles, (b) high-resolution TEM image of the single crystal particle (marked by an arrow) with lattice fringes corresponding to anatase (101), (c) STEM BSE image (topographical mode) of core-shell nanoparticles. Nanoparticles with thick carbon layer: (d) TEM image of nanoparticles covered with a thick carbon layer, marked by an arrow, (e) STEM BSE image (topographical mode) of nanoparticles with a thick carbon layer, and (f) STEM-EDS line analysis of nanoparticles showing intensity variation of Ti, O and C.

nanoparticles synthesized at 10 MPa, 50 °C, while the second section deals with the effect of CO₂ pressure and temperature on the nanoparticle size, size distribution and phase.

Section 1: Morphology, composition, phase analysis and band-gap measurement of nanoparticles synthesized at 10 MPa, 50 °C

Morphology and composition of nanoparticles. The (S)TEM images (figures 3(a)–(f)) showed presence of round nanoparticles that formed clusters or networks. Such nano-networks formed by ablation in scCO₂ have been previously reported [19]. Electron diffraction patterns indicated crystallinity of these nanoparticles (figure 3(a) inset). Based on the lattice fringes, some particles were single crystals while others were polycrystalline. On the basis of (S)TEM images, the nanoparticles can be classified into two types: (i) core-shell nanoparticles (figures 3(a)–(c)), and (ii) nanoparticles surrounded by thick layer (figures 3(d) and (e)). In case of core-shell nanoparticles, the shell surface was smooth and the thickness of the shell varied from particle to particle. Jung *et al* [28] also reported varying shell thickness and observed increase in the carbon shell thickness with the increase in the core-shell nanoparticles size. For clusters with thicker carbon layer, the nanoparticles did not appear to be typical core-shell structures as the layer surrounded several nanoparticles (figure 3(d)). This is further elucidated from the

backscattered electron image (topographical mode) in figure 3(e) where particles seemed to be buried under thick layer. In such cases, the particles seemed to form clusters first after which carbon layer may grow on top of them. The nanoparticles, in figure 3(d), with a thick surface layer were rarer than the core-shell structures on the TEM grid, making the core-shell nanoparticles to be the dominant species. This has been previously reported in PLA of iron-gold where over 90% of nanoparticles consisted of a core-shell morphology [29]. In our study, samples from each test condition consisted of two populations of nanoparticles covered with either thin or thick carbon layer. We did not observe a significant change in the shell thickness in either population nor any change in the relative amount of the two populations as the process parameters were varied. STEM-EDS line analysis (figure 3(f)) and spot analysis indicated that nanoparticle core consisted of mostly titanium and oxygen, while the shell/surface layer consisted of carbon. A drop in the titanium, oxygen peak intensities and a surge in the carbon peak intensity was observed between 80 and 100 nm (figure 3(f)). A dramatic change in carbon peak intensity at the centre of particles is not observed as it is a cluster of nanoparticles. They can be considered as 3D spheres with surface shell and the electron beam interacts with them orthogonally. This implies that there will always be some carbon intensity in the STEM-EDS spectra, higher than for titanium and oxygen. In addition, the

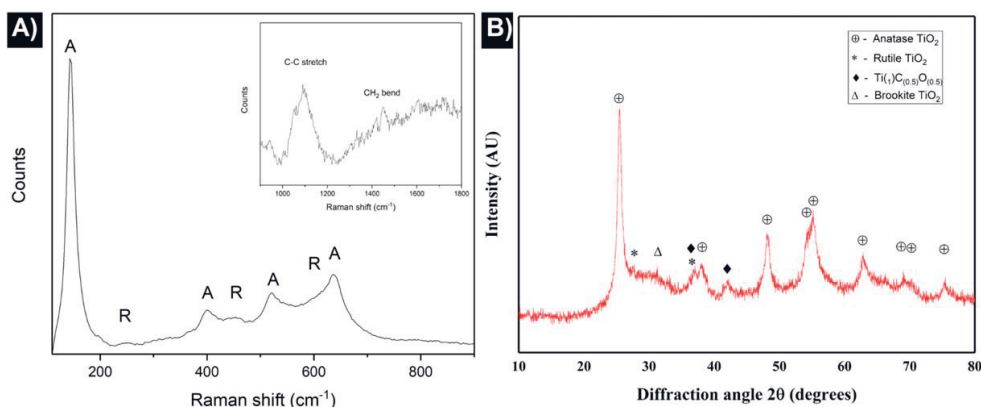


Figure 4. (a) Raman spectra and (b) XRD spectra of the nanoparticles synthesized at 10 MPa, 50 °C.

TEM grid also has a holey carbon film, as mentioned earlier in the experimental section.

Raman and XRD analysis of nanoparticles. Raman measurements of the synthesized nanoparticles indicated presence of mostly anatase-TiO₂ with small amounts of rutile-TiO₂ (figure 4(a)). The strongest peaks in Raman spectra at around 144, 400, 520, and 636 cm⁻¹ corresponded to anatase-TiO₂. The peaks corresponding to rutile at around 447 and 610 cm⁻¹ can be observed as small features and shoulders in the anatase spectrum. XRD supports Raman results indicating presence of mostly anatase-TiO₂. Sharp distinct peaks of anatase were observed at 25.3, 48.1, 54.1 and 55.2 2θ degrees (figure 4(b)). The other remaining peaks of anatase observed are marked in the figure. Other peaks in the XRD spectrum could be explained by rutile-TiO₂ at 27.4, titanium oxide carbide Ti_{(1)O_{(0.5)C_(0.5)} at 42.1 and 36.2 2θ degrees, and brookite-TiO₂ at 30.8 2θ degrees. No graphitic-carbon peaks at 26.1 and 42.3 2θ degrees could be distinctly observed; however, amorphous nature of carbon may have caused the broad pedestal starting from under the anatase peak at 25.3 until the peak for brookite at 30.8. As reported by Marzum *et al* in a study of core-shell nanoparticles synthesized by PLA in liquids, it is difficult to observe amorphous carbon on nanoparticles by XRD technique as it is more suitable for crystalline materials [30]. Thus, Raman and XRD spectra suggest anatase-TiO₂ as the main phase of nanoparticles with small amount of rutile-TiO₂, and in addition XRD suggests presence of brookite-TiO₂ and carbon containing phase Ti_{(1)O_{(0.5)C_(0.5)}. Further, the peaks for TiC were missing from both Raman and XRD spectra, suggesting carbon may not be chemically bonded to titanium. Additionally, for wide spectrum measurement (figure 4(a) inset), Raman spectra showed a broad feature centred at about 1100 cm⁻¹ and near 1450 cm⁻¹. As the D and G bands are not observed, this suggests that the carbon on top of the samples is possibly due to hydrocarbons rather than pure carbon. The peak at 1100 cm⁻¹ can be attributed to C-C bond}}

stretching whereas the feature at 1450 cm⁻¹ can be attributed to CH₂ twists and bends.

XPS analysis of nanoparticles. In the XPS spectra of the sample (figure 5(a)), peaks for Ti2p, O1s and C1s were observed. In figure 5(b), C1s peak between 284 and 286 eV indicated presence of carbon in sp² hybridization, C=C. The broadening of this peak around 286–287 may indicate presence of also sp³ carbon. Peak between 288 and 290 eV was likely from O=C=O. Carbon-titanium bonds would cause peaks at 281.5, 454.7, and 460.9 eV, which were not observed. The peak in XPS spectra figure 5(c) corresponds to the O1s peak at 530 nm. The shoulder to this peak at 532 nm likely comes from organic C=O (531.5–532 nm) indicating possible presence of organic carbonyl, ketones or it may likely be from the H–O–C bond. Metal carbonate, such as TiCO₃ (531.5–532 nm) may possibly add to this feature at 532 nm. Ti 2p1 and Ti 2p3 peaks at 464.3 and 458.5 eV respectively observed in the XPS spectra (figure 5(d)) indicated presence of titanium in +4 oxidation state Ti(IV) and the band energies corresponded to anatase-TiO₂ and rutile-TiO₂. XPS results were in accordance with Raman and XRD results to indicate presence of anatase and rutile and further suggested presence of carbon on the nanoparticles, which was not observed to be bonded to titanium.

Band-gap measurement. The band gap of the nanoparticles was calculated to be 3.32 eV from the reflectance spectra using the Tauc plot (figure 6). The bulk value for anatase is reported as 3.2 eV [31], but thin films and nanoparticles are reported to have higher band gaps due to surface states and quantum size effect [32, 33]. Thus, the measured band gap agrees with Raman and XRD results suggesting the particles are mostly anatase TiO₂.

Discussion on synthesis of nanoparticle by PLA in pressurized CO₂, their composition and phase analysis. During PLA, the laser irradiates the target, ionized target species are ejected and trapped inside laser induced high temperature plasma

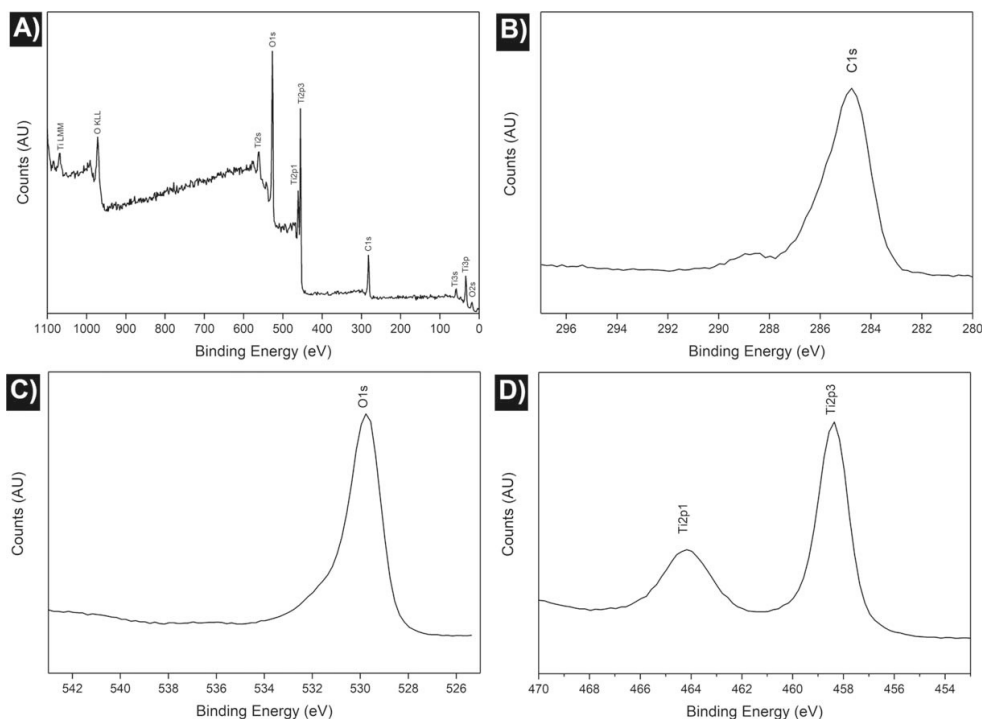


Figure 5. (a) XPS spectra of nanoparticles synthesized at 10 MPa, 50 °C, (b) carbon C1s peak, (c) O1s peak, (d) Ti2p doublet peaks in high resolution XPS spectra.

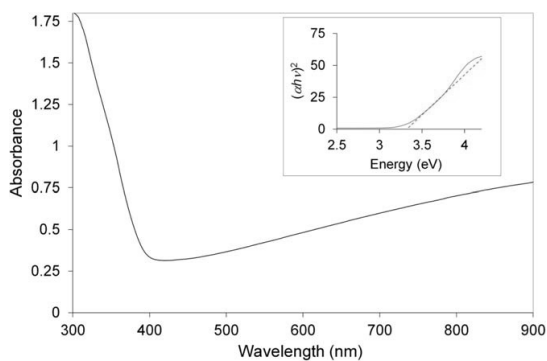


Figure 6. Absorbance spectra from 300 to 900 nm and band-gap (in inset) of the nanoparticles synthesized at 10 MPa, 50 °C.

plume which occurs over a timescale of hundreds of nanoseconds followed by formation of clusters and their growth inside the plasma [34–36]. Kato *et al* reported formation of plasma and breakdown of CO_2 in PLA in scCO_2 over a short timescale of few hundred nanoseconds after the laser pulse hit the target and observed generation of cavitation bubble at $5 \mu\text{s}$ and its collapse at around $100 \mu\text{s}$ [37]. The plasma temperature depending on the CO_2 pressure has been reported to be $3873 \text{ }^\circ\text{C}$ – $4873 \text{ }^\circ\text{C}$ by Maehara *et al* [38] and $8273 \text{ }^\circ\text{C}$ – $12273 \text{ }^\circ\text{C}$ by Furusato *et al* [39]. The high temperature of plasma decomposes CO_2 into atomic oxygen

[37, 39], carbon ions and radicals [37] and carbon monoxide positive ions CO^+ [39]. Kato *et al* reported presence of atomic oxygen and atomic carbon in addition to atomic target metal species in the optical emission spectra of PLA plasmas in scCO_2 [37]. The presence of plasma plume formation is followed by formation of a cavitation bubble wherein species originating from the target and the solvent combine to form the clusters and nanoparticles, which are released to the ambient solvent upon the collapse of the cavitation bubble. Lam *et al* reported that the cavitation bubble consists mostly of solvent species rather than the ablated material for PLA in liquids at normal pressure [40]. The cavitation bubble in scCO_2 has been reported to expand like in liquid but collapse like in gas with the bubble boundary being ragged having higher surface area compared to PLA in liquid CO_2 [37]. Then the reaction for nanoparticle formation inside the cavitation bubble begins between the ablated target species i.e. Ti ions and solvent species from previously plasma decomposed CO_2 molecules to form titanium oxides. Upon the collapse of the cavitation bubble, the hot nanoparticles are released into the surrounding pressurized CO_2 . DFT simulations show that oxygen vacancies in Anatase TiO_2 can act as efficient catalyst to dissociate CO_2 and the oxygen from CO_2 heals the vacancy [41]. Simulations show that this occurs at relatively low temperatures (400 K). This mechanism likely plays a role in the formation and further oxidation of titanium oxide nanoparticles. The produced CO has tendency to stay

adsorbed and may further dissociate to carbon according to Boudouard reaction ($2\text{CO}=\text{C} + \text{CO}_2$) and initiate the formation of the carbon shell.

In cases where the nanoparticles are individual particles, the carbon forms as a shell on top of the particles (such as in figures 3(a) and (b)), whereas for the coalesced clusters of nanoparticles the carbon coating is formed over the whole cluster rather (such as in figures 3(d) and (e)) than on the individual particles. Salminen *et al* suggested laser-induced heating of the nanoparticles to be crucial for shell formation [42]. Marzum *et al* attributed formation of graphitic carbon shell to be catalysed by copper in their study on synthesis of copper-carbon core-shell nanoparticles [30].

While rutile-TiO₂ is a more thermodynamically stable phase than anatase-TiO₂ [43], and is a dominant phase in PLA in water [44], in this study, as a result of PLA in pressurized CO₂ (in gaseous, liquid and supercritical states), anatase-TiO₂ was the predominant phase as observed in the Raman and XRD spectra (figures 9 and 13). Metastable anatase-TiO₂ once formed does not transform to rutile because of strong binding energy of Ti-O ionic covalent bond, unless melting-like processes are involved [45].

Titanium dioxide phases are observed in Raman, XPS and XRD, however, presence of other meta-stable phases, such as Ti₃O₅ and Ti_{(1)O_(0.5)C_(0.5), was also indicated by the XRD spectra. CO₂ above 760 °C may undergo Boudouard reaction with carbon to form CO which may reduce TiO₂ to form titanium oxides with lower degree of oxygen such as Ti₃O₅ and further substitution of oxygen with carbon to form Ti_xC_yO_z [46]. Another possibility is that if the temperatures is above 2273 °C, in an environment of excess carbon, TiO₂ and its other oxides are not stable and reduce to Ti(C_xO_y) or TiC, however, a direct conversion from TiO₂ to Ti(C_xO_y) is not possible without the synthesis of Ti₃O₅ and Ti₂O₃ in between the pathway of this transformation [47]. Observation of Ti₃O₅ and Ti_{(1)O_(0.5)C_(0.5) in the XRD spectra (figure 9) could either be an indication of oxidation of titanium in insufficient oxygen environment or carbothermal reduction of TiO₂ [47]. The absence of high amounts of rutile-TiO₂ and no observation of TiC may indicate that such high temperatures may not be reached by the synthesized particles to cause phase transformations, however, to some extent transformation may be possible when the nanoparticle size is small enough. Additionally, rutile may form directly without the need of transformation from anatase. The absence of TiC phase could be explained based on thermodynamic calculations. TiO₂ formation from titanium is thermodynamically more favourable than TiC, based on Ellingham diagram. Solving Gibbs free energy equations for TiO₂ and TiC, calculations show TiO₂ formation stays highly favourable until 4529 K.}}

With PLA in pressurized CO₂, we synthesized nanoparticles of metastable anatase-TiO₂ core with carbon layer. However, it is not yet fully understood whether carbon shells on nanoparticles already appear inside the cavitation bubble and whether the particles undergo several coatings of carbon if the ablation durations are long. *In situ* studies with small-angle x-ray scattering (SAXS), wide-angle x-ray scattering

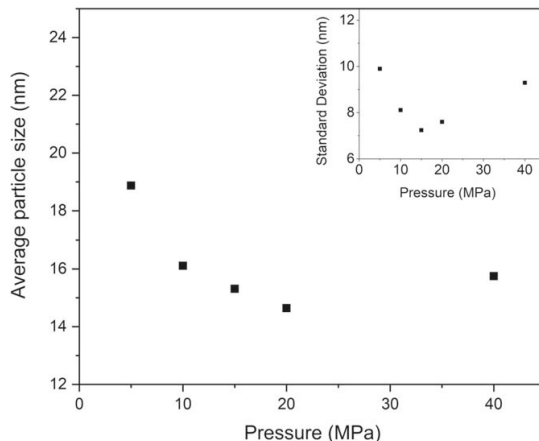


Figure 7. Variation in nanoparticle size with increase in CO₂ pressure. The inset shows the variation in standard deviation with CO₂ pressure.

(WAXS), infrared (IR) and Raman spectroscopy will make good future scope of work to provide insight on this topic.

Section 2: Effect of CO₂ pressure and temperature on particle size and phase

Effect of CO₂ pressure on nanoparticles. The average particle size when plotted for nanoparticles synthesized at 5–40 MPa CO₂ pressures at 50 °C temperature showed a decreasing trend from 19 nm to 14.5–15 nm with increasing pressures (figure 7). This is in agreement with the reduction in size of Sn [48], ZnO [49], and Au [26] nanoparticles with an increase in ambient fluid pressure (CO₂, H₂O) as reported in literature by PLA in pressurized fluids. This was attributed to smaller volume and shorter lifetimes of the cavitation bubbles at higher solvent (CO₂, H₂O) pressures [49, 50].

The size distribution of the synthesized nanoparticles (figure 8) slightly decreased with the increase in pressure. This is observable from the lognormal fitted curves for each size distribution and decreasing trend in the variation of the standard deviation (figure 7 inset). This is in agreement with the narrowing of size distribution with increasing pressures reported for ablation of gold in pressurized CO₂ [26].

Regarding effect of CO₂ pressure variation on nanoparticle phase, the Raman spectra (figure 9(a)) indicated that anatase-TiO₂ is the main phase of the nanoparticles for all samples. Based on the area of the fitted peaks, the rutile content seems to increase with the CO₂ pressure (figure 10(a)). Similarly, the XRD measurements (figure 9(b)) show that the samples are mostly anatase. The area of the fitted peaks in XRD (figure 10(b)) corroborated Raman results and showed an increasing trend. The peak at 21.2 2θ degrees corresponding to the high-temperature metastable phase Ti₃O₅ was observed only for 15 MPa CO₂ pressure. XRD and Raman indicated synthesis of mostly anatase-TiO₂ nanoparticles within the range of pressures tested as well as a slight increase in rutile-TiO₂ content as pressure increased.

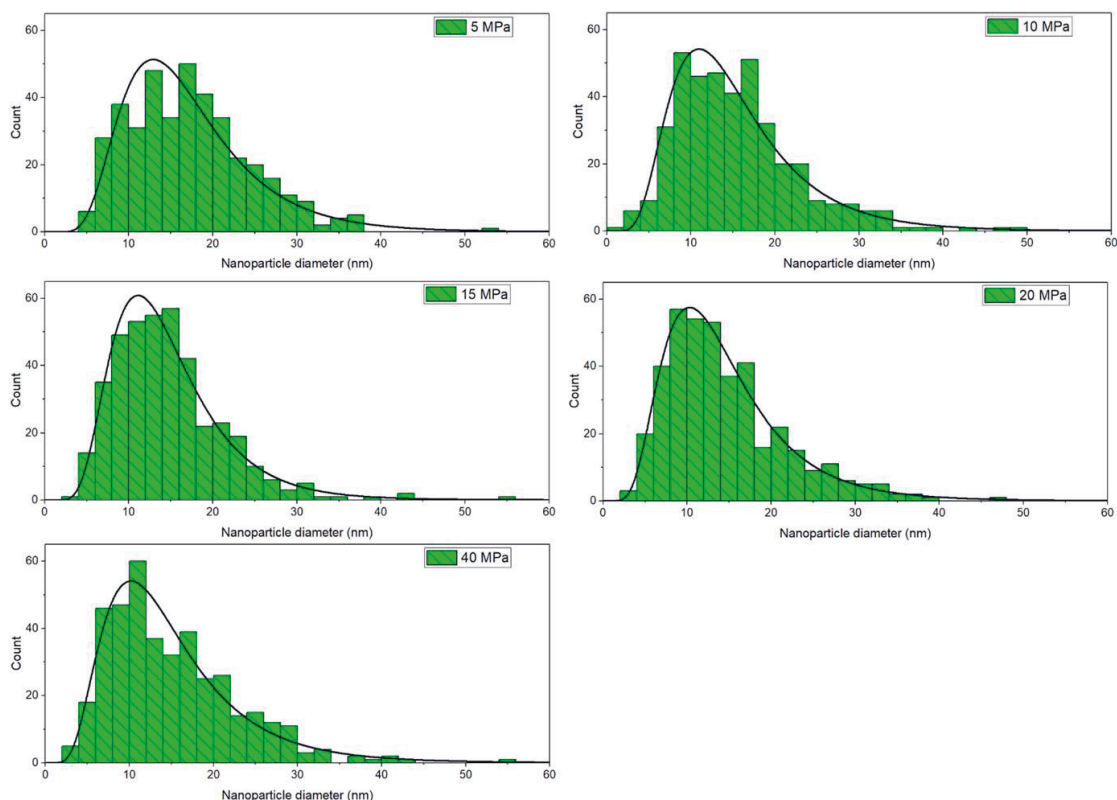


Figure 8. Size distribution of nanoparticles produced from 5 to 40 MPa at 50 °C.

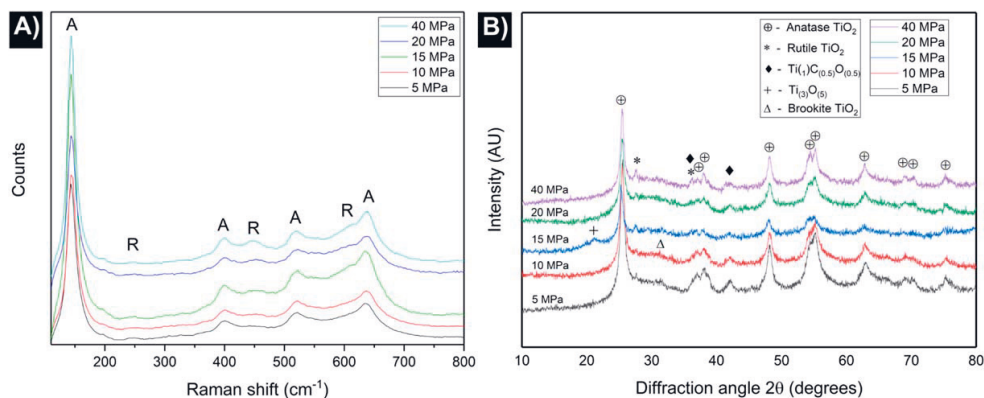


Figure 9. (a) Raman and (b) XRD spectra for nanoparticles synthesized at 50 °C and pressures 5, 10, 15, 20, and 40 MPa.

Effect of CO₂ temperature on nanoparticles. The influence of CO₂ pressure on cavitation bubble dynamics has been reported in literature [50, 51], however, the effect of CO₂ temperature has not been studied as much. A clear trend of decreasing nanoparticle size and narrower size distribution was observed with the increase in CO₂ temperature from 30 °C to 50 °C (figures 11 and 12). Although the experimental parameters at 30 °C correspond to liquid CO₂, it is highly

likely that the heating due to the laser pulse leads to local conditions corresponding to supercritical CO₂. The trend in the nanoparticle size is somewhat surprising considering that increasing the temperature while keeping the pressure constant leads to a drop in CO₂ density (figure 2), whereas when keeping the temperature constant, the simultaneously increasing pressure and density leads to production of smaller nanoparticles. Cavitation bubble dynamics and its influence

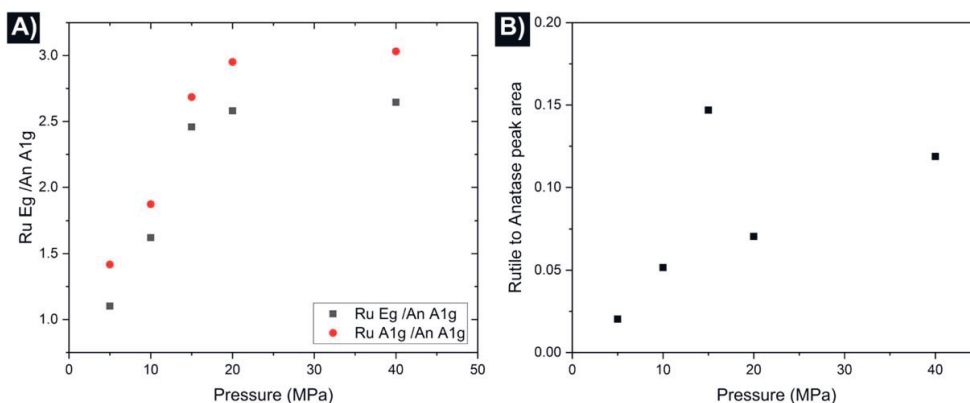


Figure 10. Area of fitted peaks rutile-to-anatase for all pressures from (a) Raman spectra, (b) XRD spectra.

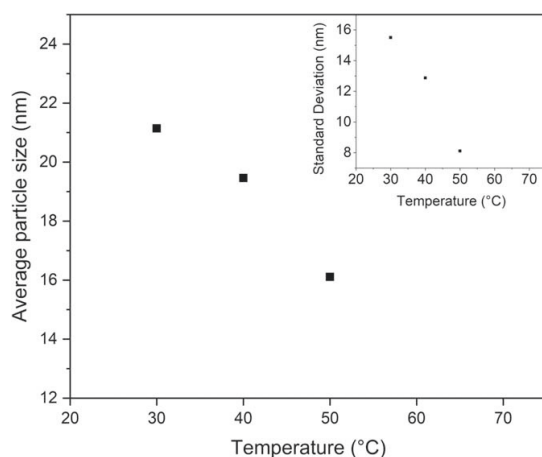


Figure 11. Effect of CO₂ temperature on nanoparticle size; in the inset is reported the variation of standard deviation with CO₂ temperature.

on the formed particles has been thoroughly studied in liquids using SAXS [52, 53]. To really understand the complex dynamics, a similar comprehensive study for supercritical fluids would be very interesting. Increasing CO₂ temperature showed a slight narrowing of the nanoparticle size distribution (figure 12) corresponding to the decreasing standard deviation (figure 11 inset). In this case, the widest size distribution was observed for CO₂ in liquid state i.e. at 30 °C.

XRD and Raman indicated the main phase of nanoparticles was anatase-TiO₂ and remained unchanged despite the change in CO₂ temperature from 30 °C to 50 °C (figures 13(a) and (b)). Unlike in CO₂ pressure variation, in case of CO₂ temperature variation, a conclusive trend on variation in rutile amount could not be observed.

Amongst the tested process conditions, the lowest temperature and the lowest pressure test conditions i.e. 30 °C, 10 MPa (gaseous CO₂) and 50 °C, 5 MPa (liquid CO₂) respectively, are interesting as they are both not supercritical

conditions for CO₂. When compared these two extreme test conditions to all other test conditions, the nanoparticle sizes were the highest and size distributions among the widest in non-supercritical conditions. This may imply that PLA in CO₂ in supercritical conditions produced nanoparticles with smaller size and slightly narrower size distribution than in liquid (at same temperature) or gaseous state (at same pressure). In addition, regarding the minor phase, the rutile content was among the least for the tests in non-supercritical conditions.

Conclusions

To the best of our knowledge, this is the first study that demonstrates PLA in liquid, gaseous and supercritical CO₂ for production of TiO₂-carbon core-shell nanoparticles. STEM-EDS showed the nanoparticles were mostly round with either carbon layers on them individually like a shell or coalesced nanoparticles collectively covered with carbon layers. STEM backscatter topography mode elucidated this observation. XPS, Raman and XRD indicated anatase-TiO₂ as the main phase of nanoparticles with minor amounts of rutile-TiO₂, and possibility of presence of brookite-TiO₂, Ti_{(1)O_(0.5)C_(0.5), and Ti₃O₅. Although, Ti_{(1)O_(0.5)C_(0.5) phase was detected in XRD, XPS indicated that carbon was not bonded to titanium. This was further corroborated by XRD and Raman results. The bandgap energy of these nanoparticles was calculated to be 3.32 eV.}}

Increase in CO₂ pressure from 5 to 40 MPa at 50 °C led to decrease in the nanoparticle size and narrowing of the size distribution. The mechanism of size refinement was attributed to shorter cavitation bubble lifetime and smaller volume at higher pressures. From Raman and XRD spectra, we observed that anatase-TiO₂ was the main phase of nanoparticles in all CO₂ pressures 5–40 MPa tested at 50 °C. The ratio of area of the fitted rutile-anatase peaks indicated increase in rutile content with increase in pressure in both Raman and XRD. Further, when the CO₂ temperature was varied from 30 °C to 50 °C at 10 MPa pressure, we observed decreasing trend in particle size and narrowing of size

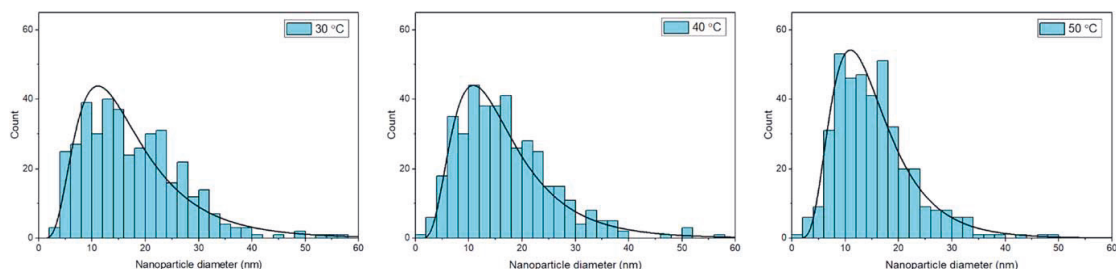


Figure 12. Size distribution of nanoparticles synthesized at 10 MPa and temperatures 30 °C, 40 °C, and 50 °C.

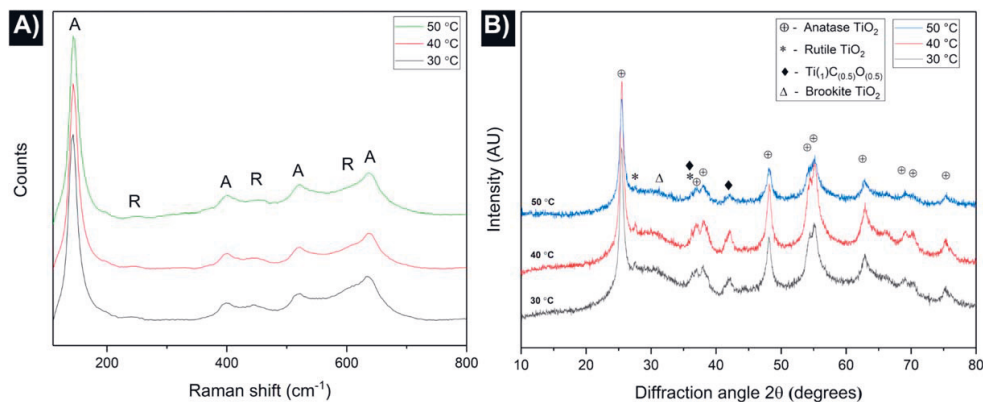


Figure 13. (a) Raman and (b) XRD spectra for nanoparticles synthesized at 10 MPa and temperatures 30 °C, 40 °C, and 50 °C.

distribution. In this case, we observed anatase-TiO₂ as the main phase of nanoparticles at all temperatures, however, the variation in the amount of rutile-TiO₂ could not be conclusively determined based on peaks in Raman and XRD spectra.

For future work, *in situ* studies with SAXS, WAXS, IR and Raman microscopy would be crucial to give insight on the process dynamics, nanoparticle nucleation, and breakdown of CO₂ with variation in CO₂ parameters. For this, the autoclave will have to be modified to accommodate the measurement systems.

Acknowledgments

This work was supported by European Commission's Horizon 2020 project 'NanoStencil'—Proposal number 767285. This work made use of Tampere Microscopy Centre facilities at Tampere University. We would like to acknowledge Jere Manni for XPS studies performed at Top Analytica.

Declaration

The authors declare no conflict of interest.

ORCID iDs

Amandeep Singh  <https://orcid.org/0000-0002-4087-6096>

References

- [1] Friedmann D, Mendive C and Bahnemann D 2010 TiO₂ for water treatment: parameters affecting the kinetics and mechanisms of photocatalysis *Appl. Catal. B* **99** 398–406
- [2] Exnar I, Kavan L, Huang S Y and Grätzel M 1997 Novel 2 V rocking-chair lithium battery based on nano-crystalline titanium dioxide *J. Power Sources* **68** 720–2
- [3] Tennakone K, Kumarasinghe A R, Sirimanne P M and Kumara G R R A 1995 Deposition of thin polycrystalline films of cuprous thiocyanate on conducting glass and photoelectrochemical dye-sensitization *Thin Solid Films* **261** 307–10
- [4] Park J, Back T, Mitchel W C, Kim S S, Elhamri S, Boeckl J, Fairchild S B, Naik R and Voevodin A A 2015 Approach to multifunctional device platform with epitaxial graphene on transition metal oxide *Sci. Rep.* **5** 14374
- [5] Lee J-M, Han S-B, Kim J-Y, Lee Y-W, Ko A-R, Roh B, Hwang I and Park K-W 2010 TiO₂@carbon core-shell nanostructure supports for platinum and their use for methanol electrooxidation *Carbon* **48** 2290–6
- [6] Gawande M B, Goswami A, Asefa T, Guo H, Biradar A V, Peng D, Zboril R and Varma R S 2015 Core-shell nanoparticles: synthesis and applications in catalysis and electrocatalysis *Chem. Soc. Rev.* **44** 7540–90

- [7] Feng H, Tang L, Zeng G, Zhou Y, Deng Y, Ren X, Song B, Liang C, Wei M and Yu J 2019 core-shell nanomaterials: applications in energy storage and conversion *Adv. Colloid Interface Sci.* **267** 26–46
- [8] Kumar K S, Kumar V B and Paik P 2013 Recent advancement in functional core-shell nanoparticles of polymers: synthesis, physical properties, and applications in medical biotechnology *J. Nanopart.* **2013** 1–24
- [9] Chang W, Skandan G, Hahn H, Danforth S C and Kear B H 1994 Chemical vapor condensation of nanostructured ceramic powders *Nanostruct. Mater.* **4** 345–51
- [10] Kobayashi Y, Correa-Duarte M A and Liz-Marzán L M 2001 Sol-gel processing of silica-coated gold nanoparticles *Langmuir* **17** 6375–9
- [11] Wang Y, Teng X, Wang J-S and Yang H 2003 Solvent-free atom transfer radical polymerization in the synthesis of Fe₂O₃@polystyrene core-shell nanoparticles *Nano Lett.* **3** 789–93
- [12] Biswas P, Wu C Y, Zachariah M R and McMillin B 1997 Characterization of iron oxide-silica nanocomposites in flames: II. Comparison of discrete-sectional model predictions to experimental data *J. Mater. Res.* **12** 714–23
- [13] Chen K Z, Zhang Z K, Cui Z L, Zuo D H and Yang D Z 1997 Catalytic properties of nanostructured hydrogen storage nickel particles with cerium shell structure *Nanostruct. Mater.* **8** 205–13
- [14] Vollath D and Szabo D V 1999 Coated nanoparticles: a new way to improved nanocomposites *J. Nanopart. Res.* **1** 235–42
- [15] Yu F, Wang J N, Sheng Z M and Su L F 2005 Synthesis of carbon-encapsulated magnetic nanoparticles by spray pyrolysis of iron carbonyl and ethanol *Carbon* **43** 3018–21
- [16] Kazakevich P V, Simakin A V, Voronov V V, Shafeyev G A, Starikov D and Bensaoula A 2005 Formation of core-shell nanoparticles by laser ablation of copper and brass in liquids *Solid State Phenom.* **106** 23–6
- [17] Zhang D, Gökçe B and Barcikowski S 2017 Laser synthesis and processing of colloids: fundamentals and applications *Chem. Rev.* **117** 3990–4103
- [18] Singh A, Salminen T, Honkanen M, Vihinen J, Hyvärinen L and Levänen E 2019 Multiphase Ti_xO_y nanoparticles by pulsed laser ablation of titanium in supercritical CO₂ *Appl. Surf. Sci.* **476** 822–7
- [19] Saitow K, Yamamura T and Minami T 2008 Gold nanospheres and nanonecklaces generated by laser ablation in supercritical fluid *J. Phys. Chem. C* **112** 18340–9
- [20] Saitow K 2005 Silicon nanoclusters selectively generated by laser ablation in supercritical fluid *J. Phys. Chem. B* **109** 3731–3
- [21] Machmudah S, Sato T, Wahyudiono, Sasaki M and Goto M 2012 Silver nanoparticles generated by pulsed laser ablation in supercritical CO₂ medium *High Press. Res.* **32** 60–6
- [22] Kuwahara Y, Saito T, Haba M, Iwanaga T, Sasaki M and Goto M 2009 Nanosecond pulsed laser ablation of copper in supercritical carbon dioxide *Japan. J. Appl. Phys.* **48** 040207
- [23] Nakahara S, Stauss S, Kato T, Sasaki T and Terashima K 2011 Synthesis of higher diamondoids by pulsed laser ablation plasmas in supercritical CO₂ *J. Appl. Phys.* **109** 123304
- [24] Machmudah S, Kuwahara Y, Sasaki M and Goto M 2011 Nano-structured particles production using pulsed laser ablation of gold plate in supercritical CO₂ *J. Supercrit. Fluids* **60** 63–8
- [25] Mardis M, Takada N, Machmudah S, Wahyudiono, Sasaki K, Kanda H and Goto M 2016 Nickel nanoparticles generated by pulsed laser ablation in liquid CO₂ *Res. Chem. Intermed.* **42** 4581–90
- [26] Mardis M, Wahyudiono, Takada N, Kanda H and Goto M 2018 Formation of Au-carbon nanoparticles by laser ablation under pressurized CO₂ *Asia-Pacific J. Chem. Eng.* **13** e2176
- [27] National Institute of Standards and Technology 2018 US Department of Commerce Thermophysical Properties for Carbon dioxide *NIST Chemistry WebBook* (SRD 69) (Gaithersburg, MD: National Institute of Standards and Technology) (<https://doi.org/10.18434/T4D303>)
- [28] Jung H J and Choi M Y 2018 One-pot synthesis of graphitic and nitrogen-doped graphitic layers on nickel nanoparticles produced by pulsed laser ablation in liquid: Solvent as the carbon and nitrogen source *Appl. Surf. Sci.* **457** 1050–6
- [29] Wagener P, Jakobi J, Rehbock C, Chakravadhanula V S K, Thede C, Wiedwald U, Bartsch M, Kienle L and Barcikowski S 2016 Solvent-surface interactions control the phase structure in laser-generated iron-gold core-shell nanoparticles *Sci. Rep.* **6** 1–12
- [30] Marzun G, Bönemann H, Lehmann C, Spliethoff B, Weidenthaler C and Barcikowski S 2017 Role of dissolved and molecular oxygen on Cu and PtCu alloy particle structure during laser ablation synthesis in liquids *ChemPhysChem* **18** 1175–84
- [31] Reyes-Coronado D, Rodríguez-Gattorno G, Espinosa-Pesqueira M E, Cab C, de Coss R and Oskam G 2008 Phase-pure TiO₂ nanoparticles: anatase, brookite and rutile *Nanotechnology* **19** 145605
- [32] Wang Y and Herron N 1991 Nanometer-sized semiconductor clusters: materials synthesis, quantum size effects, and photophysical properties *J. Phys. Chem.* **95** 525–32
- [33] Madhusudan Reddy K, Manorama S V and Ramachandra Reddy A 2003 Bandgap studies on anatase titanium dioxide nanoparticles *Mater. Chem. Phys.* **78** 239–45
- [34] Amendola V and Meneghetti M 2013 What controls the composition and the structure of nanomaterials generated by laser ablation in liquid solution? *Phys. Chem. Chem. Phys.* **15** 3027–46
- [35] Shih C-Y, Wu C, Shugaev M V and Zhigilei L V 2017 Atomistic modeling of nanoparticle generation in short pulse laser ablation of thin metal films in water *J. Colloid Interface Sci.* **489** 3–17
- [36] Amendola V and Meneghetti M 2009 Laser ablation synthesis in solution and size manipulation of noble metal nanoparticles *Phys. Chem. Chem. Phys.* **11** 3805–21
- [37] Kato T, Stauss S, Kato S, Urabe K, Baba M, Suemoto T and Terashima K 2012 Pulsed laser ablation plasmas generated in CO₂ under high-pressure conditions up to supercritical fluid *Appl. Phys. Lett.* **101** 224103
- [38] Maehara T, Kawashima A, Iwamae A, Mukasa S, Takemori T, Watanabe T, Kurokawa K, Toyota H and Nomura S 2009 Spectroscopic measurements of high frequency plasma in supercritical carbon dioxide *Phys. Plasmas* **16** 033503
- [39] Furusato T, Ashizuka N, Kamagahara T, Matsuda Y, Yamashita T, Sasaki M, Kiyan T and Inada Y 2018 Anomalous plasma temperature at supercritical phase of pressurized CO₂ after pulsed breakdown followed by large short-circuit current *IEEE Trans. Dielectr. Electr. Insul.* **25** 1807–13
- [40] Lam J, Lombard J, Dujardin C, Ledoux G, Merabia S and Amans D 2016 Dynamical study of bubble expansion following laser ablation in liquids *Appl. Phys. Lett.* **108** 074104
- [41] Huygh S, Bogaerts A and Neyts E C 2016 How oxygen vacancies activate CO₂ dissociation on TiO₂ anatase (001) *J. Phys. Chem. C* **120** 21659–69
- [42] Salminen T, Honkanen M and Niemi T 2013 Coating of gold nanoparticles made by pulsed laser ablation in liquids with silica shells by simultaneous chemical synthesis *Phys. Chem. Chem. Phys.* **15** 3047–51

- [43] Cui Z-H, Wu F and Jiang H 2016 First-principles study of relative stability of rutile and anatase TiO₂ using the random phase approximation *Phys. Chem. Chem. Phys.* **18** 29914–22
- [44] Singh A, Vihinen J, Frankberg E, Hyvärinen L, Honkanen M and Levänen E 2016 Pulsed laser ablation-induced green synthesis of tio₂ nanoparticles and application of novel small angle x-ray scattering technique for nanoparticle size and size distribution analysis *Nanoscale Res. Lett.* **11** 447
- [45] Satoh N, Nakashima T and Yamamoto K 2013 Metastability of anatase: size dependent and irreversible anatase-rutile phase transition in atomic-level precise titania *Sci. Rep.* **3** 1959
- [46] Hajalilou A, Hashim M, Ebrahimi-Kahizsangi R, Ismail I and Sarami N 2014 Synthesis of titanium carbide and TiC–SiO₂ nanocomposite powder using rutile and Si by mechanically activated sintering *Adv. Powder Technol.* **25** 1094–102
- [47] Kim J and Kang S 2014 Stable phase domains of the TiO₂–Ti₃O₅–Ti₂O₃–TiO–Ti(C_xO_y)–TiC system examined experimentally and via first principles calculations *J. Mater. Chem. A* **2** 2641–7
- [48] Koizumi M, Kulinich S A, Shimizu Y and Ito T 2013 Slow dynamics of ablated zone observed around the density fluctuation ridge of fluid medium *J. Appl. Phys.* **114** 214301
- [49] Kulinich S A, Kondo T, Shimizu Y and Ito T 2013 Pressure effect on ZnO nanoparticles prepared via laser ablation in water *J. Appl. Phys.* **113** 033509
- [50] Sasaki K, Nakano T, Soliman W and Takada N 2009 Effect of pressurization on the dynamics of a cavitation bubble induced by liquid-phase laser ablation *Appl. Phys. Express* **2** 046501
- [51] Takada N and Machmudah S 2014 Characteristics of optical emission intensities and bubblelike phenomena induced by laser ablation in supercritical fluids *Japan. J. Appl. Phys.* **53** 010213
- [52] Wagener P, Ibrahimkutty S, Menzel A, Plech A and Barcikowski S 2013 Dynamics of silver nanoparticle formation and agglomeration inside the cavitation bubble after pulsed laser ablation in liquid *Phys. Chem. Chem. Phys.* **15** 3068–74
- [53] Ibrahimkutty S, Wagener P, Rolo T D S, Karpov D, Menzel A, Baumbach T, Barcikowski S and Plech A 2015 A hierarchical view on material formation during pulsed-laser synthesis of nanoparticles in liquid *Sci. Rep.* **5** 16313

